A High Power Interior Permanent Magnet Alternator for Automotive Applications

Chong-Zhi Liaw

March 15, 2013

Contents

List of Figures

List of Tables

Abstract

This thesis examines the operation of a 6 kW interior permanent magnet machine as a generator and its use in conjunction with a switched-mode rectifier as a controllable current source. The interior permanent magnet machine was designed for optimum field-weakening performance which allows it to achieve a wide constant-power speed range. This configuration has possible applications in power generation, e.g. as an alternator in automotive electrical systems and in renewable energy systems such as small-scale wind turbines.

The thesis starts from a study of the behaviour of the interior PM machine while generating into a three-phase resistive load and also through a rectifier into a voltage source load. Steady-state and dynamic d-q models are developed which describe the machine generation characteristics. The concept of the VI locus is introduced which provides insights into the generating performance of interior PM machines. In particular, the phenomenon of hysteresis in the current versus speed characteristic of highly salient interior PM machines is explained using the VI locus and for the first time is experimentally demonstrated.

The steady-state and transient response of the 6 kW interior PM machine while operating with a switched-mode rectifier is modeled and experimentally measured, forming the basis for the design of a closed-loop controller to regulate the output voltage. The experimental performance and stability of the closed-loop system is examined and evaluated. Further improvements to the output power of the system at low speed using a switched-mode rectifier modulation scheme are investigated and a 66% improvement in output power from 2.8 kW to 4.7 kW is experimentally demonstrated.

Statement of Originality

I, Chong-Zhi Liaw certify that this work contains no material which has been accepted for the award of any other degree or diploma in any university or other tertiary institution and, to the best of my knowledge and belief, contains no material previously published or written by another person, except where due reference has been made in the text.

I give consent to this copy of my thesis when deposited in the University Library, being made available for loan and photocopying, subject to the provisions of the Copyright Act 1968.

I also give permission for the digital version of my thesis to be made available on the web, via the University's digital research repository, the Library catalogue and also through web search engines, unless permission has been granted by the University to restrict access for a period of time.

Signed: _____

Date: _____

Acknowledgements

I would like to offer my deepest gratitude to my supervisor, Associate Prof. Wen L. Soong for his invaluable guidance, patience and support throughout the course of my research, as well as to my co-supervisor Associate Prof. Nesimi Ertugrul for his valued feedback and advice.

I would also like to thank the staff of the University of Adelaide Electrical Engineering Workshop for their assistance with my laboratory work as well as my fellow colleagues with whom I have had the pleasure of collaborating, in particular Dr. David Whaley and Dr. Vlatka Zivotic-Kukolj.

I would like to thank my family for their faith in me and lastly my wife, June for her endless support and encouragement.

This thesis was supported by Australian Research Council Discovery Grant DP0342874.

Nomenclature

β_n	normalised magnetic saturation parameter
δ	the angle between the back-emf E and the output voltage V_o of an electrical machine
ω_e	electrical frequency
Ψ_m	magnet flux linkage
ξ	saliency ratio of an interior PM machine
C	DC link capacitance
d	PWM duty-cycle
E	induced back-EMF of an electrical machine
Gm	gain margin of a transfer function
I_d	d-axis current
i_d	time-varying d-axis current
I_f	field current in an alternator winding
I_q	q-axis current
i_q	time-varying q-axis current
I_{IN}	DC current before the SMR switch
I_{LOAD}	current delivered to a load
I_{OUT}	DC current after the SMR switch
I_{qn}	normalised q-axis current

I_{SW}	DC current flowing through the SMR switch to ground
K_p	proportional gain of a closed-loop controller
L_d	d-axis inductance
L_q	q-axis inductance
L_{dn}	normalised d-axis inductance
L_{qno}	normalised unsaturated q-axis inductance
L_{qn}	normalised q-axis inductance
R_L	load resistance
R_n	normalised resistance
R_S	stator resistance
R_T	total resistance
R_{ph}	stator resistance of an electrical machine
T	reaction torque of an electrical machine
T_s	sampling time of a closed-loop controller
V_d	d-axis voltage
v_d	time-varying d-axis voltage
V_o	open-circuit voltage of an electrical machine
V_o	output voltage
V_q	q-axis voltage
v_q	time-varying q-axis voltage
V_s	line voltage of an electrical machine
V_{DC}	DC link voltage
V_{EFF}	effective voltage seen at the terminals of an electrical machine

V_{max} maximum voltage obtained on a voltage-current locus

X_d d-axis reactance

X_q q-axis reactance

Z_S source impedance

Abbreviations

AC	Alternating Current
CPSR	Constant Power Speed Ratio
DC	Direct Current
FET	Field Effect Transistor
LCD	Liquid Crystal Display
PWM	Pulse-Width Modulation
SAE	Society of Automotive Engineers
SLI	Starting, Lighting and Ignition
SMR	Switched-Mode Rectifier
UCG	Uncontrolled Generation
VI	Voltage-Current

Chapter 1

Introduction and Background

1.1 Introduction to Alternators

An alternator is a device that converts mechanical energy to alternating electrical current. The term normally refers to the small Alternating Current (AC) generators found in automotive vehicles, where mechanical energy is supplied by a combustion engine. In these vehicles, the alternator is usually coupled via a belt system to the engine drive shaft and generates electricity both to charge the battery of the vehicle and to supply electrical loads, most importantly for engine Starting, Lighting and Ignition (SLI) but also including air-conditioning, heating, pumps, wiper motors and various other on-board systems (see Fig. 1.1) [1].

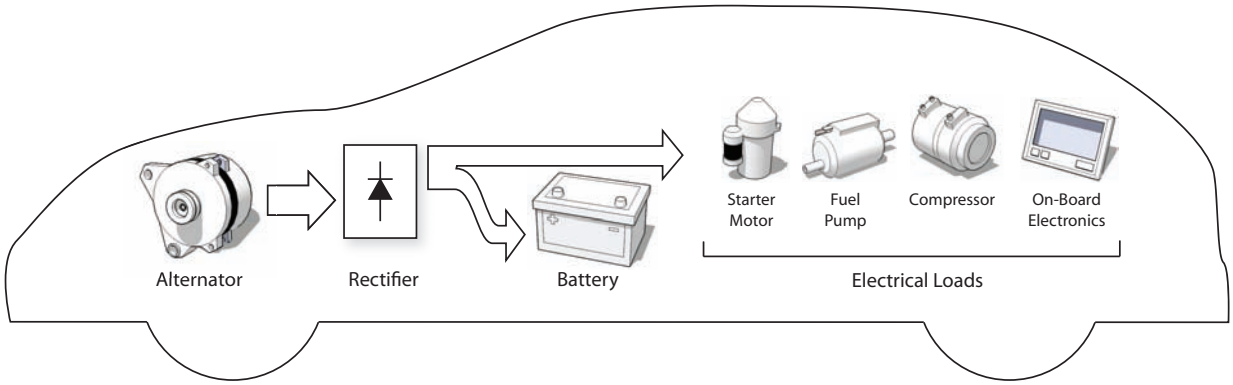

Figure 1.1: *Power generation, storage and usage in an automotive electrical system*

The alternator was first developed in the 19th century by pioneers such as Michael Faraday and Nikola Tesla. The first large-scale introduction of alternators in cars was

to replace the Direct Current (DC) generators previously used for powering the vehicle electrical system. While various improvements to the alternator have since been made, its basic design remains unchanged. The most commonly used modern alternator topology is known as the Lundell alternator (see Fig. 1.2), which is a three-phase, wound-field synchronous machine of a simple claw-pole rotor design with an integrated rectifier and regulator. The steel claw-pole design of the Lundell alternator is mechanically robust and can be cheaply manufactured. A reasonable amount of maintenance is required, usually due to wear of brushes and slip rings. The Lundell alternator produces 1-2 kW of output power and achieves approximately 50% efficiency from shaft to output [1].

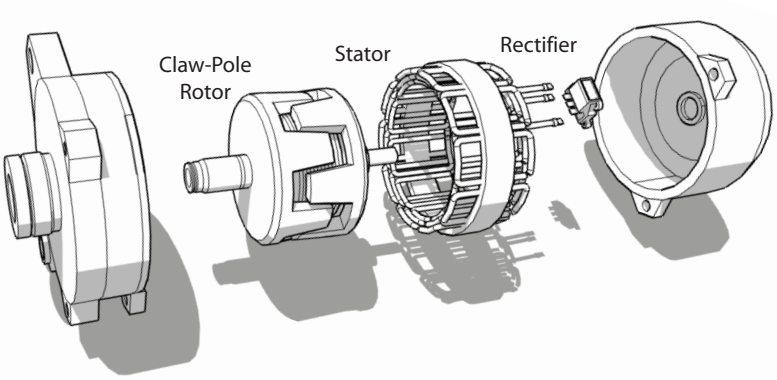

Figure 1.2: *Simplified diagram of a conventional Lundell alternator*

As with other AC generators, alternators work via the principle of electromagnetic induction. Mechanical power input to the alternator causes the rotor to turn relative to the stator. As the magnetic field of the rotor cuts across the stationary windings of the stator, an alternating voltage is induced. In the Lundell alternator, a field current, I_f is fed via slip rings and brushes to the rotor to produce its magnetic field.

The induced AC output voltage of the alternator is proportional to both the strength of the rotor magnetic field and the alternator speed. By changing the value of field current, the magnitude of the output voltage, V_s can be controlled. This is shown in (1.1), where the alternator speed is represented in terms of its electrical angular frequency, ω_e. The alternator three-phase output voltage is converted by an integrated bridge rectifier to DC, which is required by the electrical loads in a car.

$$V_s \propto \omega_e i_f \tag{1.1}$$

The output voltage of the alternator is kept constant by the integrated regulator which monitors the output voltage and adjusts the current in the field winding to increase or decrease the magnetic field of the rotor and thus control the output voltage (1.1). The presence of the car battery as a load also helps to absorb any voltage ripples or disturbances such as load changes caused by other electrical devices in the car being turned on or off.

An alternator is faced with the task of providing sufficient output power to supply the electrical accessory loads over the entire operating speed range of the car engine. This typically ranges from an idle speed of 600 rpm to a top speed of 6,000 rpm and since the alternator output power is generally proportional to speed, producing sufficient power at low speeds is particularly challenging. Alternators are therefore commonly run with a belt ratio of 3:1 to obtain a higher rotational speed of 1,800 rpm at engine idle.

The surplus power generated by the alternator is used to maintain the battery charge level. This is important because when the engine is not running, any active devices must draw their power from the battery alone, e.g. the starter motor used to crank the engine. A typical consumer vehicle has a 12 V lead-acid battery and the alternator output is slightly higher at 14 V in order to provide a suitable charging voltage. The battery generally has a capacity of around 80 Ah and may be called upon to supply currents as large as 200 A for engine cranking.

Ideally, an alternator should maximise output power and efficiency while minimising the cost of manufacture and maintenance. Mounted near the engine of a vehicle, the alternator is exposed to constant vibration and high temperatures, thereby reducing its performance and lifetime.

1.2 Trends in Power Consumption

The demand for electrical power in vehicles has been steadily rising, as shown in Fig. 1.3. With the conventional Lundell alternator limited to 1-2 kW of output power, newer vehicles are already approaching the limits of the Lundell alternator's capability. The graph of Fig. 1.3 was published in 2000 and shows the projected electrical power demand in cars up to 2005.

The increase in power demand has largely been driven by the plethora of new features being introduced into vehicles to provide increased performance, safety and comfort. Some of these applications, such as active suspension and electromechanical valve timing, re-

Figure 1.3: *Graph of historical and projected electrical demand in cars [2], and breakdown of electrical demand in generic luxury vehicles in 1996 and 2005 [3]*

quire large currents in order to achieve the desired mechanical effect. Active suspension involves using actuators to actively control the suspension system of a vehicle in order to enhance the smoothness of travel or even adjust the grip of the vehicle on the road surface. Electromechanical valve timing describes the replacement of the mechanical cam shafts used to control engine valves by electrical actuators, allowing the valve timing to be fully and dynamically controlled in order to optimise fuel efficiency and engine power in varying conditions.

A further contributing factor to increased electrical power demand is the gradual replacement of engine-driven devices such as water pumps, air-conditioning compressors and power-steering pumps with electrical alternatives. This relieves the mechanical load on the engine and reduces maintenance needed by moving parts such as belts and drive clutches. This change also results in greater fuel efficiency, particularly for devices which see intermittent use, e.g. an air-conditioning compressor.

Apart from improvements to the basic functionality of the vehicle, various auxiliary on-board systems are also becoming increasingly popular and affordable, such as satellite navigation, video entertainment systems and even small inverters to power mains-voltage appliances such as laptop computers. These ever-increasing demands to be placed on the next generation of automotive electrical systems highlight the need for a high-power successor to the Lundell alternator.

1.3 High Power Alternators

1.3.1 High Power Alternator Requirements

In the mid to late 1990s, the Massachusetts Institute of Technology (MIT)/Industry Consortium on Advanced Automotive Electrical/Electronic Components and Systems [4] provided several recommendations in an effort to formulate and standardise solutions for addressing the high power demands of future vehicles. The main points can be summarised as follows:

- *More power* - output power ranging from 4 kW at engine idle speed (600 rpm) to 6 kW at top speed (6,000 rpm), corresponding approximately to a constant power speed range of 10:1
- *Better efficiency* - a requirement of 75% system efficiency at 75% load at 1,500 rpm engine speed (4,500 rpm alternator speed assuming a 3:1 pulley ratio)
- *Higher and better regulated output voltage* - strict voltage limits around a 42 V output voltage as specified by the 42V Powernet specification

The requirements for output power and efficiency are considerably higher than those achieved by a conventional Lundell alternator and are illustrated in Fig. 1.4. A useful metric relevant to this output power requirement is the constant power speed range (CPSR) of a machine, which is the range of operating speed over which a machine is capable of producing rated power. If the rated speed is defined as the speed at which rated power and torque are produced, the CPSR is expressed as the ratio of the maximum speed at which rated power is obtainable to the rated speed. The high power alternator specification is approximately equivalent to a CPSR ratio of 10:1.

1.3.2 42V Powernet Specification

The shift from the existing 14 V electrical system voltage to a 42 V system, as recommended by the Consortium, represents a significant development in the automotive industry. The preceding shift from 7 V to 14 V did not entail such an extensive change to the electrical system because the only electrical loads present at the time were for starting, lighting and ignition, whereas electrical devices are now pervasive in modern vehicles. The main reason for this move is to improve the efficiency of the electrical system - the three-fold increase in system voltage allows a three-fold reduction of the current required

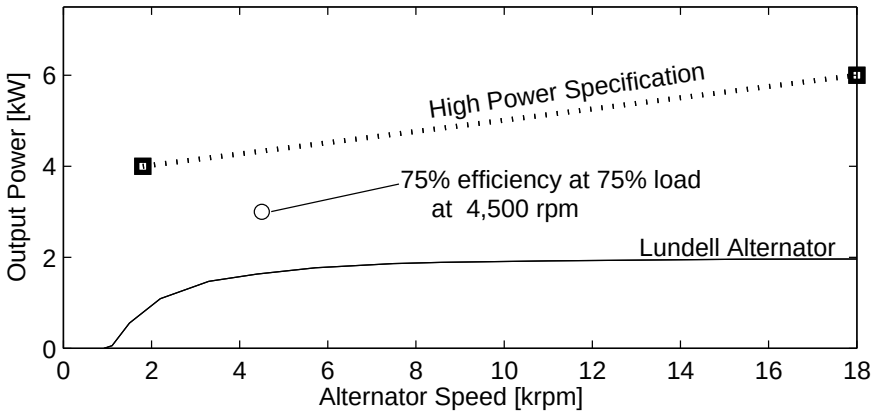

Figure 1.4: *High power alternator specification, showing power and efficiency requirements*

to deliver the equivalent power to car loads. This results in a nine-fold reduction in copper losses alone, which is especially important at the higher levels of output power specified.

Originally an initiative of Mercedes Benz and the Massachussets Institute of Technology, the next-generation automotive electrical system based on a 42 V system voltage is formalised in the Society of Automotive Engineers (SAE) 42V Powernet specification. The operating voltage of 42 V was originally chosen because it was the highest possible multiple of 14 V which satisfied the internationally established safe peak voltage limit of 60 V while allowing a reasonable voltage margin for transients. By offering reduced I^2R transmission losses, the higher operating voltage also allows the use of lighter wiring and insulation. The resulting weight reduction also translates to savings in fuel.

The 42 V specification enforces strict voltage regulation (see Fig. 1.5), reducing the need for device over-rating and thus leading to cost savings at the component level. The overall savings can be significant - it is estimated that the cost of an automotive electrical system exceeds that of the engine and transmission combined and that the electrical wiring harness typically makes up more than 35 kg of a vehicle's weight [5].

Some issues remain to be addressed in the adoption of the 42 V standard. One of these is the increased risk of arcing at the high levels of voltage involved and another is the problem of jump-starting [6]. Dual 12 V and 42 V rail systems have also been investigated in order to ensure compatibility with existing 12 V lighting and accessories while the industry transitions to the new standard [7].

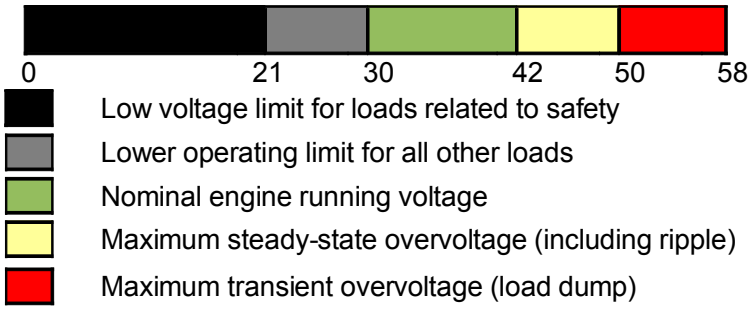

Figure 1.5: *Operating voltage limits for the 42V Powernet specification*

1.3.3 Load Dump Transients

Although the integrated regulator of an alternator monitors its output voltage, the car's electrical system may still experience large disturbances in certain extreme situations, such as when the connection to the battery is lost while the alternator is running. Without the battery to absorb the generated power, the alternator voltage climbs sharply. The regulator employs field current control to regulate the output voltage and thus cannot respond instantaneously - the inductance of the field winding prevents the field current from changing quickly. This condition is known as a *load dump* and the associated transient voltage peak can be as large as 80 V and last for hundreds of milliseconds [8, 9].

In order to cope with the voltage transient, electrical components throughout the car must be over-rated to withstand voltages much higher than the operating voltage. As more higher power devices are incorporated into vehicles, the cost of the necessary device over-rating grows. The introduction of more sophisticated and sensitive electronics also means that the power quality of the car's electrical supply becomes increasingly important in a next-generation vehicle.

1.3.4 Machine Types

Research into viable high power automotive alternators has turned to various types of electrical machines, including other wound-field synchronous machines, induction machines (IM), switched reluctance machines, surface permanent magnet (SPM) and interior permanent magnet (IPM) machines. The performance achieved in early studies with these machines is summarised in Fig. 1.6, with the curve for the conventional Lundell alternator shown for reference.

While it would be possible to scale an existing 14 V wound-field Lundell alternator for

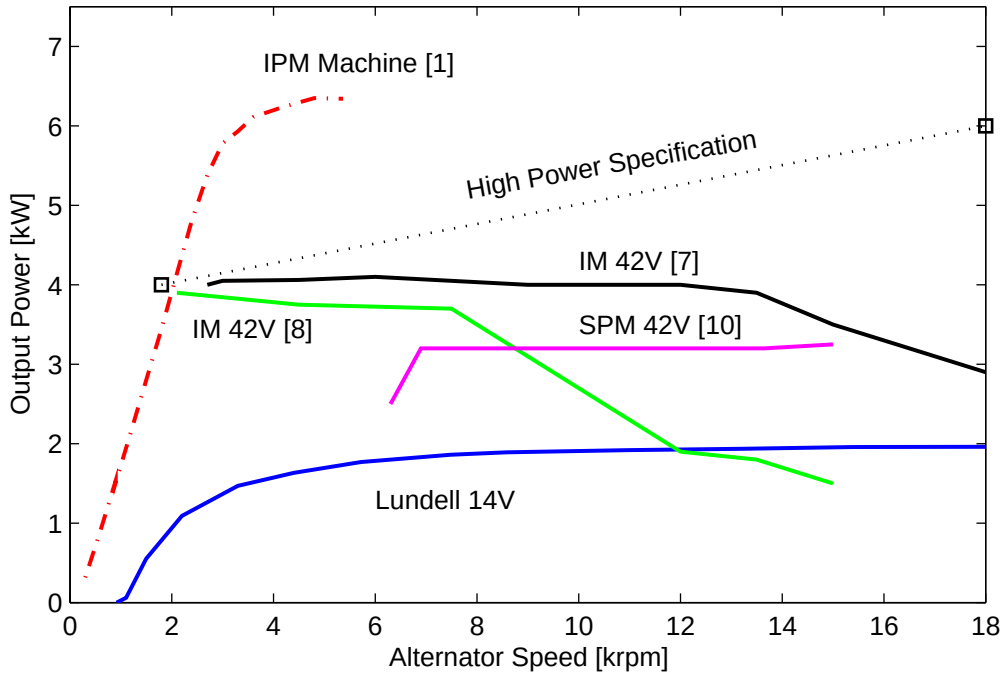

Figure 1.6: *Comparison of power vs. speed curves achieved by various types of electrical machines*

42 V output by tripling the number of winding turns in the stator, this would not change its output power.

The asynchronous or induction machine is very widely used in industrial applications and has the benefit of being robust and relatively inexpensive. Work on induction machines as automotive alternators has achieved maximum output powers of around 4 kW, however this power tends to fall off at engine speeds beyond 4 krpm [10, 11, 12] (see Fig. 1.6).

The switched and variable reluctance machines are attractive because of their simple construction and high efficiency. Their inert rotors without windings or magnets are inexpensive and robust, making them suitable for operation at high speed and in high temperature conditions [13]. However, they do suffer from significant torque ripple, vibration and noise.

Permanent magnet (PM) machines have also attracted significant interest in alternator applications. As the rotor magnetic field is provided by magnets instead of field windings, PM machines offer high efficiency and power density which allow for a more compact design.

Although improvements in manufacturing have helped reduce the cost of permanent magnets, it is worth noting that in recent years, the price of rare-earth magnet materials has risen by over an order of magnitude. This has been due to reduced supply and tighter export limitations imposed by China since 2005, which at the time supplied more than 90% of the global rare-earth metal demand. While there has been a ramping up of rare-earth production in other countries as well as increased pressure on China to loosen export controls, this situation remains an economic concern for permanent magnet applications.

1.3.5 Field Weakening

As shown in Fig. 1.6, one of the main challenges faced has been that of meeting the output power requirement specification - the output power of the machine must be maintained above the specification line for all engine speeds from 600 rpm to 6,000 rpm (see Fig. 1.4), i.e. the machine must deliver rated voltage and current over that operating speed range.

The back-emf of electrical machines is proportional to the product of the speed and the flux in the machine. In machines where the flux is relatively constant, such as surface PM machines, it is difficult to operate above rated speed without exceeding the rated output voltage. This could be solved by employing a DC-to-DC converter to maintain a constant output voltage. However, at top speed the power electronic components in the converter would be required to withstand both rated current (150 A, for 6 kW at 42 V) and the considerable machine back-emf of several hundred volts. This approach therefore involves increased power electronics cost and complexity.

Another method to maintain rated voltage is to reduce the flux in the machine, as for example in the Lundell alternator, where this is accomplished by reducing the field current and thus the magnetic field of the rotor (see (1.1)). Figure 1.7 shows how if at above rated speed the alternator terminal voltage and armature current are kept at rated values and the field current is decreased inversely proportionally to the speed, the torque likewise decreases with $1/\omega_e$. The output power, being the product of torque and speed, thus remains constant. Operating at above rated speeds in this fashion is known as *field-weakening* and makes it theoretically possible to achieve a very high Constant Power Speed Ratio (CPSR).

A study by Schiferl and Lipo showed that interior PM machines offer the best field-weakening performance of any AC synchronous machine and thus have the potential to achieve a wide CPSR [14]. This study also described the optimal field-weakening condition for interior PM machines (1.2), where the magnet flux-linkage Ψ_m is equal to the d-axis

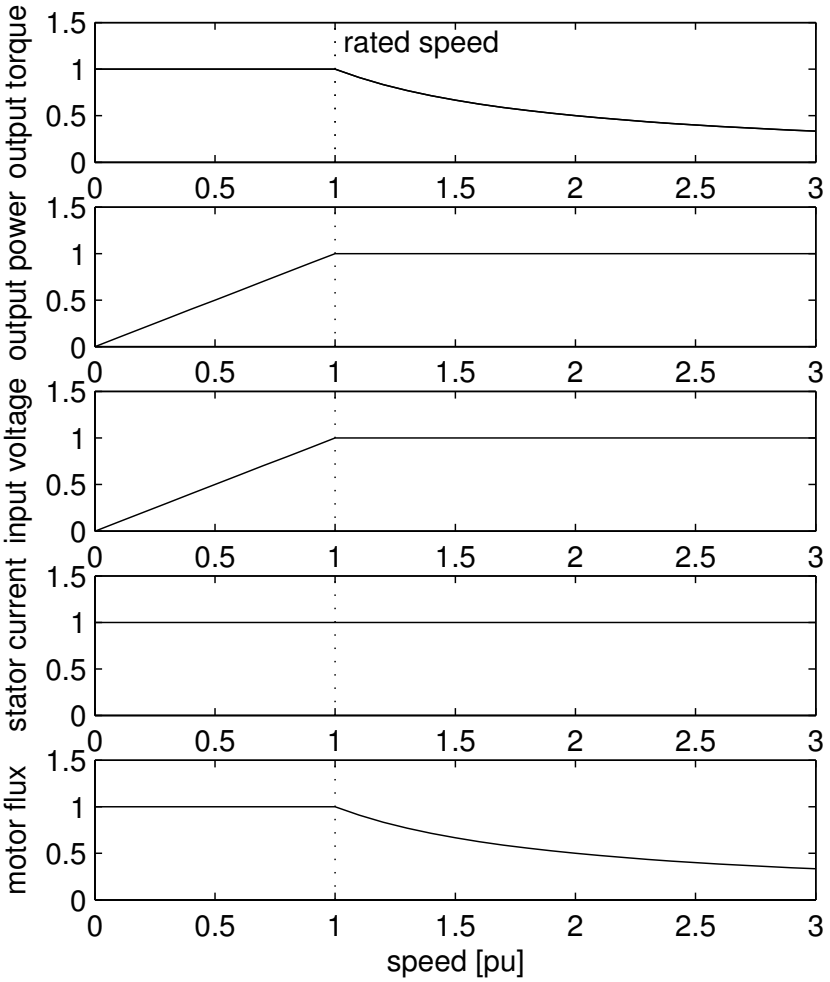

Figure 1.7: *Machine parameters under field-weakening operation*

stator inductance L_d multiplied by the rated stator current I_o.

$$\Psi_m = L_d I_o \tag{1.2}$$

1.3.6 Power Conversion

The three-phase AC output of an alternator must be converted to a DC current suitable for charging the battery of a vehicle. Several circuit configurations which are capable of achieving this are shown in Fig. 1.8.

The simplest means of producing a DC output is the three-phase bridge rectifier (see

Fig. 1.8.a) and this is the configuration commonly used in conventional automotive alternators. If the DC link voltage of the rectifier is increased by a factor of three from 14 V to 42 V then this would increase the output power at high speeds by a factor of three as shown in Fig. 1.9. It would however also increase the speed at which generation starts by a factor of three and reduce the idle speed output power to zero.

The configuration which delivers the most power at any speed from an alternator is an inverter (see Fig. 1.8.b). An inverter has two independently controlled switches per phase-leg which can be used to modify the phase and amplitude of the current and voltage waveforms in order to extract maximum power from the machine. This provides maximum power transfer but at the cost of additional power electronics switches and a more complex control system.

Semi-bridge (see Fig. 1.8.c) and single-switch (see Fig. 1.8.d) Switched-Mode Rectifiers (SMRs) represent intermediate steps between the inverter and the bridge rectifier. Previous work by Perreault has investigated the use of a Lundell alternator with a semi-bridge switched-mode rectifier in place of a bridge rectifier [9]. By modulating the SMR switches with a Pulse-Width Modulation (PWM) signal of controllable duty, the effective load voltage seen by the alternator could be manipulated in order to obtain power at all speeds. Later work by Rivas examined a phase advance SMR modulation scheme which could improve Lundell alternator output power at idle speed [15].

The various power converter topologies will be discussed in more detail in later chapters but the output power obtained from a Lundell alternator with each configuration is shown in Fig. 1.9 for the purpose of comparison.

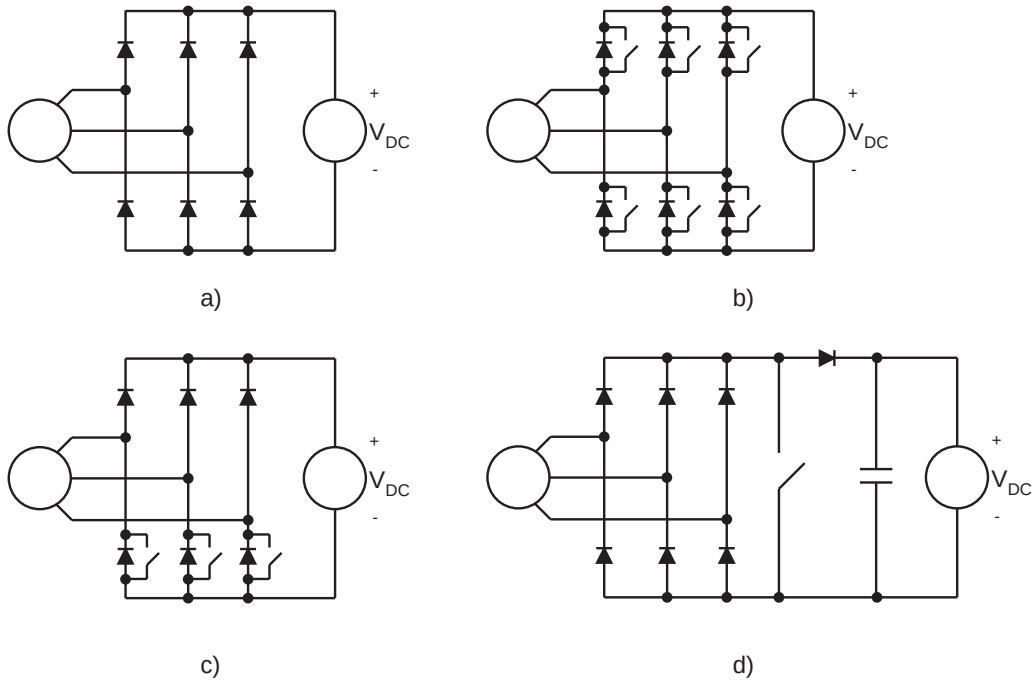

Figure 1.8: *Three-phase AC machines operating into a DC voltage source load via: a) a bridge rectifier, b) an inverter, c) a semi-bridge SMR, and d) a single-switch SMR*

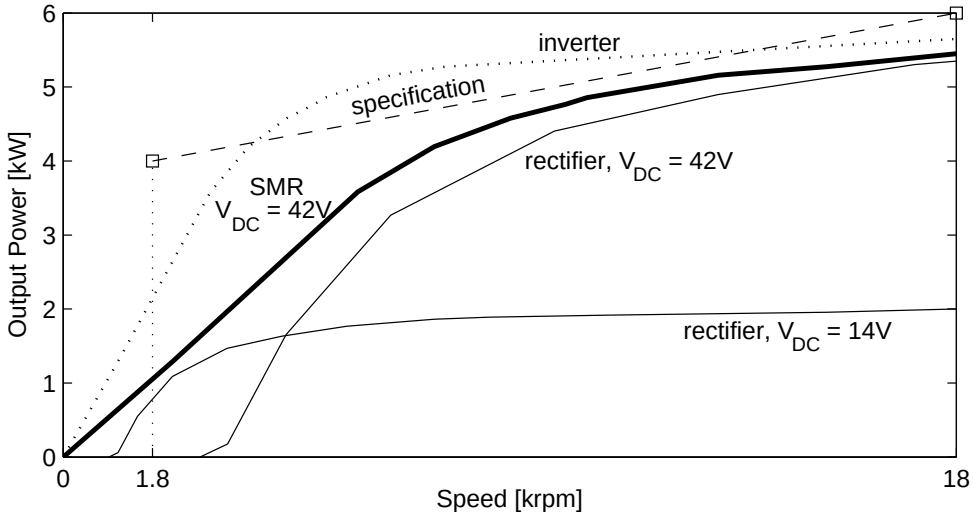

Figure 1.9: *Output power obtained from a Lundell alternator using different power converter configurations*

1.3.7 Inverterless Alternator Concept

Previous work by Soong and Ertugrul has investigated the field-weakening capability of an interior PM generator and produced promising preliminary results with a specially-designed concept demonstrator of an 'inverterless' alternator [16]. The inverterless alternator is so called because the inverter normally used in interior PM machine operation (see Fig. 1.10a) is replaced by a switched-mode rectifier (SMR) consisting of a three-phase rectifier and a controllable switch (see Fig. 1.10.b).

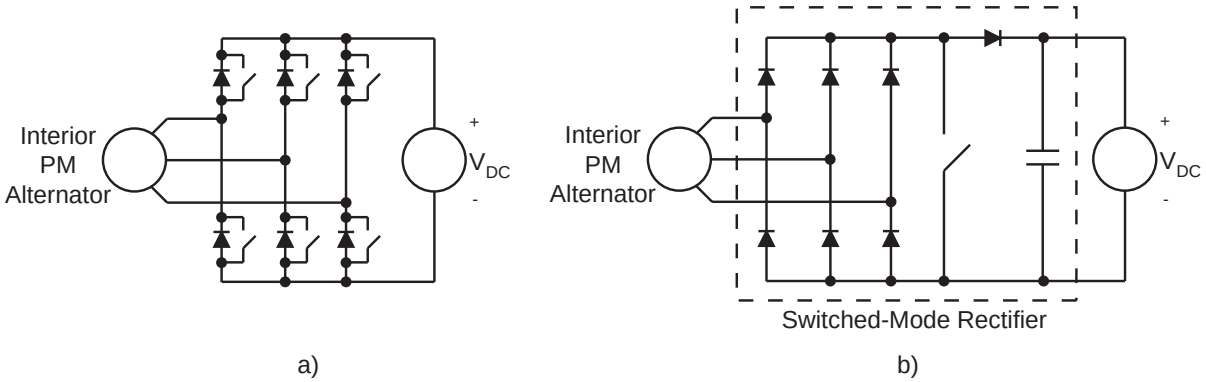

Figure 1.10: *Interior PM alternator in a) inverter configuration and b) inverterless configuration*

The interior PM machine was designed for near-optimal field-weakening performance in order to obtain a wide CPSR by meeting the condition described in (1.2). Under this condition, the machine stator current asymptotes towards a maximum value of rated current at high speeds, so that the single switch of the SMR is only required to cope with rated current and voltage. Thus the the total switch volt-ampere rating of the single-switch SMR is much lower than that of an inverter.

The interior PM machine was designed with a high back-emf relative to the rated output voltage, allowing it to act as a controllable current source at high speeds when operated with an SMR. This gives it a wide CPSR and allows for a simple method of output voltage regulation. At low speeds, where the machine back-emf is less than the DC link voltage, the single-switch SMR acts as a boost converter, however since it is generating into a fixed DC voltage source, controlling the SMR switch duty-cycle does not change the DC link voltage but has the effect of varying the voltage seen at the machine terminals between 0 V and the DC link voltage. This enables the alternator to perform load-matching, which improves power transfer in a manner similar to that demonstrated

by Perreault in his work with a Lundell alternator [9]. Although this configuration uses two less switches and one more diode than the semi-bridge rectifier in Perreault's study, the effect of the switching is similar, since Perreault used a single control signal for all three SMR switches.

The inverterless interior PM alternator offers a wide CPSR, obtained using fewer switches and simpler control as compared to an inverter. As position sensors are not necessary and lower switch VA ratings are allowed, the cost of this configuration is further reduced. Preliminary studies with the interior PM machine using a variable three-phase resistive load to simulate load-matching performance showed promising results, achieving more than 6 kW of power at 4 krpm (see Fig. 1.6) [16].

1.3.8 Recent Developments in 42 V Power Electronics and Related Work

The majority of the work in this thesis (2003-7) was carried out at a time of significant interest in the 42 V automotive electrical system specification. However, as of 2012, there has been only limited commercial adoption of this standard and some in the industry are of the opinion that 42 V is no longer on the horizon [17].

In part, this has been due to vehicle and component manufacturers weighing the long-term benefits of a higher system voltage against the immediate cost and time required to redevelop the extensive and well-established 14 V infrastructure. With heavy economic pressure in many countries, vehicle makers may be more inclined to reduce commercial risk by investing in projects which result in an immediate, obvious benefit to consumers. Some of this focus has gone into the development of hybrid and electric vehicles, for which there is a growing market in the face of increasing petroleum prices. The integrated starter/alternator, which has been one of the major applications of a 42 V electrical bus and intended to improve fuel economy, is already employed in several current hybrid-electric vehicles; for instance, the Hybrid Synergy Drive in the Toyota Prius, which operates with a 200 V battery pack and uses an inverter to raise the voltage to 650 V DC to drive the electric motor [18].

Other reasons given for the difficulty in adopting the 42 V standard include problems with the lack of standardisation of 42 V connectors, safety issues with test and repair of 42 V systems in the field and reduced reliability of 42 V components. The latter is due to the larger arcs and subsequent contact erosion occurring in switches and relays under the higher voltage which thus requires a redesign of these components to improve their

reliability [19].

Such issues are not insurmountable given sufficient incentive, however this must be accomplished "within realistic R&D budgets that reflect the economics of our times" [20]. On the one side, we have hybrid-electric vehicles such as Toyota's Prius, which have already moved ahead with a higher voltage bus and battery to cater for increased power demand, while using a DC/DC converter to charge a separate 12 V battery and power existing 14 V accessories. On the other side, some of the electrical issues to be addressed by the 42 V standard such as growing wiring losses and weight have been somewhat mitigated by manufacturers using techniques such as wire multiplexing, and some of the features previously requiring more power such as electrical power steering can now operate properly under 14 V as a result of ongoing development [17].

Considering the many benefits of a higher voltage architecture, some see the move to a higher standard voltage as only being put off for a time by advances in other areas. Whilst any prediction regarding the fate of the 42 V standard would be speculation, the standard does continue to act as a common focus for research efforts, with many of the outcomes being potentially scalable and applicable regardless of the standard the industry eventually adopts. A brief look at recent publications reveals continuing and varied research [21, 22, 23, 24, 25, 26] into 42 V alternators and associated power converters, which will be discussed in the following section.

1.3.9 Literature Review on Automotive Alternator Developments

In this subsection a brief outline is provided of the range of existing research conducted with the aim towards developing alternator technology with suitable output power, efficiency and cost-effectiveness for 42 V automotive applications. Specifically, the scope of this thesis in relation to the existing research is summarised in Table 1.1, in terms of the type of machine and power electronics used.

- Henry et al. [11] implemented a prototype belt-driven induction machine starter-generator for 42 V systems, utilising an inverter. This system was capable of producing an output power of approximately 4 kW, however at higher speeds this was reduced, e.g. to 2 kW at 4,000 rpm. The overall efficiency of the alternator and the power electronics was between 73% and 79%.

- Naidu et al. [10] constructed a surface PM alternator with a single SCR bridge rectifier being used to regulate the output voltage, producing 3.4 kW of output

power up to 6,500 rpm, with 71% full-load efficiency at that speed.

- Carrichi et al. [27] constructed a 3 kW surface PM starter-alternator using Litz wire winding to reduce winding losses and thus improve efficiency at higher speeds. An inverter was used as the power converter and a full-load efficiency of 96% was achieved at 3,000 rpm.

- Liang et al. [28] employed six-step inverter control with a Lundell alternator and obtained a 43% increase in output power at idle speed.

- Lovelace et al. [29] found that the major factor in the cost of the alternator and power electronics was in fact the cost of the inverter. This highlights a benefit of employing a switched-mode rectifier as opposed to the more complex and costly inverter.

- Perreault et al. [9] investigated the application of half-bridge SMR control to a Lundell alternator in order to extract more power through load-matching. Load-matching allowed the output power of the alternator to increase linearly from 1 kW at an idle speed of 1,800 rpm to approximately 4 kW at 6,000 rpm whereas with a conventional diode rectifier the output power would be limited to 1.5 kW.

- Rivas et al. [15] introduced a phase advance SMR modulation scheme to increase the output power of a Lundell alternator power at idle speed. This scheme was implemented with a half-bridge SMR and produced a 15% increase in output power at idle speed.

In the time since the work in this thesis was carried out, there have been further related studies, as follows:

- Shrud et al. [21] developed an analytical model and simulated the performance of a 42 V Lundell alternator and rectifier system.

- Stoia et al. [22] investigated the design parameters of a 42 V Lundell alternator for use with an integrated single-switch SMR.

- Mudannayake et al. [23] investigated the performance of a 42 V integrated starter/alternator (ISA) based on a 5.5 kW induction machine, implementing stator voltage control with an inverter to extract more output power at high speeds and regulate output voltage.

- Xueyi et al. [24] analysed the operation of a 42 V rare-earth PM alternator using a semi-bridge SMR for rectification and output voltage regulation.
- Xiao et al. [25] implemented a bidirectional power converter for a 42 V ISA using indirect space vector modulation.
- Sai et al. [26] designed and tested a 42 V Lundell alternator with an integrated switched-mode rectifier for output power improvement and transient load dump control.

Table 1.1: *Existing high-power alternator research categorised by machine and type of power electronics*

	Wound-Field	**Induction**	**Surface PM**	**Interior PM**
Inverter	Liang et al. [28]	Henry [11], Naidu [10], Mudannayake et al. [23]	Naidu [30], Carrichi [27]	Lovelace [29], Xueyi et al. [24]
SMR	Perreault et al. [9], Rivas et al. [15], Stoia et al. [22], Sai et al. [26]		Whaley et al. [31], Pathmanathan [32]	*This Work*

There has also been research closely related to and continuing on from the work in this thesis. Whaley et al. [31] investigated the application of a high-inductance PM alternator with a SMR and commutated H-bridge inverter as a novel grid-connected inverter for small-scale wind turbines. Pathmanathan investigated the output power capability of surface PM machine with an SMR [32] and also devised a simplified phase-advance modulation scheme to maximise output power from a surface PM machine [33], obtaining an output power improvement of almost 60%. Pathmanathan also applied phase-advance modulation for maximum torque-per-ampere control of SPM wind generators [34].

1.3.10 Original Contributions

This thesis focuses on the investigation of an interior PM automotive alternator with an SMR as the power converter. Compared to other machine types which have been studied, the high power density, compact size, high efficiency and excellent field-weakening

performance of the interior PM machine makes it a promising candidate for development as a next-generation, high power automotive alternator with a wide CPSR.

The key contributions of this work are summarised as follows:

- Analysis of the generation characteristics of the interior PM machine when operating into a resistive/voltage source load, including the development of steady-state and dynamic models capable of predicting the machine output.
- Introduction of the VI locus as a tool in the steady-state modelling of electrical machines and its application to modelling the effects of saliency, magnetic saturation and stator resistance on interior PM alternators and in particular the hysteresis in the output current.
- Experimental validation of the developed models, including output current hysteresis in an interior PM machine, which has not previously been experimentally demonstrated.
- Investigation and modelling of SMR-based control of the interior PM machine output and experimental demonstration of alternator output power maximisation through load-matching. Demonstration of closed-loop voltage regulation and transient suppression using the SMR.
- Dynamic modelling of a phase-advance modulation scheme to improve the output power of the interior PM alternator at idle speed. Implementation and testing of the phase-advance modulation scheme on a microcontroller.

1.3.11 Thesis Layout

This thesis is divided into several chapters which examine different aspects of the interior PM machine relevant to this application:

- Chapter 2 covers the fundamental theory governing the generation characteristics of PM machines and discusses several interesting aspects particular to interior PM machines, such as saliency and voltage overshoot.
- Chapter 3 investigates the behaviour of the interior PM machine when a SMR is employed to control the output power. A simple closed-loop controller is examined to evaluate the performance of the alternator as a regulated voltage source.

- Chapter 4 investigates the use of a phase advance SMR modulation technique to improve the output power of the alternator at idle speed, thereby allowing it to meet the 42V high power alternator output power specification.
- Chapter 5 summarises the key findings and original contributions of this work and outlines areas of potential for further investigation.

Chapter 2

Interior PM Alternator Characteristics

This chapter examines the operating principles of the interior permanent magnet machine in its function as an alternator. The behaviour of the interior PM machine during generation operation is analysed, in particular the case of generation into a DC voltage source load.

The concept of the Voltage-Current (VI) locus is introduced to illustrate the behaviour of the interior PM machine in this operating mode, with attention to the phenomenon of stator current hysteresis. Theoretical models are developed for both steady-state and dynamic situations in order to predict the currents and voltages present in the interior PM machine, taking into account the effects of saliency, DC link voltage and non-idealities such as magnetic saturation and stator resistance. Lastly, experimental results from two different test machines are presented and compared against theoretical predictions.

2.1 Introduction to Permanent Magnet Machines

A brushless permanent magnet machine is a form of synchronous AC machine in which the magnetising flux of the rotor is supplied by permanent magnets rather than a field winding. They are generally divided into surface PM and interior PM machines, the latter being distinguished by having magnets embedded inside the rotor, rather than mounted on the rotor surface (see Fig. 2.1).

Some of the general advantages of brushless PM machines over other machine types are their high efficiency and power density and therefore attractiveness in applications

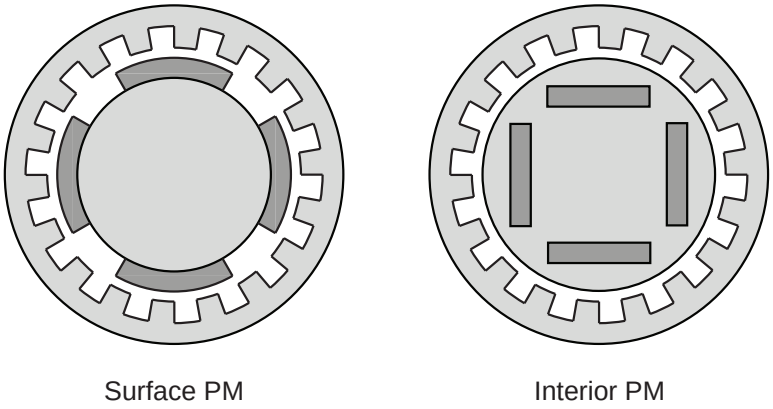

Figure 2.1: *Cross-sections of a surface PM and an interior PM machine*

requiring compact size. Since the flux is provided by permanent magnets, machine excitation losses are eliminated. On the other hand, PM machines are susceptible to demagnetisation if the magnetic field generated by the stator winding currents become too high. This can be prevented by avoiding excessive stator currents during operation.

One of the main reasons for using an interior PM machine as an alternator in this study is its good field-weakening performance. This gives the interior PM machine an advantage over the surface PM machine as it is then easier to achieve a high CPSR - one of the requirements implicit in the high power alternator specification. Additionally, the interior PM machine torque has contributions from both magnet and reluctance torque, allowing a higher torque density.

A surface PM machine can be modelled as the machine back-emf voltage, E in series with the synchronous inductance, L_s and resistance, R_s (see Fig. 2.2). L_s is the inductance of the path taken by magnetic flux within the machine due to the stator current, which in the case of the surface PM machine can be considered to be constant for all rotor angles, as the magnets mounted on the rotor surface have a permeability close to that of air. The synchronous inductance is relatively small due to the large electromagnetic airgap.

In an interior PM machine, however, the path taken by the flux is complicated by the presence of the magnets embedded in the rotor. The characteristics of the interior PM machine are accordingly more complex and are described in this chapter as the *d-q* model of the interior PM machine is examined.

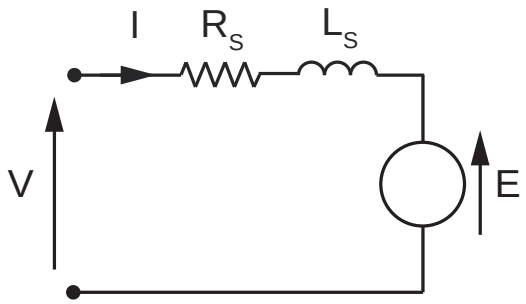

Figure 2.2: *Equivalent circuit model for a surface PM machine*

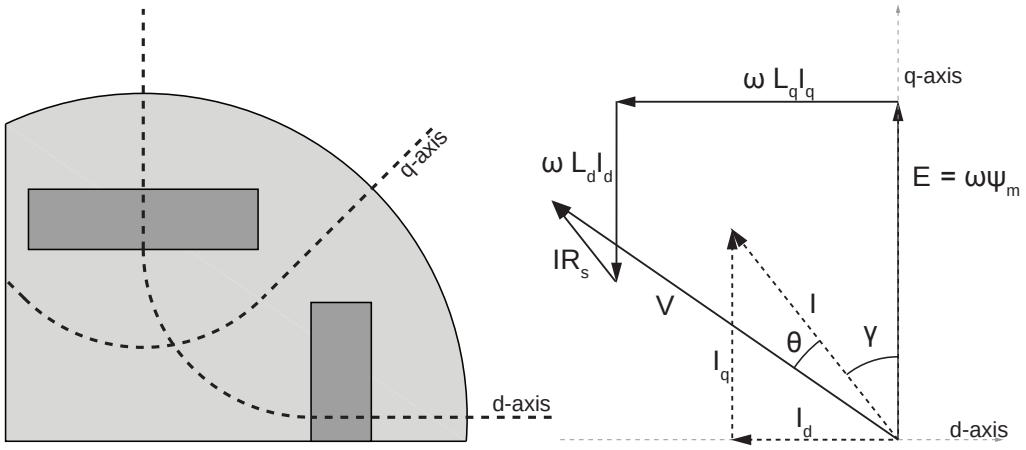

Figure 2.3: *Interior PM machine rotor indicating synchronous d-q frame axes and phasor diagram of currents and voltages during operation (the effect of stator resistance is neglected)*

2.1.1 Interior PM Machine *d*-*q* Model

The synchronous *d*-*q* model defines flux flowing in two orthogonal axes in the rotor frame of reference - the *direct* or *d*-axis and the *quadrature* or *q*-axis, as indicated in Fig. 2.3. The *q*-axis flux follows a path through the solid body of the rotor which in most cases is made of steel, whereas the *d*-axis flux path passes through the magnets in the rotor. The magnet flux linkage, Ψ_m lies in the positive *d*-axis and thus the induced back-emf, $E = \omega_e \Psi_m$ appears in the positive *q*-axis.

The steady-state phase equations for the *d* and *q*-axis voltages V_d and V_q of the *d*-*q* model can be derived from the phasor diagram of Fig. 2.3.

$$V_q = R_s I_q + \omega_e L_d I_d + \omega \Psi_m \tag{2.1}$$

$$V_d = R_s I_d - \omega_e L_q I_q \tag{2.2}$$

$$\text{Output torque, } T = \frac{3}{2} p \left(\Psi_m I_q - (L_q - L_d) I_d I_q\right) \quad \text{where } p = \text{number of pole-pairs} \tag{2.3}$$

In contrast with the surface PM machine, the inductance in the d- and q-axes differ. The magnetic permeability of the magnets is close to that of air and thus the effective air-gap in the d-axis is larger than in the q-axis. As a result, the q-axis inductance, L_q is higher than the d-axis inductance, L_d.

The ratio of the q-axis inductance to the d-axis inductance is known as the saliency ratio $\xi = L_q/L_d$ and is an important parameter which determines the field-weakening performance and torque characteristics of the machine. The saliency in the rotor causes a reluctance torque proportional to $(L_q - L_d)$ to be produced, in a similar fashion to a synchronous reluctance machine. This reluctance torque is in addition to the magnet alignment torque, together comprising the total output torque in interior PM machines, from (2.3).

As the stator current flowing in an interior PM machine is increased, the magnetic flux flowing through the stator and rotor iron increases and at some point begins to saturate. Saturation can reduce both the d and q-axis inductances at higher operating currents. This reduction is less evident in the d-axis due to the larger effective airgap.

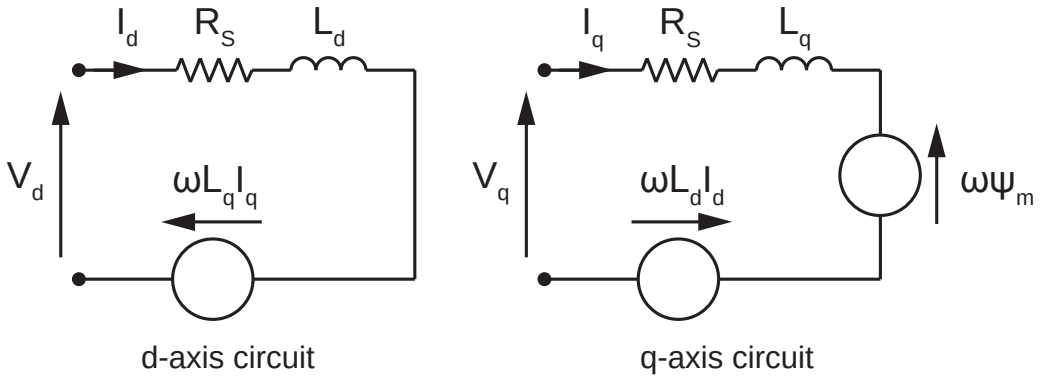

Figure 2.4: *Equivalent circuits for an interior PM machine in the d-axis and the q-axis*

The d- and q-axis equivalent circuits for an interior PM machine corresponding to

(2.1) and (2.2) are given in Fig. 2.4, where the controlled voltage sources represent the interaction between the d-axis and q-axis circuits.

2.1.2 Generation in Interior PM Machines

Although interior PM machines have recently experienced increased popularity in motoring applications because of their efficiency and compact size, their use as generators has been limited. This is partly because unlike the wound-field Lundell alternator, there is no direct control of the magnetic flux being provided by the magnets in a PM machine and therefore in order to control the voltage or current output of an interior PM machine and maximise its power transfer to a load, additional power electronics is needed.

In this study the interior PM machine acts as an alternator, delivering power via a rectifier to supply various electrical devices in a vehicle and to charge a battery, which is modelled by a DC voltage source load (see Fig. 2.5.a).

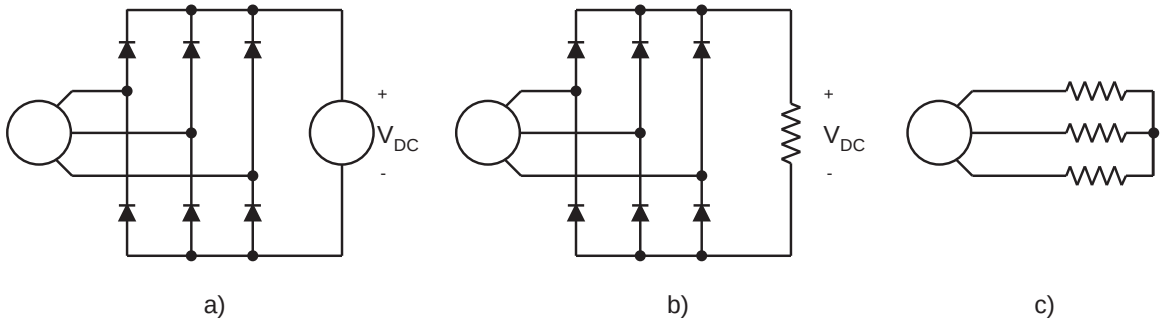

Figure 2.5: *Equivalent circuits for uncontrolled generation : a) rectifier and voltage source load, b) a rectifier and resistive load and c) a three-phase resistive load*

2.2 Uncontrolled Generation

The condition shown in Fig. 2.5.a has been previously studied, albeit as a fault mode occurring in inverter-fed interior PM machines during motoring operation. This is known as Uncontrolled Generation (UCG) and it occurs when the switches of the inverter driving an interior PM machine are disabled while the machine is operating at a sufficiently high speed where the induced back-emf exceeds the DC link voltage. Under this condition, the inverter freewheeling diodes act as an uncontrolled rectifier and the machine generates power into the DC link. While uncontrolled generation is undesirable during motoring

operation, it can be seen from Fig. 2.5.a that this is essentially the same configuration as when an interior PM alternator provides power to a DC voltage source load such as a car battery.

The fault currents generated during UCG operation can be undesirably large in motoring applications and hence an early investigation by Adnanes concerned the calculation of these fault current magnitudes in PM machines [35]. In the case of Adnanes' study, the fault currents involved were large because of the low inductance and hence high short-circuit current of the interior PM machines investigated.

In order to theoretically model the fault currents in UCG, the voltage source load of Fig. 2.5.a can be simplified to an equivalent resistance, giving a rectifier and resistive load (see Fig. 2.5.b). This can be further simplified using the findings of Caliskan [36], who analysed three-phase rectifiers with a constant voltage load and an ac-side reactance, which in the case of UCG is the machine inductance. Caliskan's study offered a simplified analysis based on the assumptions that:

- the machine phase currents are balanced, sinusoidal and free of harmonics during operation;

- the rectifier forces the phase currents to be strictly in phase with the phase voltages (viewed from the generator convention).

Caliskan showed that almost all of the real power is transmitted to the voltage source load in the fundamental of the phase current waveform. Provided the above assumptions are valid, the rectifier and voltage source load can be approximated by a three-phase resistive load (see Fig. 2.5.c).

While the first assumption is generally valid over most of the speeds of interest for the machines used in this study, it may not hold at very low machine speeds where the phase currents tend to become non-sinusoidal. The second assumption is a known property of waveforms in a rectifier.

Further investigations into UCG included a more detailed theoretical analysis and steady-state modeling of UCG in interior PM machines by Jahns [37], which takes into account magnetic saturation but assumes zero stator resistance. This model also predicts a hysteresis effect for high saliency machines. A study into fault modes of PM machines by Welchko [38] also introduced a time-stepping dynamic *d-q* model which takes into consideration various transient effects.

2.2.1 Steady-State Model

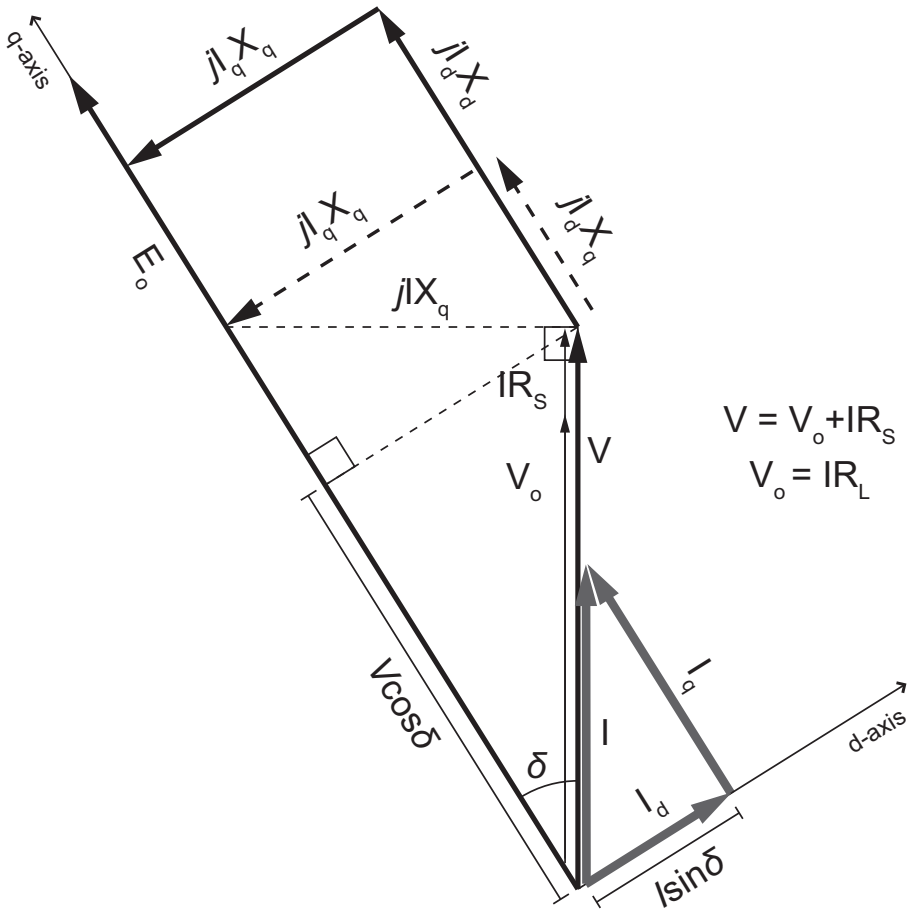

Figure 2.6: *Phasor diagram for an interior PM machine operating into a resistive load*

The currents and voltages in an interior PM machine operating in UCG can be represented by the phasor diagram in Fig. 2.6, which corresponds to equations (2.1) and (2.2).

The standard method for analysing salient-pole synchronous generators starts from knowledge of the magnitudes of the output voltage **V** and the output current **I**, as well as the phase difference between **V** and **I**. From these, the magnitude of the induced voltage $\mathbf{E_0}$ and the rotor angle δ between $\mathbf{E_0}$ and **V** can be determined from equation 2.4.

$$\begin{aligned} &\delta = \angle(\mathbf{V} + j\mathbf{I}X_q), \text{ hence } E_0 = V\cos\delta + I_d X_d \\ &\text{where the } d\text{-axis current component } I_d = I\sin\delta \end{aligned} \tag{2.4}$$

The steady-state model used by Jahns [37] to analyse interior PM machines in UCG also starts from a known output voltage (set by the DC link voltage) during UCG operation and the back-emf magnitude, E_0, and solves for the two unknowns of rotor angle, δ and current magnitude I. Jahns' model uses the assumptions of the simplified UCG analysis mentioned above. Additionally, the model assumes that the effects of stator resistance and magnetic saturation are negligible.

The steady-state model used in this study retains the assumptions of sinusoidal phase currents and a three-phase resistive load, but instead of assuming a known output voltage, it uses a known load resistance, R_L. In this model, the stator resistance, R_S can be taken into account by combining it with the load resistance so that the machine sees a total resistance of $R_T = (R_S + R_L)$. The actual output phase voltage present across the three-phase resistive load is $\mathbf{V}_o = \mathbf{I}R_L$ but the effective output voltage is $\mathbf{V} = \mathbf{I}(R_S + R_L)$. As the load is purely resistive, $\mathbf{V}$ and $\mathbf{I}$ are in phase and related by the resistance R_T but neither the magnitude of $\mathbf{V}$ nor $\mathbf{I}$ are known.

To determine the rotor angle, δ, the imaginary vector $\mathbf{V} + j\mathbf{I}X_q$ can be used to obtain the following expression for δ:

$$\begin{aligned} \tan\delta = \frac{IX_q}{V} = \frac{IX_q}{I(R_L + R_S)} = \frac{\omega_e L_q}{R_L + R_S} \\ \text{hence } \delta = \arctan\left[\frac{\omega_e L_q}{R_L + R_S}\right] \end{aligned} \tag{2.5}$$

$$\begin{aligned} E_0 = V\cos\delta + I_d X_d \\ = I(R_L + R_S)\cos\delta + I\sin\delta \end{aligned} \tag{2.6}$$

$$\mathbf{V}_o = \mathbf{I}R_L. \tag{2.7}$$

The current can then be found by expressing the magnitude of $\mathbf{E_0}$ as in (2.6) and rearranging (2.5) for I. The magnitude of the output voltage $\mathbf{V}_o$ is then found simply by (2.7).

Magnetic saturation was accounted for in this model by treating the d and q-axis inductances as a function of their respective axis currents. While this neglects cross-saturation effects, it still produces reasonably accurate results, particularly for high saliency machines

such as those considered in this study. The functions $L_d(I_d)$ and $L_q(I_q)$ are obtained from experimental inductance measurements of the machines used in this study. A spline curve fit to the data was used to provide values to the simulation, which iterates until the values of inductance converge.

An approximate normalised non-linear parametric model of magnetic saturation was developed by Jahns [37] based on experimental data, and this will be used in later sections to examine the effect of saturation without being machine specific. This model is described by (2.8), where L_{qno} is the unsaturated value of L_{qn} when I_{qn} is zero, and β_n determines the degree to which L_{qn} is affected by saturation as illustrated in Fig. 2.7. This model assumes that the value of L_{dn} is constant with respect to I_{dn} and thus unaffected by saturation.

$$L_{qn} = L_{dn} + \frac{(L_{qno} - L_{dn})}{[1 + (\beta_n I_{qn})^2]^{1/2}} \tag{2.8}$$

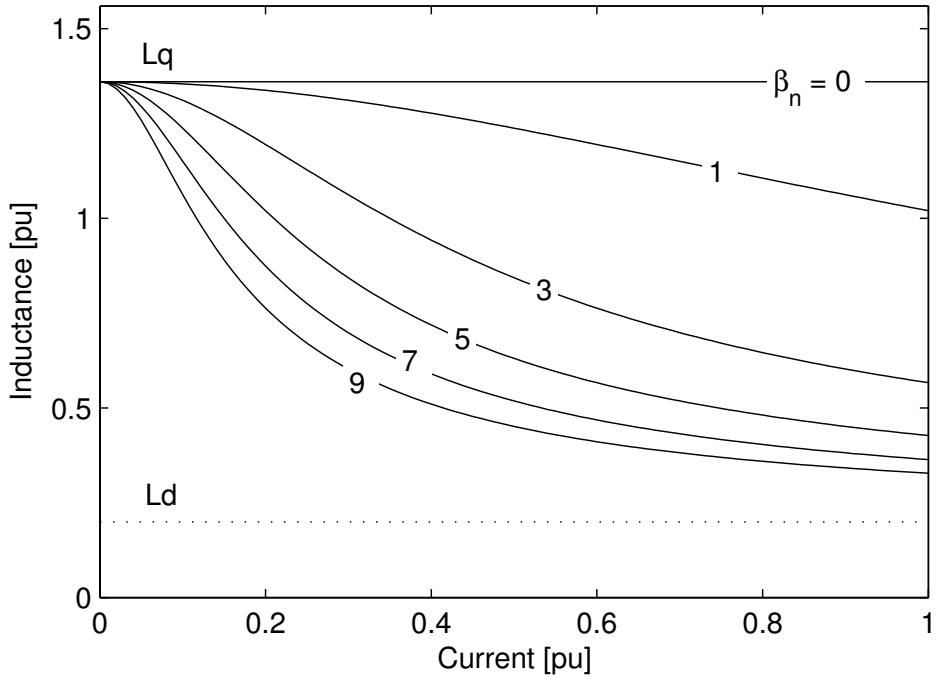

Figure 2.7: *D and q-axis inductances as a function of current, for various levels of magnetic saturation parameter β_n from Jahns' model of magnetic saturation [37], for $\xi = 6$*

2.2.2 Dynamic Model

The dynamic model used in this study was a Simulink time-stepping simulation based on the model developed by Welchko [38]. The following are the dynamic *d-q* equations for the interior PM machine upon which the model is based, including the effects of stator resistance and magnetic saturation:

$$v_q = R_S i_q + L'_q \frac{di_q}{dt} + \omega_e L_d i_d + \omega_e \Psi_m \tag{2.9}$$

$$v_d = R_S i_d + L'_d \frac{di_d}{dt} - \omega_e L_q i_q \tag{2.10}$$

$$\text{where } L'_q = L_q + \frac{\delta L_q}{\delta i_q} i_q \text{ and } L'_d = L_d + \frac{\delta L_d}{\delta i_d} i_d$$

The advantage of the dynamic model is that it can predict transient as well as steady-state effects in the system, however the simulations are more time-consuming. Magnetic saturation is taken into account in this model by using a piecewise inverse exponential curve fit to the measured inductance curves.

2.3 Voltage-Current Loci in Uncontrolled Generation

It has been shown that the voltage source load in UCG can be approximated as a three-phase resistive load [36]. Measuring the machine output voltage and current over a range of different resistive load values produces a voltage-current or VI locus. This is a useful tool which, to the author's knowledge, has not previously been used to visualise the behaviour of interior PM machines. It will be applied here to illustrate various aspects of the machines in this study.

A number of electrical machines can be modelled as a voltage source with some series impedance, Z_S (see Fig. 2.8). For instance, a DC generator can be modelled by a DC voltage source and series resistance. When the output is considered over a range of values of resistive load, this circuit behaves as a voltage divider and the VI locus is thus a straight line between the machine's open-circuit voltage at infinite load resistance and its short-circuit current at zero load resistance (see Fig. 2.9). A non-salient surface PM machine can be similarly modelled as an AC voltage source and series inductance L. An equation can be written for the output voltage and current (2.11) which is in the form of an ellipse

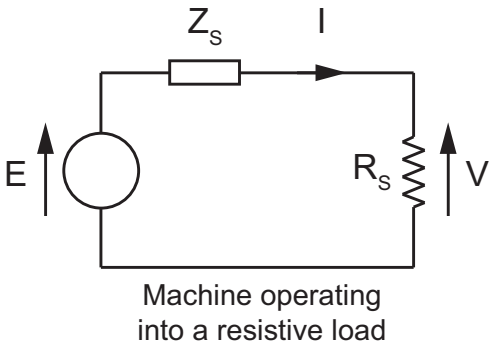

Figure 2.8: *Single-phase equivalent circuit of an electrical machine modelled as a voltage source with series impedance while operating into a resistive load*

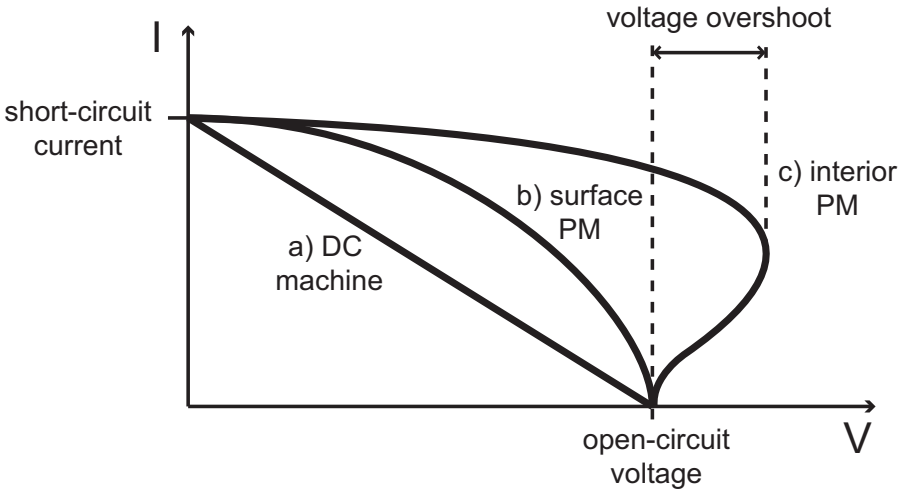

Figure 2.9: *Voltage-current loci for DC, surface PM and interior PM machines*

and so a semi-circular locus is obtained.

By Kirchhoff's Voltage Law,

$$V = \sqrt{E^2 - I^2(\omega L)^2} \tag{2.11}$$

The voltage-current locus of an interior PM machine may be similarly found from (2.6) and (2.7). Under certain conditions, a highly salient interior PM machine may exhibit an interesting feature whereby a portion of its voltage-current locus exceeds the open-circuit voltage (see Fig. 2.9). This means that for certain non-zero values of stator current, the machine can produce an output voltage which is greater than the open-circuit voltage.

This unusual effect has been termed 'voltage overshoot' and its magnitude is governed by the machine's saliency ratio.

Consider the interior PM machine operating at a certain electrical frequency ω_e. The d-q equations can be normalised using the base units defined in (2.12) to (2.14). Normalising (2.1) and (2.2) produces (2.15) and (2.16) and from these it can be clearly seen that the parameters affecting the shape of the voltage-current locus are the saliency ratio ξ and the normalised stator resistance R_n, which is a function of the stator resistance R_s, the d-axis inductance L_d and electrical frequency ω_e. This normalises the VI locus to a unity value for both open-circuit voltage and (high-speed) short-circuit current.

$$V_{base} = \omega_e \Psi_m \tag{2.12}$$

$$I_{base} = \Psi_m / L_d \tag{2.13}$$

$$R_{base} = V_{base} / I_{base} = \omega_e L_d \tag{2.14}$$

$$V_{qn} = 1 + I_{dn} + R_n I_{qn} \tag{2.15}$$

$$V_{dn} = -\xi I_{qn} + R_n I_{dn} \tag{2.16}$$

$$\text{where } R_n = \frac{R_s}{\omega_e L_d} \tag{2.17}$$

2.3.1 Saliency Ratio

In the ideal case where the stator resistance R_s is neglected, the R_n terms in (2.15) and (2.16) disappear. The only factor determining the shape of the VI locus is then the saliency ratio, ξ of the interior PM machine. As illustrated in Fig. 2.10, a saliency ratio of $\xi = 1$ would mean that the rotor is non-salient and the VI locus would be semi-circular, exhibiting no overshoot. Voltage overshoot only occurs for interior PM machines with $\xi \geq 2$ and the amount of overshoot increases almost linearly with increasing saliency ratio (see Fig. 2.11).

It was chosen to define voltage overshoot as the difference between the maximum voltage V_{max} on the VI locus and the machine open-circuit voltage V_o, expressed as a percentage of V_o, i.e. $overshoot\% = (V_{max} - V_o)/V_o \times 100\%$.

With the R_n term eliminated, the shape of the normalised VI locus does not change

with respect to speed. As the open-circuit voltage increases proportionally with speed, the VI locus likewise scales proportionally in the voltage axis (see Fig. 2.12). The short-circuit current remains constant since the stator reactances also scale with speed.

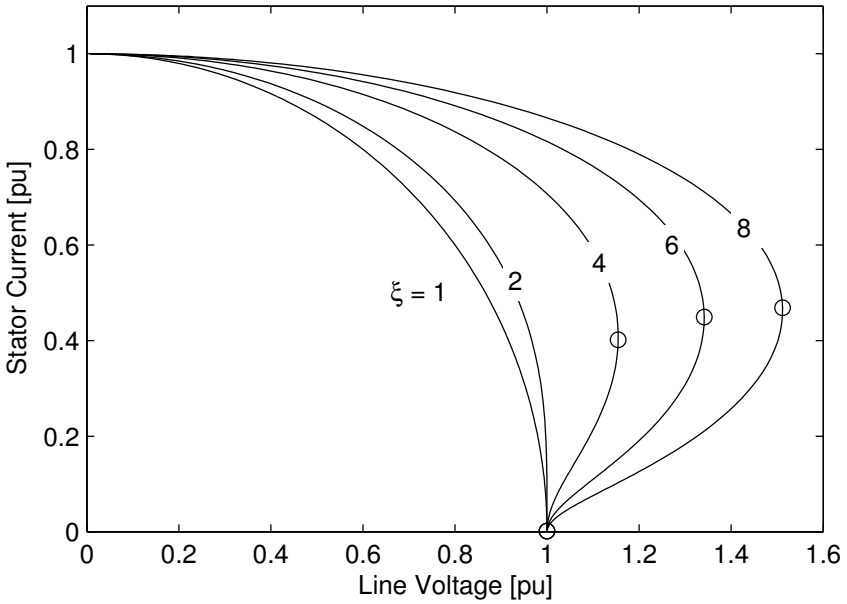

Figure 2.10: *Normalised voltage-current loci for various saliency ratios ξ, neglecting the effects of stator resistance and saturation. The peak output voltage points are indicated with circles.*

2.3.2 Stator Resistance

In practice, the non-zero stator resistance of an interior PM machine can have a significant effect on the shape of its VI locus, as illustrated by Fig. 2.13, which shows the effect of increasing values of R_n for a machine with a saliency ratio of 6. It can be seen that stator resistance reduces both the short-circuit current and the maximum output voltage (as indicated on the loci by circles). Towards higher values of resistance, the shape of the locus starts to approach the straight line characteristic of a resistive impedance. This is not surprising since the resistance at this point dominates over the reactance in the machine output impedance. If loci are plotted over a larger range of stator resistance values, it can be shown that the reduction in short-circuit current and maximum output voltage is proportional to stator resistance.

As R_n is inversely proportional to the reactance $\omega_e L_d$, it follows that for a constant actual stator resistance R, that R_n will become large at low machine speeds. With higher

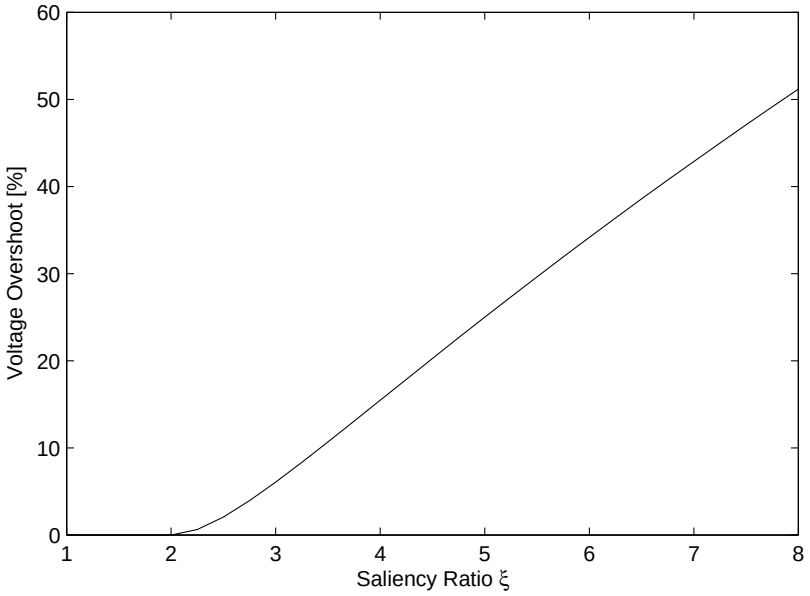

Figure 2.11: *Voltage overshoot versus saliency ratio ξ, neglecting the effects of stator resistance and saturation*

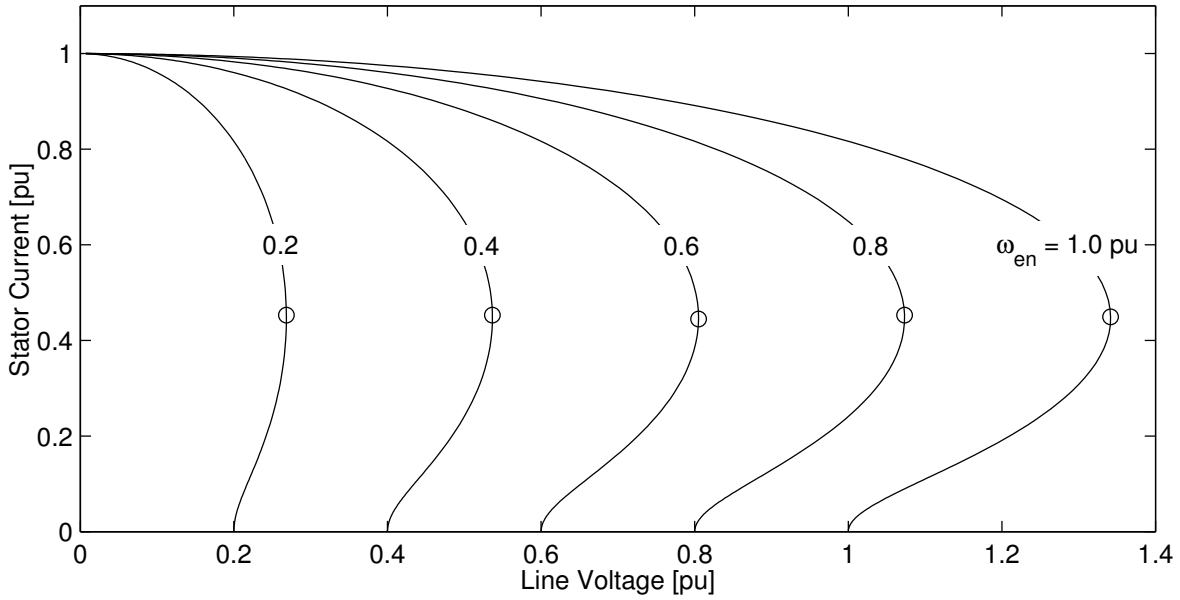

Figure 2.12: *Ideal voltage-current loci at various speeds ω_{en} for saliency ratio $\xi = 6$, $R_{ph} = 0$ pu*

speeds, the effect of stator resistance becomes relatively small compared to the increasing machine reactances. The resulting transition in the shape of the non-ideal VI locus with

speed is shown in Fig. 2.14

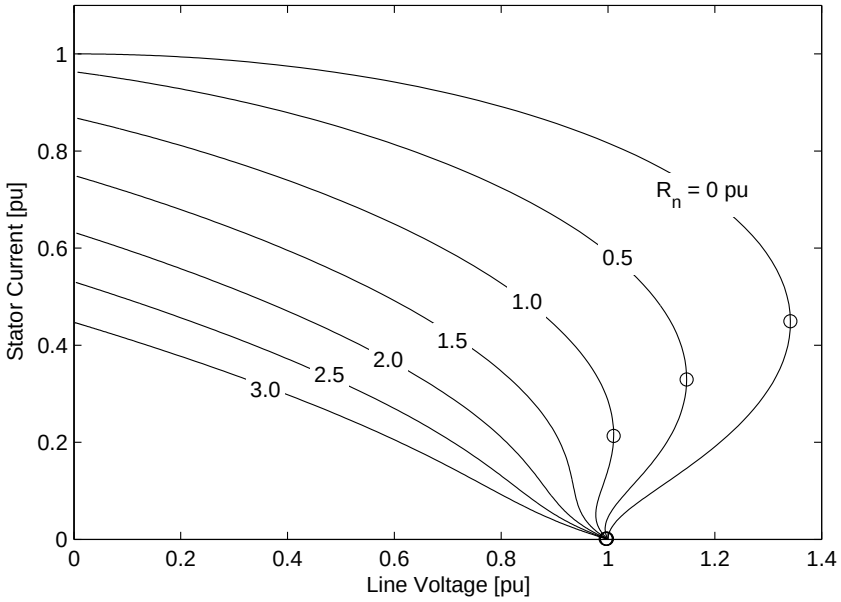

Figure 2.13: *Normalised voltage-current loci for various values of normalised stator resistance R_n, with $\xi = 6$*

The slope of the curve at the open-circuit point ($I = 0$), exhibits an interesting variation with resistance. With $R_n = 0$, the gradient of the curve, $\frac{dV}{dI} = 0$. For large values of stator resistance, a negative slope is observed, with $\frac{dV}{dI} \propto R_n$. The combination of a moderate value of stator resistance and a high saliency can cause a kink in the curve such that the slope is negative near the open-circuit point but becomes positive at higher currents as the effect of high saliency overcomes the effect of resistance. Thus a voltage overshoot is still obtained (see Fig. 2.13).

Whereas an ideal machine with zero stator resistance should have the same amount of voltage overshoot at any speed, the non-zero resistance of a practical machine means that voltage overshoot is only exhibited at sufficiently high speeds. This is illustrated in Fig. 2.15, which shows how the open-circuit voltage and the maximum output voltage of a machine start to diverge at a certain speed which is dependent on the stator resistance.

Figure 2.16 illustrates the relationship between voltage overshoot and R_n, plotted for various values of ξ. Two points are also plotted for the two machines used in this study, showing expected values of voltage overshoot of almost 40% and approximately 25% for the axially-laminated and multiple-barrier machines, respectively using a base speed of 1,500 rpm. These curves do not account for magnetic saturation, which further decreases

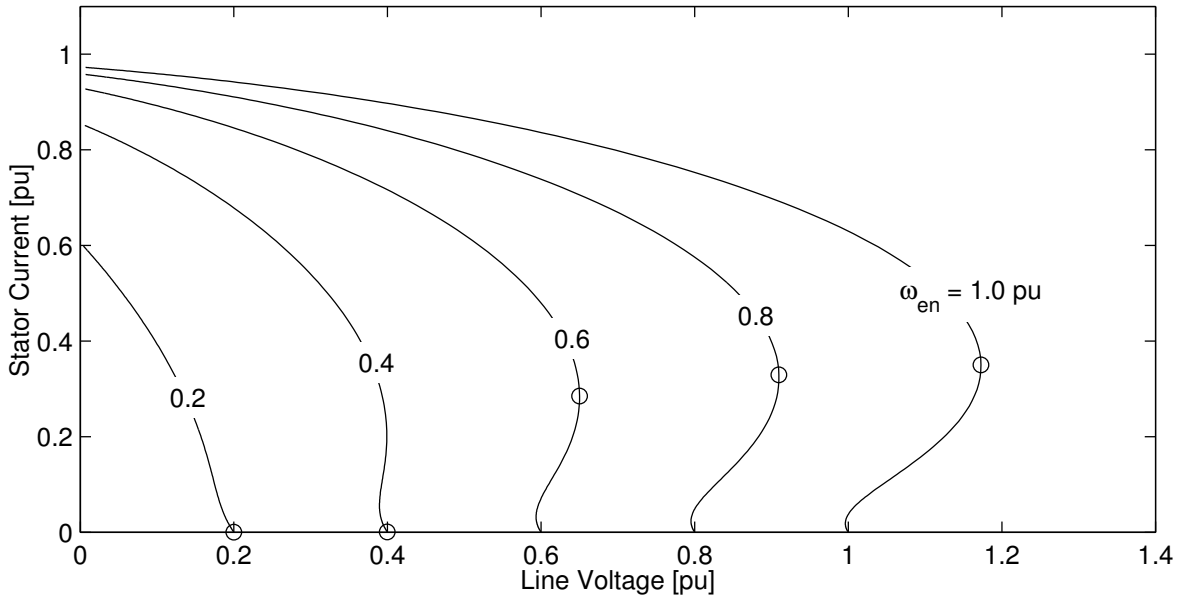

Figure 2.14: *Normalised voltage-current loci at various speeds ω_{en}, with $R_n = 0.42$ pu at base speed*

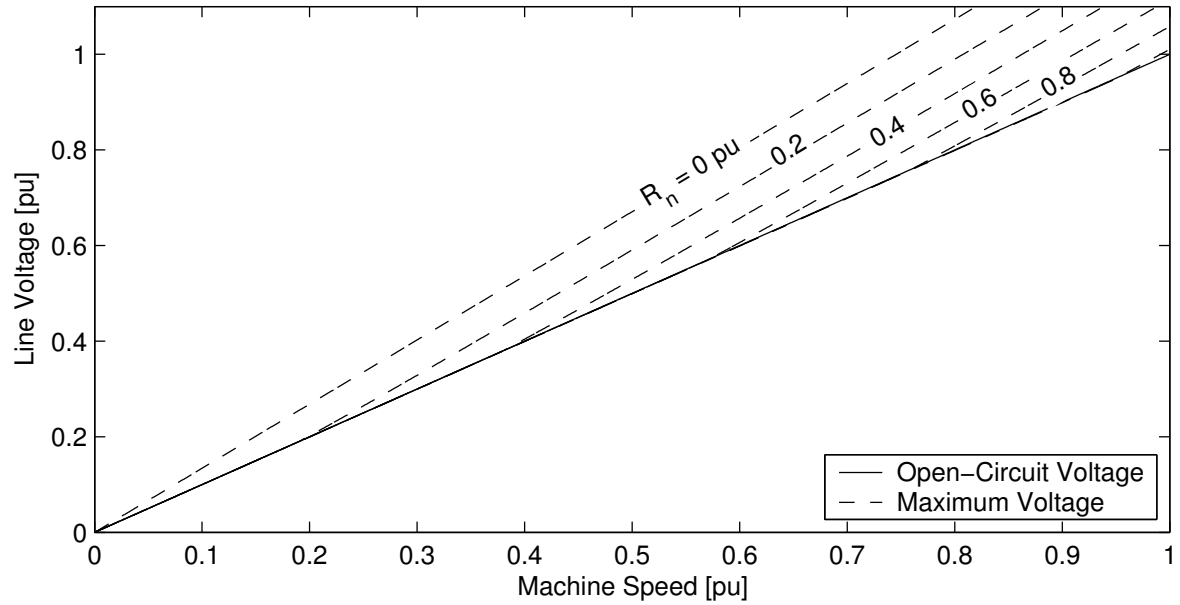

Figure 2.15: *Open-circuit voltage and maximum voltage vs. machine speed for various values of stator resistance R_n, with $\xi = 6$*

the voltage overshoot.

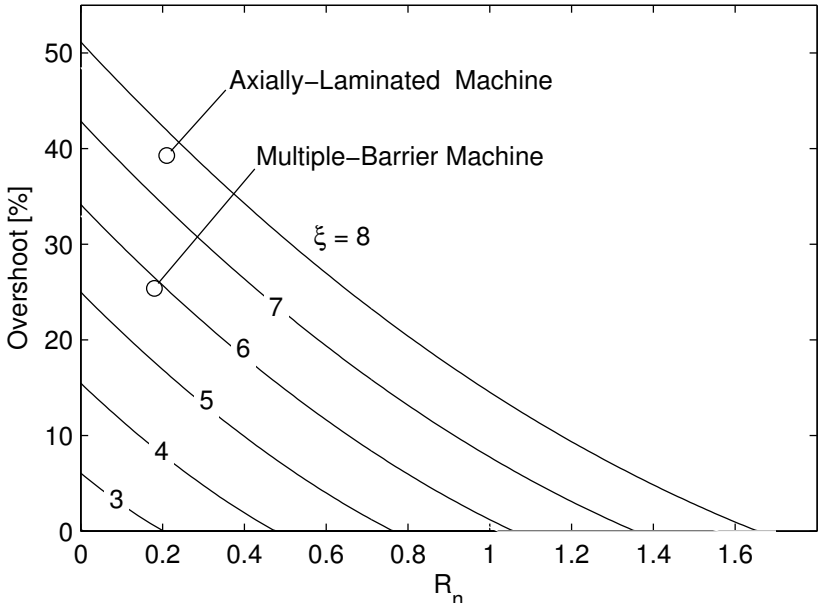

Figure 2.16: *Voltage overshoot versus R_n for various values of saliency ratio ξ, showing the locations of the two test machines based on their unsaturated saliency ratio and normalised stator resistance at 1,500 rpm*

2.3.3 Magnetic Saturation

Magnetic saturation effectively reduces the saliency ratio at high stator (q-axis) currents. As illustrated in Fig. 2.7, the reduction in the saliency is greater and occurs over a wider current range for high values of the saturation model parameter β_n. Shown in Fig. 2.17 are a range of loci for a machine with an unsaturated saliency ratio of 6 and zero stator resistance, as β_n is increased. Saturation can cause a considerable reduction in voltage overshoot in much the same way that reducing saliency does.

The voltage overshoot that can be observed in the VI loci of highly salient interior PM machines produces an interesting hysteretic phenomenon in their stator current vs. speed characteristic, which is discussed in the next section.

2.4 Stator Current Hysteresis

Hysteresis in the stator current versus speed characteristic of interior PM machines during uncontrolled generation was first discussed by Jahns [37], who modelled uncontrolled generation from the viewpoint of motoring operation, starting with knowledge of the DC link voltage supplied by an inverter and the machine back-emf magnitude. Jahns noted

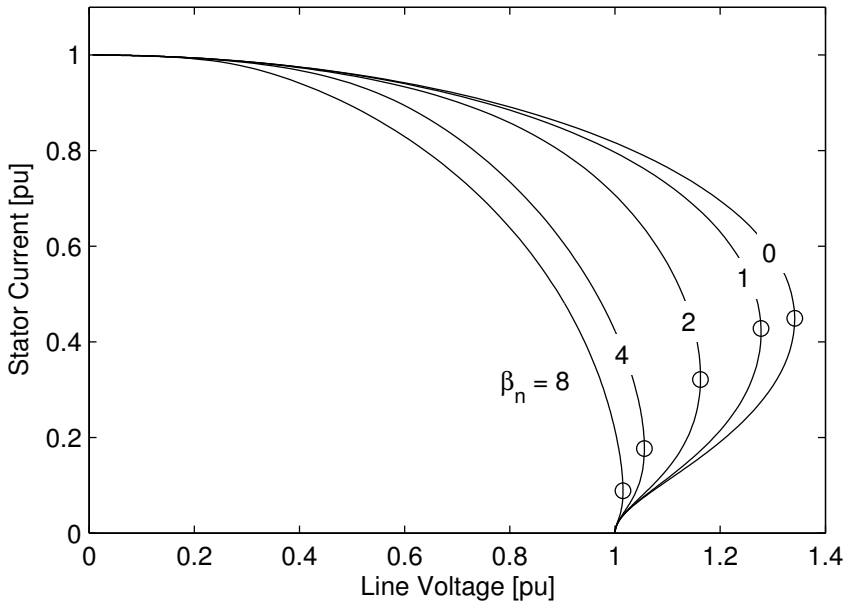

Figure 2.17: *Normalised voltage-current loci for various values of saturation parameter β_n, with $R_n = 0$ and $\xi = 6$*

that it was possible for an interior PM machine operating in uncontrolled generation to continue generating current into the DC link even below the threshold speed at which generation starts, i.e. the speed at which the rectified machine back-emf is equal to the DC link voltage. This counter-intuitive behaviour is illustrated in a plot of stator current vs. speed (see Fig. 2.18).

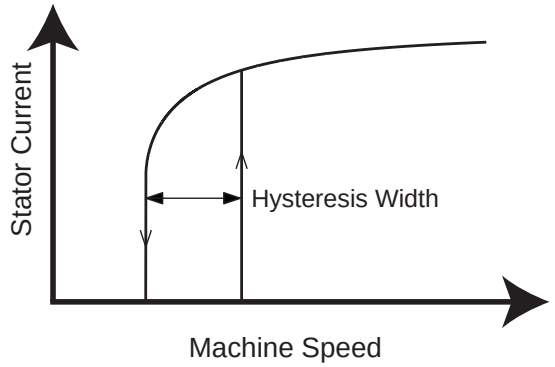

Figure 2.18: *Typical stator current vs. speed characteristic of an interior PM machine exhibiting hysteresis*

Jahns found that hysteresis was only present for saliency ratios of greater than 2 and

that the width of the hysteresis band was proportional to saliency and was reduced by magnetic saturation.

In this section, VI loci will be used to explain how a hysteretic curve arises in the stator current vs. speed characteristic of an interior PM machine. The VI locus is a simple graphical representation of the current-voltage characteristics of the interior PM machine with a resistive load and allows the correlation between hysteresis, voltage overshoot and the saliency ratio to be clearly illustrated.

2.4.1 Hysteresis explained using VI Loci

Figure 2.19 shows how the voltage overshoot in the VI locus of the interior PM machine causes hysteresis in the UCG stator current.

Consider a highly salient interior PM machine which exhibits voltage overshoot being connected via a three-phase uncontrolled rectifier to a DC voltage source and then accelerated from standstill.

The graph on the left shows the VI locus of the machine at increasing speeds from ω_1 to ω_4. The graph on the right shows the stator current which the machine generates as the speed is increased.

As the machine accelerates from standstill, it will only start to generate current into the DC link at a certain minimum speed - this is the speed at which the open-circuit back-emf exceeds the DC link voltage (referred to the AC side). The DC link voltage is represented on the graph as a vertical line. The possible operating points of this system are found where the VI locus of the machine and the DC link voltage intersect. These points are labelled on the VI loci and likewise the corresponding stator currents produced are labelled on the right-hand graph. At a low speed ω_1, for instance, the back-emf is lower than the DC link voltage and the diodes of the rectifier are reverse-biased. The system operates at (A) and the output current is zero. The output voltage is the machine open-circuit back-emf.

Generation only occurs at the higher speed of ω_3, where the machine open-circuit voltage becomes greater than the DC link voltage. The diodes become forward-biased and current starts to flow (B). Note that the machine VI locus intersects the DC link line at two points - at (B) where there is zero current and at (C) where there is non-zero current. Operating point (B) is unstable, as once current starts to flow the system immediately shifts up along the VI locus to operate at (C).

As the speed increases to ω_4, the operating point moves to (D), producing slightly

more current. If the speed is then decreased below ω_4, the current only ceases once the VI locus no longer intersects the DC link voltage line. Thus current still flows when the speed is decreased below ω_3, as the operating point is shifted along the overshoot portion of the locus, where the back-emf still exceeds the DC link voltage. The threshold occurs at ω_2, where the peak back-emf on the VI locus (E) is equal to the DC link voltage and decreasing the speed below this point causes the current to fall to zero. Note that although (E) is a valid operating point, generation does not start occuring at ω_2 because a non-zero current is necessary to obtain the voltage at (E).

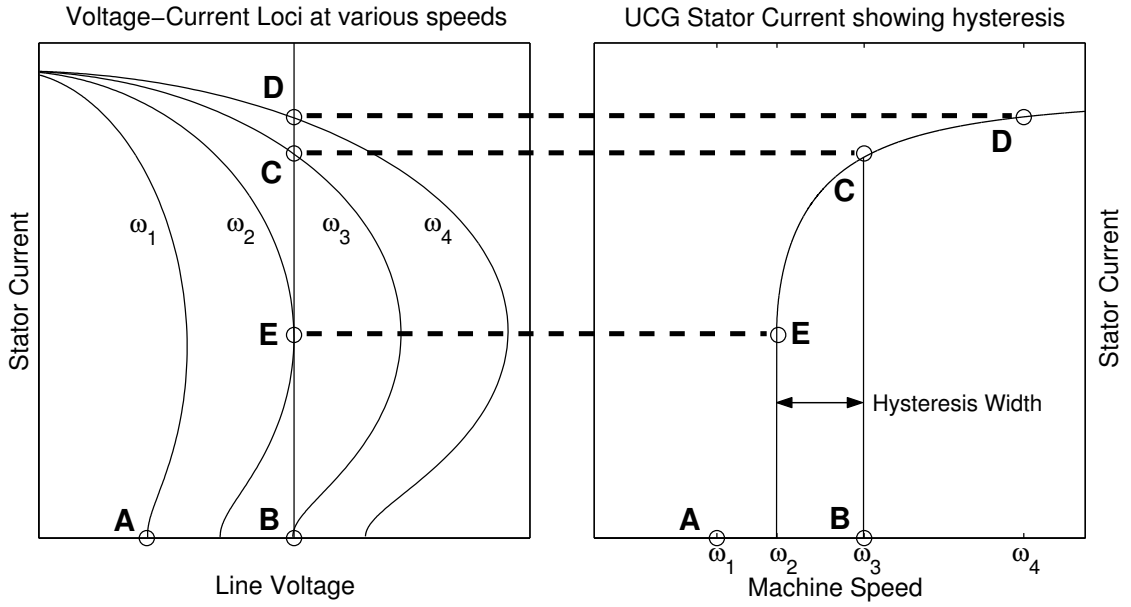

Figure 2.19: *The relationship between the VI loci and the stator current vs. speed characteristic of an interior PM machine exhibiting hysteresis*

It can be seen that hysteresis in the stator current versus speed characteristic arises through voltage overshoot in the VI locus and that the width of the hysteresis band is proportional to the amount of voltage overshoot. The factors which affect the presence of hysteresis in a machine under a particular operating condition are thus those same factors affecting voltage overshoot as described in the previous section, i.e. saliency ratio, magnetic saturation and stator resistance.

In addition, the DC link voltage into which the machine is operating is also a factor, as this is related to the machine speed at which generation occurs. Figure 2.15 showed that for machines with finite stator resistance, overshoot is only present above certain machine speeds. This same characteristic is represented in Fig. 2.20 in terms of DC link

voltage, which is proportional to the speed at which conduction first occurs, where a DC link voltage of 1 pu represents the rectified value of the machine back-emf at rated speed.

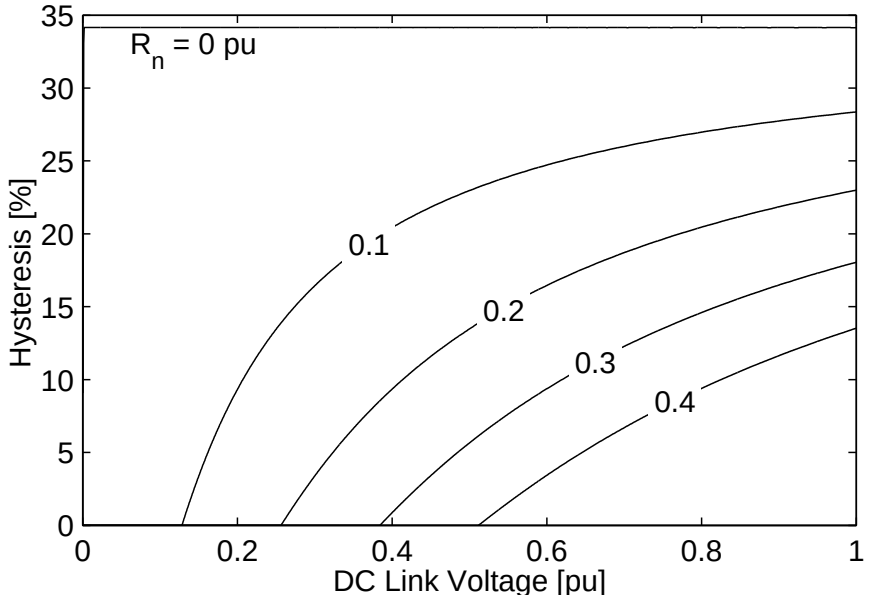

Figure 2.20: *Hysteresis versus DC link voltage for various values of R_n, with $\xi = 6$*

2.5 Experimental Investigation

In this section, experimental results from two interior permanent magnet machines are examined in order to investigate their behaviour under UCG operation. The tests described in the following subsections were carried out in order to achieve the following objectives:

- To test the validity of the steady-state and dynamic models used during the study and their accuracy in predicting the output of an interior PM machine operating in UCG;
- To experimentally demonstrate hysteresis in UCG, which had previously been predicted but not demonstrated;
- To test the validity of the approximations and assumptions made in the present as well as earlier models of UCG operation, specifically the approximation of a rectifier and voltage source load as a three-phase resistive load.

2.5.1 Test Machine Parameters and Construction

The 6.8 kW alternator used in this study was an interior PM machine built as a concept demonstrator in a previous investigation [16]. The custom-made interior PM rotor was comprised of radial multiple-barrier laminations embedded with rare-earth Neodymium-Ferrite-Boron (NdFeB) magnets (see Figs. 2.21 and 2.22). As a comparison in some tests, a 2.0 kW axially-laminated rotor using flexible ferrite magnets was also used. Both rotors were run with a standard 4 pole induction motor stator rated for 2.2 kW at 415 V, 4.8 A [39].

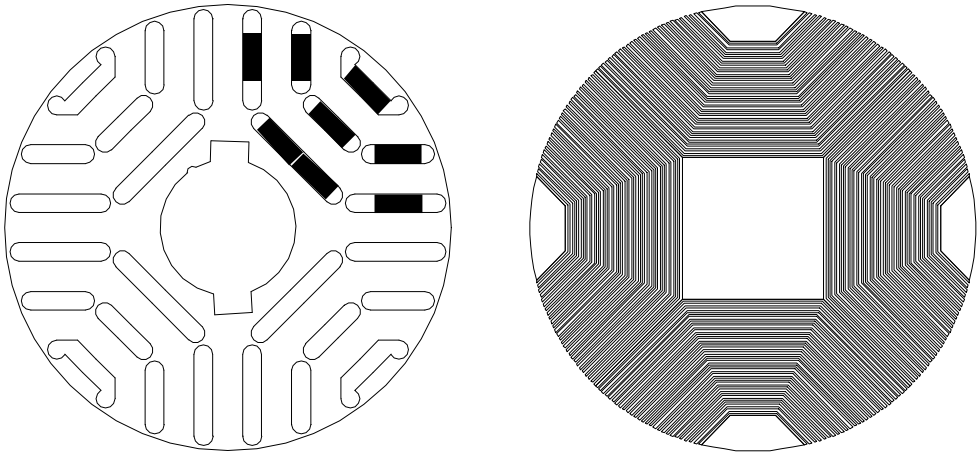

Figure 2.21: *Rotor cross-sections for the multiple-barrier and axially-laminated machines*

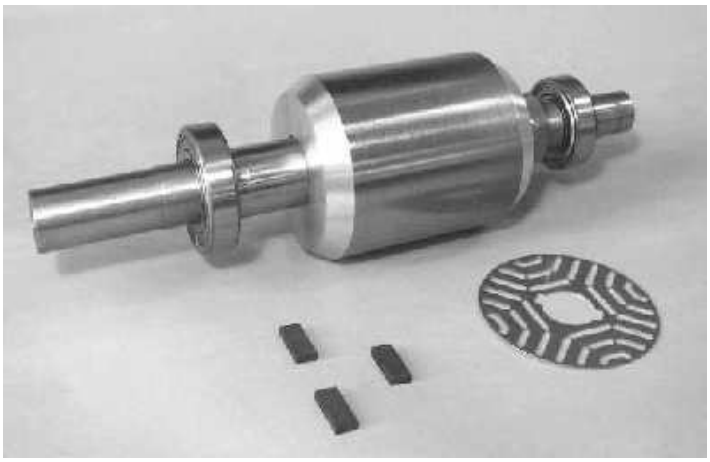

Figure 2.22: *Multiple-barrier rotor with rare-earth magnets*

The multiple-barrier rotor was designed by Soong and Ertugrul [16] to achieve a wide constant-power speed range. This is done by selecting the rated current to be equal to the characteristic current as described by (2.18), producing a design which has close to optimal field weakening operation.

The measured electrical parameters of the two machines are shown in table 2.1. The pertinent characteristics of the rotors are their high saliency and high back-emf. The axially-laminated rotor has a higher unsaturated saliency ratio ($\xi = 7.67$) than the multiple-barrier rotor ($\xi = 5.87$).

$$\Psi_m = L_d I_d \tag{2.18}$$

Figure 2.23 shows the measured curves of machine inductance versus stator phase current. Heavy magnetic saturation is exhibited in the q-axis, where the saturated inductance at the rated stator current of 9.4 A is roughly a third of its unsaturated value.

Table 2.1: *Measured test machines parameters*

Parameter	**Multiple-barrier**	**Axially-laminated**
q-axis inductance (unsat'd)	312 mH	345 mH
d-axis inductance (sat'd)	53 mH	45 mH
max. saliency ratio	5.87	7.67
stator phase resistance	3.0 Ω	3.0 Ω
magnetic flux-linkage (Vs peak)	0.704 Vs	0.1802 Vs
open-circuit line-to-line back-emf @ 1,500 rpm (Vrms)	271.2 V	69.3 V
short-circuit current @ 1,500 rpm	9.4 A	2.8 A
max. power under UCG operation	6.8 kW	2.0 kW

2.5.2 Experimental Setup

The dynamometer test rig in Fig. 2.24 was used to drive the electrical machines used in this study. This consisted of two 5 kW DC machines with a rated speed of 1,500 rpm, connected to the test machine via a belt drive (see Fig. 2.25) with adjustable gear ratio settings of 4:1, 2:1 and 1:1, thus allowing a maximum test speed of 6,000 rpm. The speed was controlled by varying the armature voltage to the DC machines. The windings of the test machine could be connected to various types of loads as necessary for each test, e.g.

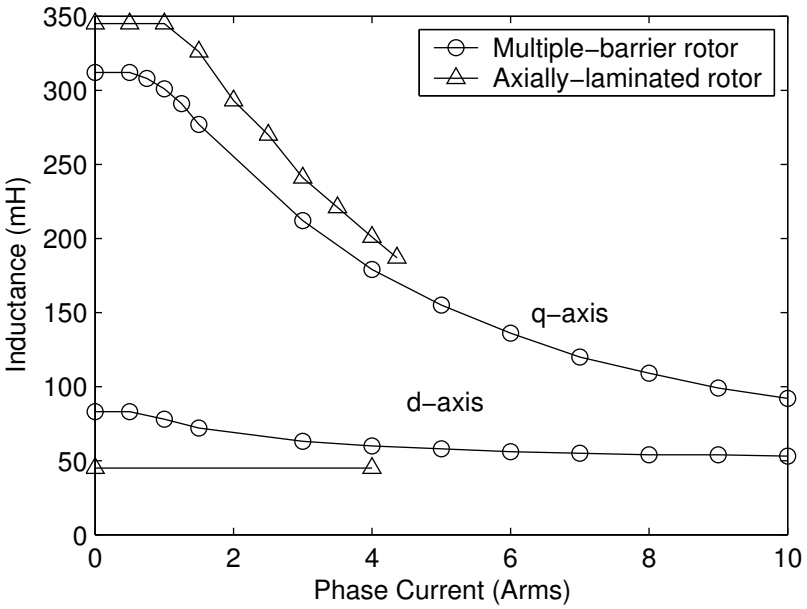

Figure 2.23: *Measured d-axis and q-axis inductance saturation curves for the multiple-barrier and axially-laminated machines*

a three-phase resistive load, a rectifier and resistive load or a rectifier and voltage source load.

The DC voltage source load simulator depicted in Fig. 2.24 employed a series diode to prevent damage to the laboratory power supply and a parallel resistive load in order to absorb the power generated by the test machine. The value of this load resistance was chosen to be able to absorb the maximum expected load current.

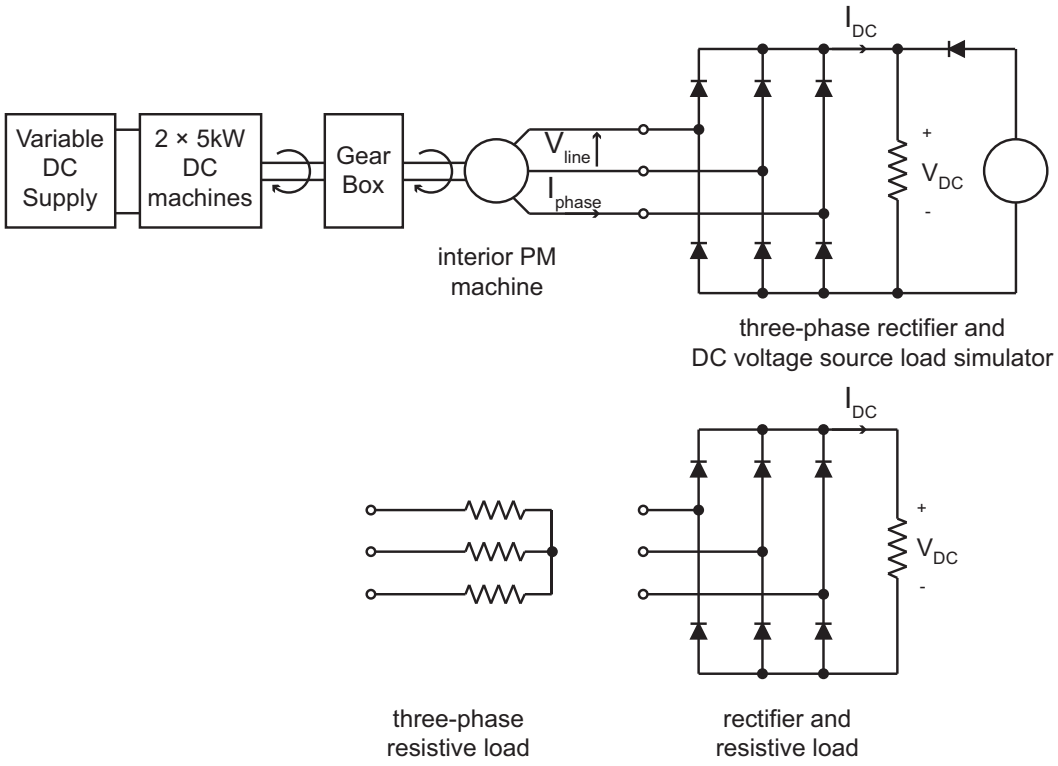

Figure 2.24: *Dynamometer rig test setup for testing the interior PM alternator*

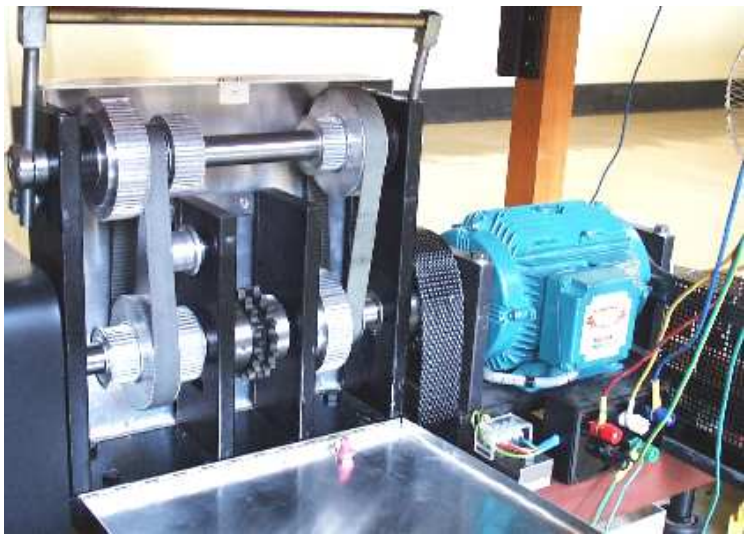

Figure 2.25: *Variable gearbox for the dynamometer rig*

The DC machine's armature voltage and current, field current and speed were monitored on a readout box during the tests. A bank of meters provided measurements of the three-phase test machine's line voltages, phase currents and output power, while a load cell on the stator of the test machine measured its reaction torque.

2.5.3 Short-Circuit Test

As a simple initial validation of the steady-state model, measurements of short-circuit current and torque vs. speed were conducted. When the test machines are driven from standstill with their windings short-circuited, the stator current rises monotonically with speed and asymptotes towards a value of Ψ_m/L_d. The torque initially increases, reaches a maximum value at low speed, then gradually decreases with increasing speed.

The calculated curves were obtained from the steady-state model using a zero load resistance. A good match with the experimental data was obtained for the multiple-barrier machine (see Fig. 2.26), however the measured torque results for the axially-laminated machine were slightly larger than the predicted values (see Fig. 2.27). This could be due to the typically higher iron losses in axially-laminated machines or the effect of the iron losses simply being more noticeable due to the lower torque magnitude.

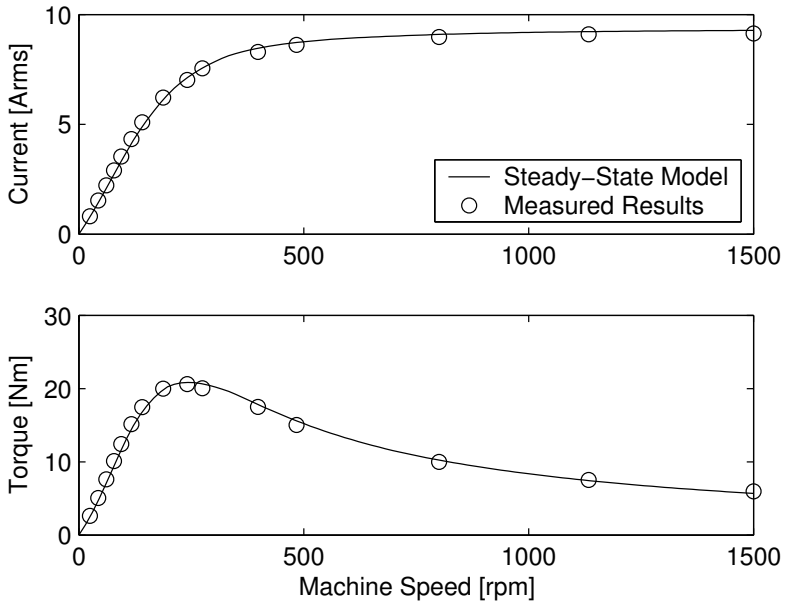

Figure 2.26: *Short-circuit phase current and torque vs. speed for the multiple-barrier machine*

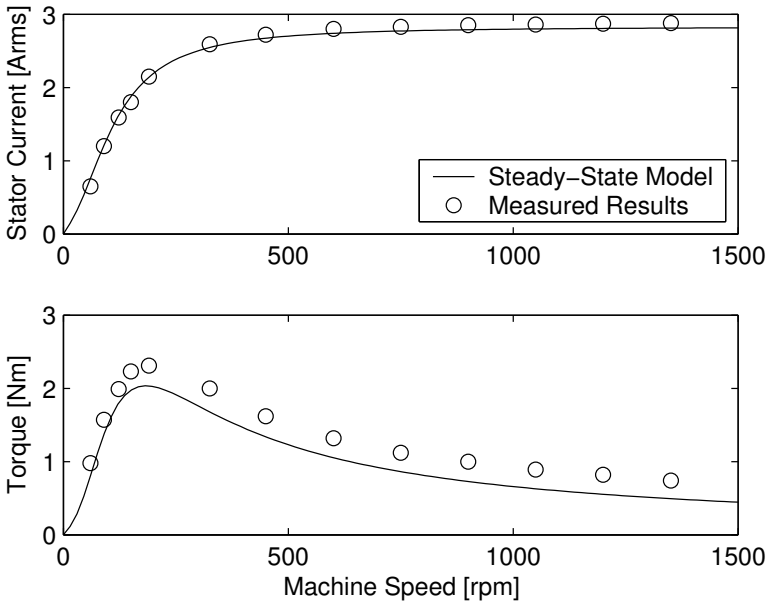

Figure 2.27: *Short-circuit phase current and torque vs. speed for the axially-laminated machine*

2.5.4 Three-Phase Resistive Load Test

A three-phase resistive load is the load upon which the steady-state model of UCG is directly based and also the simplest load to analyse. Hence, the results are most likely to match the model predictions.

The test machines were run at 1,500 rpm into a three-phase resistive load and the stator currents and line voltages were measured for various values of load resistance in order to obtain VI loci. Figure 2.28 shows the measured and predicted results for the multiple-barrier machine. The ideal model prediction shown does not take into account stator resistance or magnetic saturation and exhibits approximately 30% voltage overshoot. The effect of stator resistance alone reduces the predicted overshoot from 30% to 22%, whereas the effect of magnetic saturation alone reduces the predicted overshoot from 30% to 14%, hence playing a larger part in reducing the overshoot than stator resistance for this machine at this speed. The combination of these two effects act to reduce the predicted overshoot from 30% to a mere 7%.

For the axially-laminated machine, the maximum q-axis current obtainable at 1,500 rpm regardless of the value of load resistance is approximately 0.5 A. Referring to Fig. 2.23, this current is still in the unsaturated region of L_q so the machine does not experience magnetic saturation, which can therefore be neglected. Although the decrease in current due to stator resistance is much more noticeable than in the multiple-barrier machine, the reduction of the predicted overshoot from 56% of the open-circuit voltage to 50% is less dramatic (see Fig. 2.29).

The measured VI loci from both interior PM machines are closely matched by the steady-state model predictions, indicating that the model is reasonably accurate.

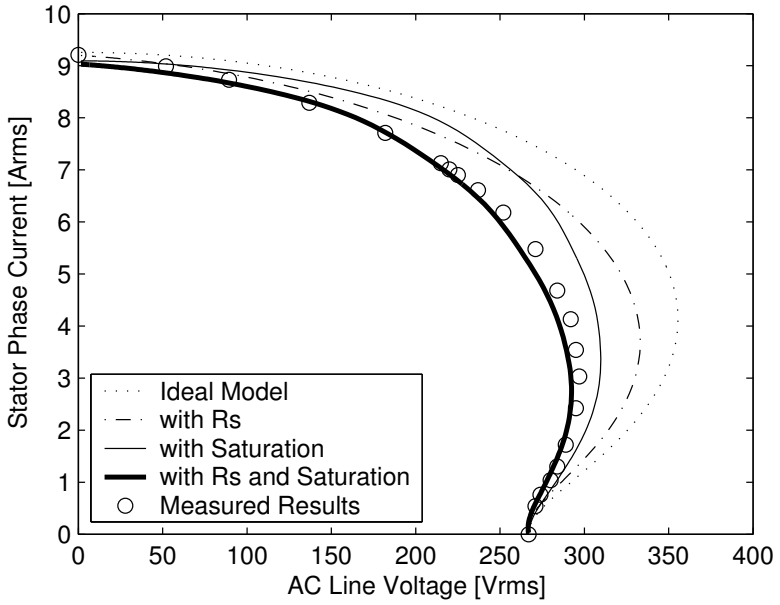

Figure 2.28: *Voltage-current loci for the multiple-barrier machine, operating at 1,500 rpm with a three-phase resistive load, showing the effect of non-idealities*

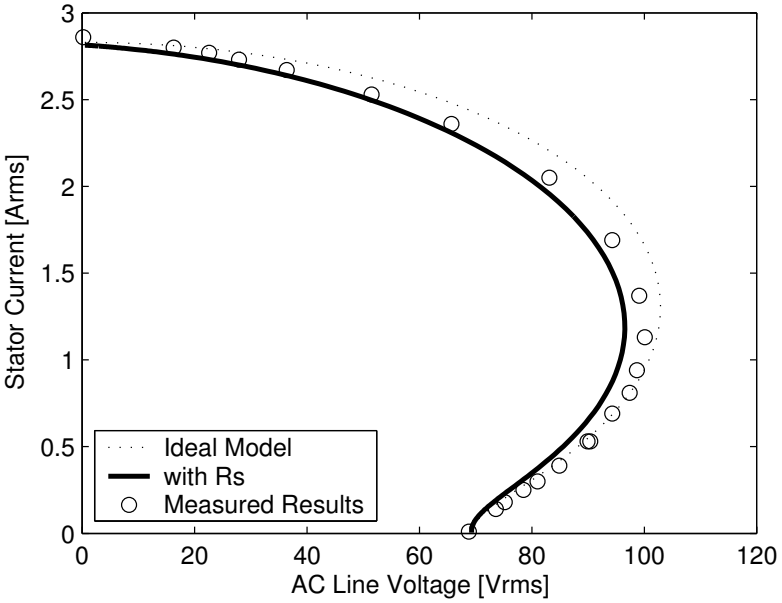

Figure 2.29: *Voltage-current loci for the axially-laminated machine, operating at 1,500 rpm with a three-phase resistive load, showing the effect of non-idealities*

2.5.5 Generation into a Rectifier and Resistive Load

In this test, both machines were run at speeds of 1,800, 3,000 and 6,000 rpm into a three-phase rectifier and resistive load (see Fig. 2.5b) and current, voltage and power measurements were taken. AC measurements were taken at the machine windings and DC measurements were taken across the resistive load. These measurements allow an observation of how the AC VI loci translate to DC output, which reflects on the validity of simplifying a rectifier and resistive load as a three-phase resistive load in the steady-state model of UCG.

The theoretical loci at the output of the rectifier were obtained by scaling the the AC predictions by the theoretical ratio of the rectified DC to rms AC values. These ratios are 1.355 for current and 1.283 for voltage.

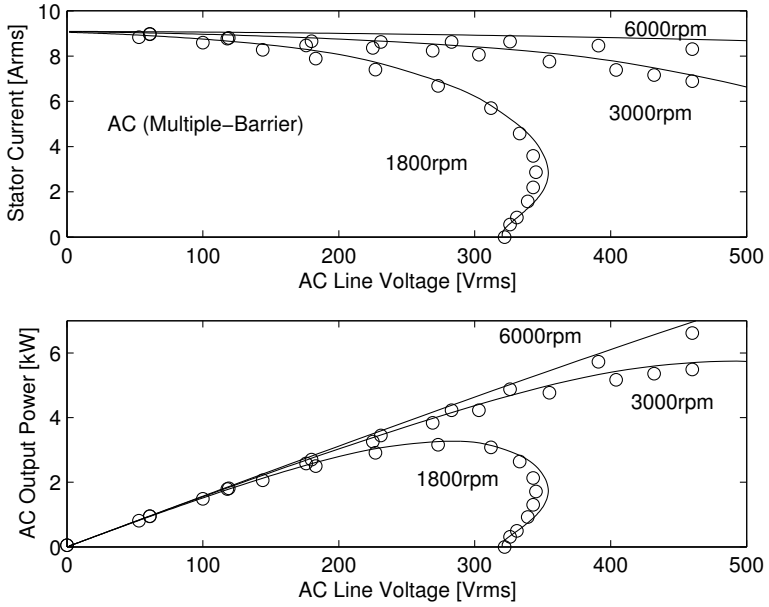

Figure 2.30: *AC VI and VP loci for the multiple-barrier machine at various speeds, showing calculated curves (lines) and measured results (circles)*

Figure 2.30 shows the measured voltage-current and voltage-power loci together with the steady-state model predictions for the multiple-barrier machine. The AC results match well with the predictions although the current obtained is slightly smaller than predicted. There is however a significant discrepancy in the corresponding DC output curves (see Fig. 2.31) at lower values of current corresponding to the voltage overshoot region. The measured overshoot for the multiple-barrier machine at 1500 rpm is thus reduced tenfold, from 10% in the AC curves to about 1% in the DC curves.

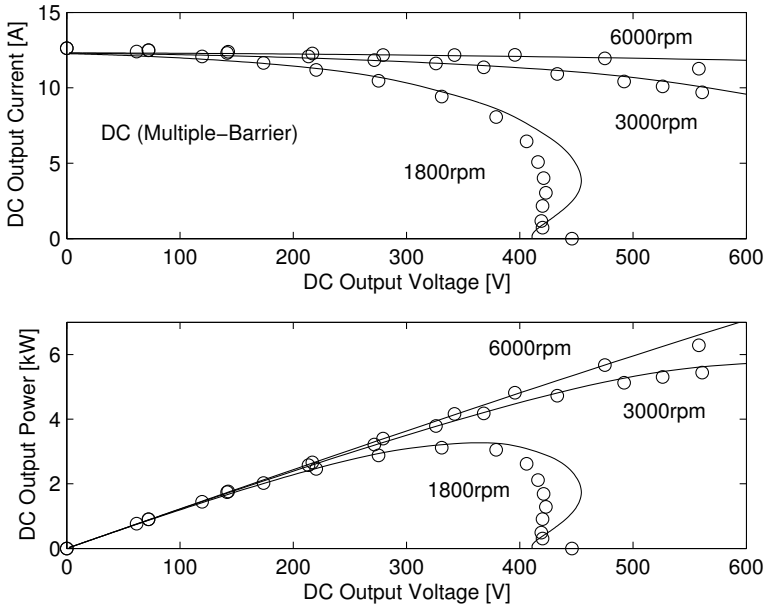

Figure 2.31: *DC VI and VP loci for the multiple-barrier machine at various speeds, showing calculated curves (lines) and measured results (circles)*

The multiple-barrier machine results show that at higher speeds the stator current becomes nearly constant with respect to line voltage and the output power is almost linearly related to output voltage. They also show that at rated line voltage (415 V) the machine is capable of producing around 6 kW of output power at 6,000 rpm.

The results for the axially-laminated machine (see Figs. 2.32 and 2.33) exhibit the same trends as those found with the multiple-barrier machine. The measured AC curves show a good correspondence with the steady-state model predictions, whereas once again significant discrepancy is noted in the DC curves, which show a lower than predicted maximum voltage on the overshoot portion of the loci.

One feature which occurs in both the multiple-barrier machine and the axially-laminated machine is the unusual shape of the measured DC curve towards lower currents - the open-circuit voltage appears higher than predicted and as the current increases from zero, the voltage at first decreases before starting to rise as the operating point enters the voltage overshoot region.

The decreased maximum overshoot voltage in the axially-laminated machine means that it will stop generating at a higher speed than predicted, causing a reduction of overshoot in the DC loci from 39% to 23%, which corresponds to a reduction factor of 1.7 which is consistent for both the 750 rpm and 1,500 rpm curves. As this significant voltage

overshoot reduction in both machines was not observed in the AC side loci, it may be due to the discontinuous current waveforms present in this region.

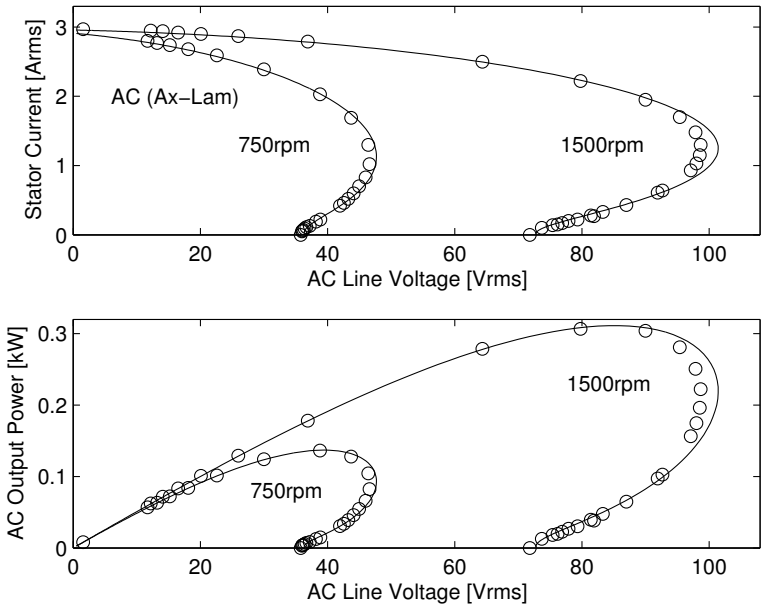

Figure 2.32: *AC VI and VP loci for the axially-laminated machine at various speeds, showing calculated curves (lines) and measured results (circles)*

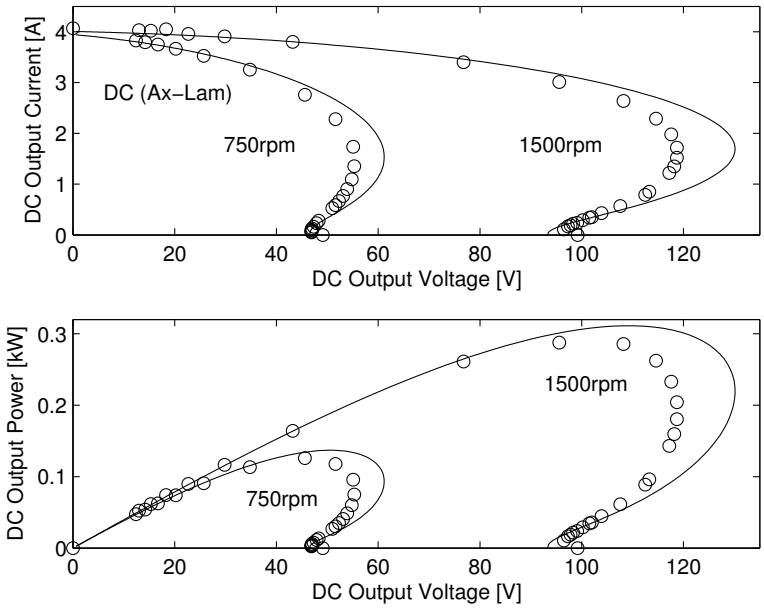

Figure 2.33: *DC VI and VP loci for the axially-laminated machine at various speeds, showing calculated curves (lines) and measured results (circles)*

2.5.6 Generation into a Rectifier and Voltage Source Load

For testing of actual uncontrolled generation, the output of the test machine was connected to a rectifier and a variable DC voltage supply as shown in Fig. 2.24. The DC voltage supply was capable of providing sufficiently high DC link voltages of up to 200 V DC, such that hysteresis should be observable within the speed range from 0 to 1,500 rpm. The steady-state model predictions of voltage versus speed for both test machines (see Fig. 2.34), with dotted lines indicating the predicted minimum DC link voltage and machine speed at which hysteresis occurs.

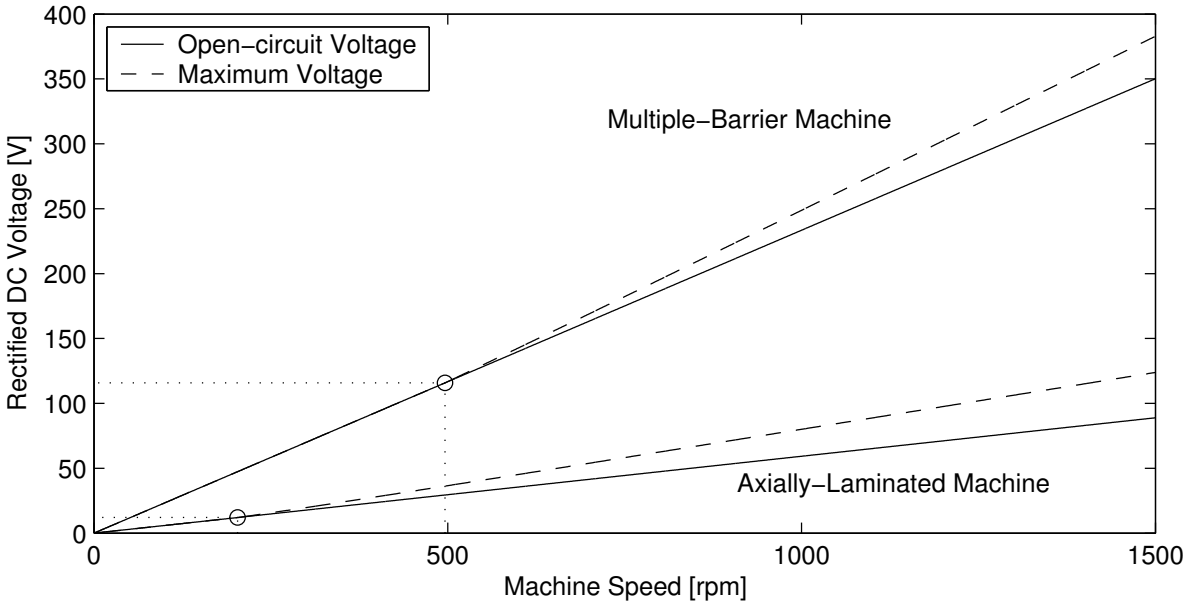

Figure 2.34: *Predicted rectified open-circuit and maximum voltage vs. machine speed*

The corresponding hysteresis vs. DC link voltage predictions (see Fig. 2.35 and 2.36) were generated from the dynamic model and from the steady-state model both with and without stator resistance. Note that the prediction from the ideal steady-state model neglecting resistance appears as a straight line at 16% for the multiple barrier-machine and 48% for the axially-laminated machine as without resistance the percentage overshoot does not change with speed.

The steady-state model including resistance predicts that no hysteresis will be obtained below threshold DC link voltages of 115 V for the multiple-barrier machine and 11 V for the axially-laminated machine. At DC link voltages above these thresholds, a reduced hysteresis band should be obtained, with the width of the band asymptoti-

cally approaching the ideal hysteresis width value as the DC link voltage increases. The dynamic model prediction (which includes resistance) lies roughly mid-way between the steady-state model predictions with and without resistance.

The actual hysteresis measured for the axially-laminated machine is significantly smaller than that predicted by the steady-state model. If the overshoot reduction factor of 1.7 observed earlier in the measured VI loci is incorporated into the steady-state prediction, it can be seen that the measured points are more consistent with the resultant adjusted curve. Experimental points were only taken up to a DC link voltage of 80 V, due to the axially-laminated machine's maximum test speed of 1,500 rpm.

Figure 2.36 shows that the hysteresis predictions of the steady-state model with resistance and the dynamic model predictions were comparable for the multiple-barrier machine. No hysteresis was observed experimentally with the multiple-barrier machine, even with measurements being taken up to 250 V. Taking into account the tenfold decrease previously observed in the measured voltage overshoot between the AC and DC curves, the expected hysteresis is only approximately 1%. This corresponds to a speed range of 15 rpm at this test speed, which may have been too small to detect with the experimental setup used.

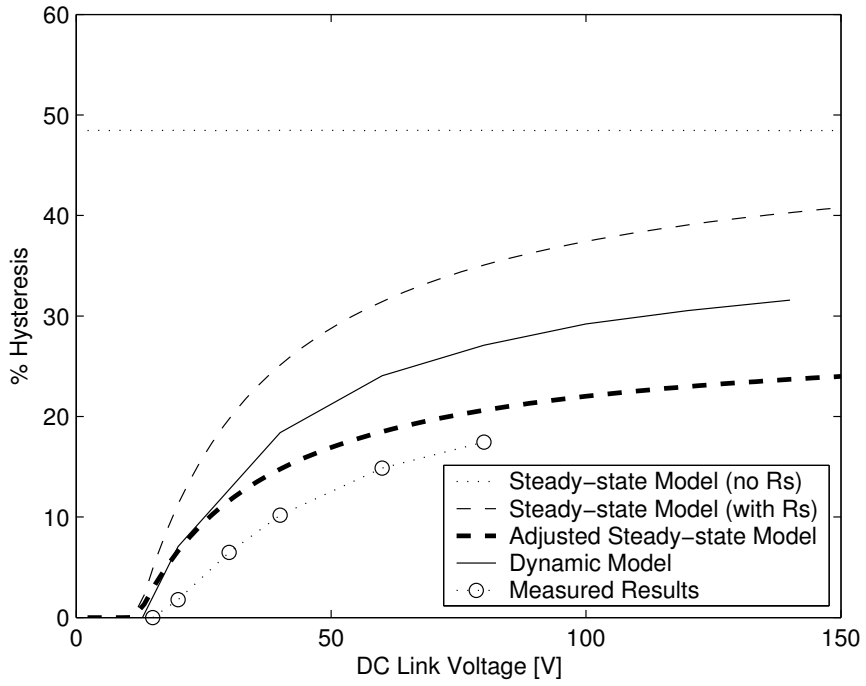

Figure 2.35: *Model predictions and measured hysteresis band as a function of the DC link voltage for the axially-laminated machine*

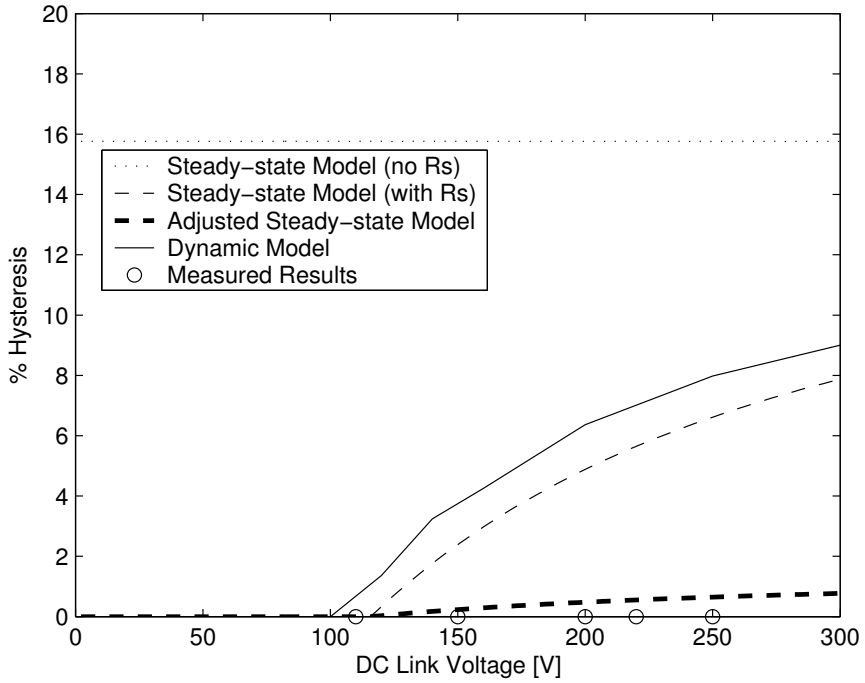

Figure 2.36: *Model predictions and measured hysteresis band as a function of the DC link voltage for the multiple-barrier machine*

Figures 2.37 and 2.38 show examples of measured stator current versus speed characteristics from which the hysteresis data points in Figures 2.36 and 2.35 were obtained, for the multiple-barrier rotor and the axially-laminated rotor respectively.

The stator current was recorded as the machine speed was increased slowly from standstill up to 1,500 rpm and then decreased until generation ceased. Figure 2.38 shows the axially-laminated machine operating into a DC link voltage of 40 V. The upper half of the figure shows calculated VI loci for the machine at increasing speeds, with the DC link voltage (referred to the machine AC side) indicated as a solid vertical line. The lower half shows a plot of measured stator current versus speed, overlaid with calculated curves from the dynamic model and from the steady-state models both with and without resistance. The axially-laminated machine exhibited a measured hysteresis band of approximately 15%, which is significantly smaller than the steady-state prediction of 25%, but close to the dynamic model prediction of 18%.

Figure 2.37 shows the multiple-barrier machine operating into a DC link voltage of 110 V, where no hysteresis was observed. The reason for this is evident in the VI loci which indicate that generation begins at around 480 rpm, where the open-circuit back-emf crosses the DC link voltage line. At this speed there is almost no overshoot in the VI

locus and hence no observable hysteresis.

While all three models could accurately predict the speed at which generation starts, it can be seen that the steady-state model prediction incorporating resistance generally shows the best match with the measured results, particularly at higher speeds. In comparison, the dynamic model tends to slightly overestimate the current throughout the curve but provides a more accurate prediction of the speeds at which generation begins and ends. This can be more clearly seen in Fig. 2.32, which shows an enlarged view of the speed range over which hysteresis occurs. The steady-state model neglecting resistance overestimates both the stator current magnitude and the hysteresis considerably, as shown in the case of the 110 V DC link voltage where it incorrectly predicts the presence of hysteresis where there is none (see Fig. 2.36).

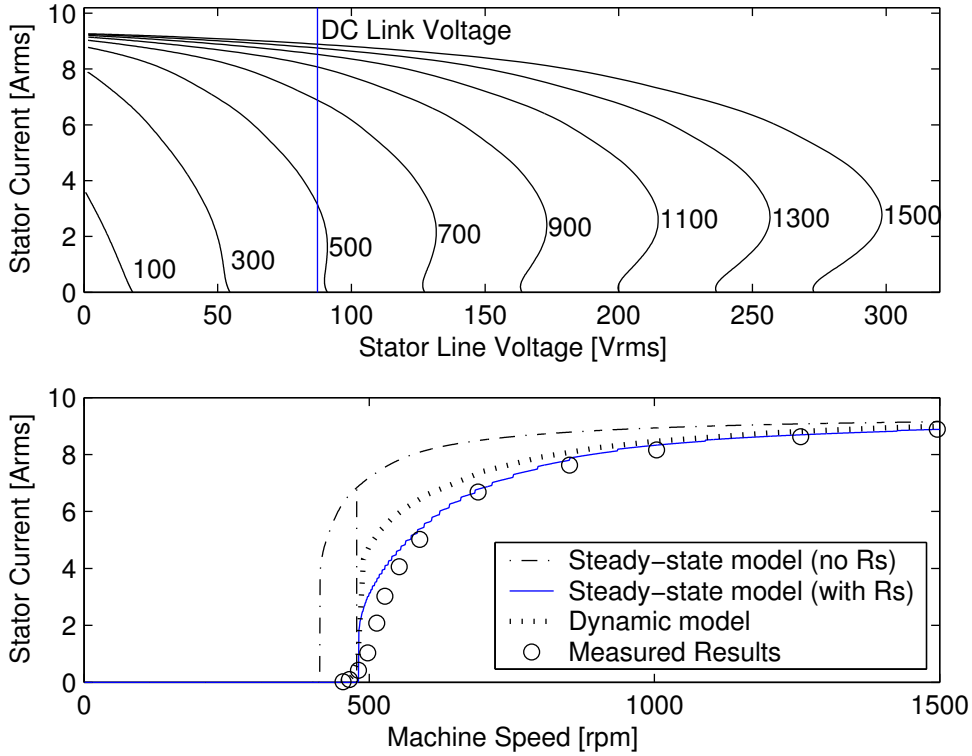

Figure 2.37: *Calculated and measured UCG stator current characteristic with speed for the multiple-barrier machine operating into a 110V DC voltage source*

Several oscilloscope screenshots of the stator current and voltage waveforms are shown in Fig. 2.40, taken from the multiple-barrier machine operating into a rectifier and voltage source load of 110 V. At rated speed (1,500 rpm) where the back-emf voltage is much higher than the DC link voltage, the stator current is sinusoidal while the stator line

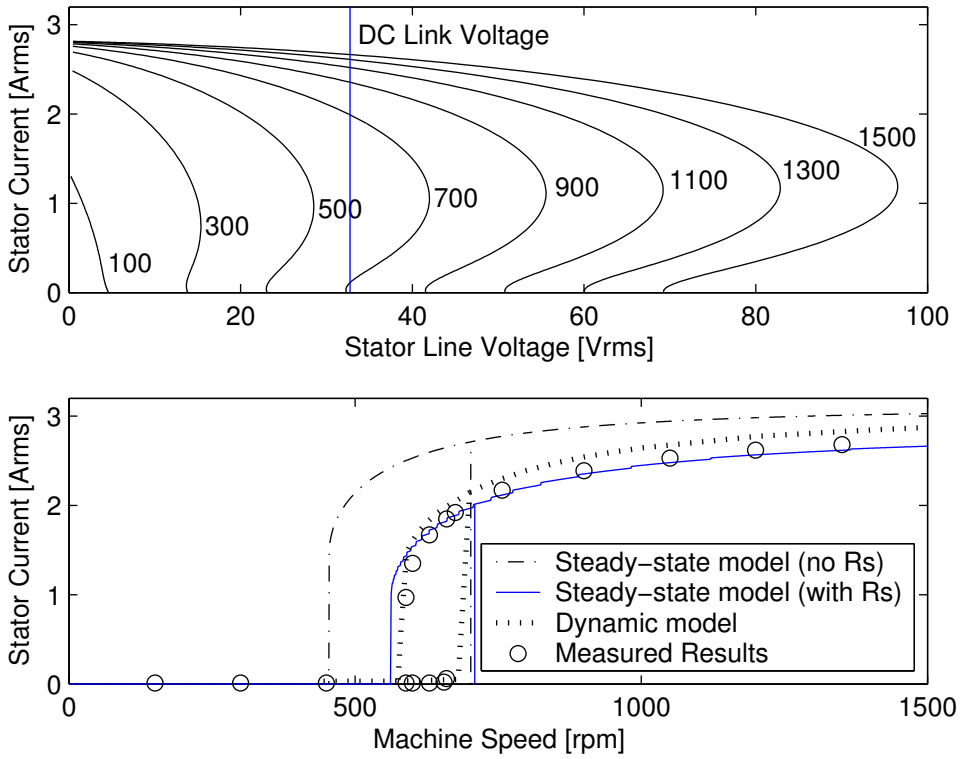

Figure 2.38: *Calculated and measured UCG stator current characteristic with speed for the axially-laminated machine operating into a 40V DC voltage source*

voltage resembles the normal six-step waveform from an inverter, ranging from 110 V to -110 V.

As the speed is reduced to 504 rpm, the machine back-emf becomes comparable to the DC link voltage, the current waveform becomes non-sinusoidal and the line voltage waveform transitions start to become smoother (note the change in the scaling of the current axis). This trend continues down to a low speed close to the generation threshold (482 rpm), where the current starts to resemble a six-step waveform and the voltage is more sinusoidal.

The waveform shapes are accurately predicted by the dynamic model, although there is some discrepancy in the magnitude of the current at 504 rpm.

2.6 Summary of Findings

The work in this chapter has produced findings which represent new contributions in the area of interior PM machines, which can be used as a high power alternator in vehicles:

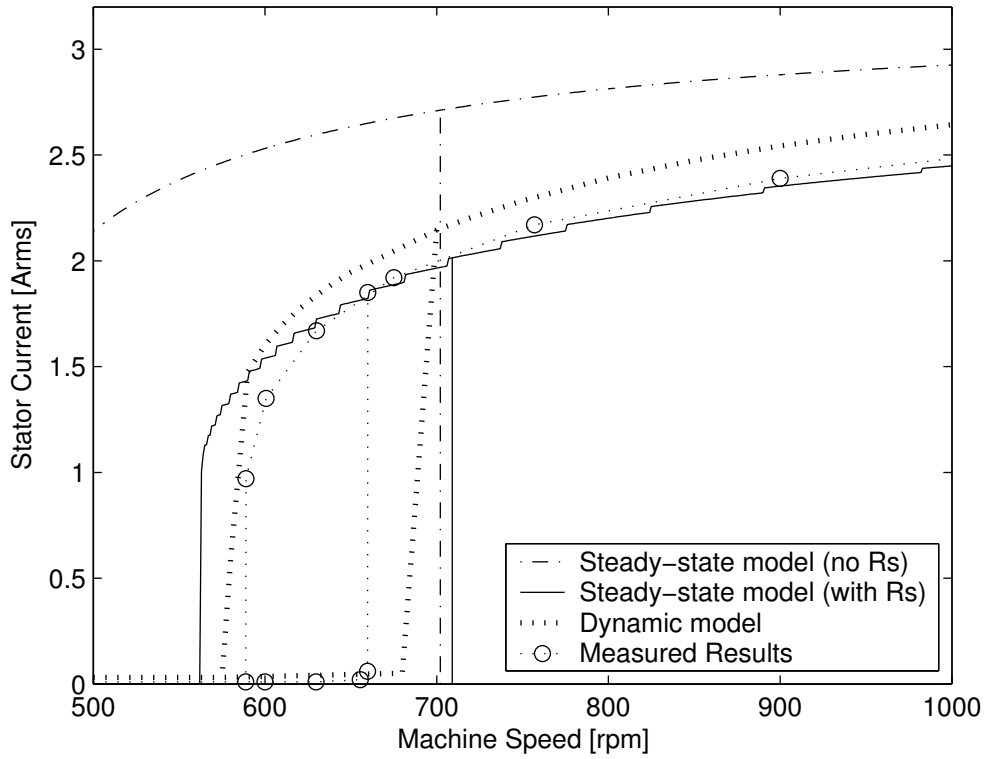

Figure 2.39: *Enlarged view of the hysteresis band shown in Fig. 2.32*

- The output voltage versus current locus with a resistive load of an interior PM machine with a saliency ratio of greater than 2 may exhibit a voltage overshoot effect where the output voltage under load is greater than the open-circuit voltage.

- This voltage overshoot is responsible for hysteresis in the UCG stator current versus speed characteristic and the width of the hysteresis band is proportional to the voltage overshoot.

- The magnitude of the voltage overshoot is proportional to the machine saliency and is therefore also affected by magnetic saturation, which causes an effective non-linear reduction in the saturated saliency ratio.

- Neglecting stator resistance, the width of the hysteresis band is independent of speed. The presence of stator resistance reduces the voltage overshoot obtained. Practically, this means that for a given machine, overshoot and thus hysteresis only occurs above a certain speed which is dependent on the relative magnitude of the stator resistance with respect to the machine reactances. This threshold speed can

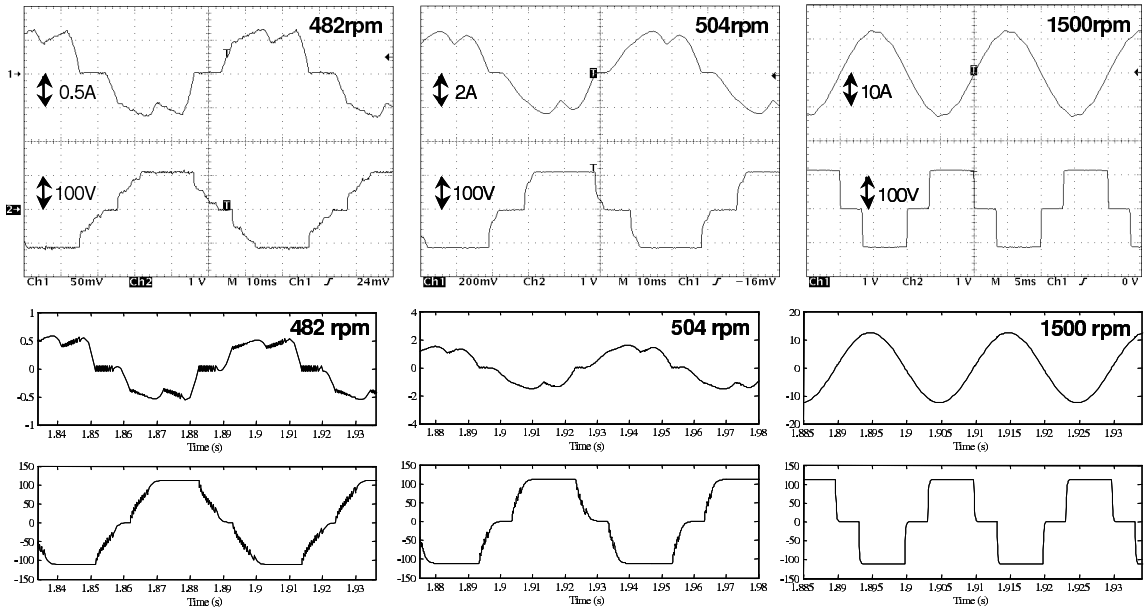

Figure 2.40: *Measured (top) vs. simulated (bottom) stator current and voltage waveforms in UCG for the multiple-barrier machine at speeds corresponding to the start of conduction (482 rpm), at a low speed after the conduction point (504 rpm) and at high speed (1500 rpm)*

also be thought of as corresponding to a DC link voltage below which no hysteresis is observed.

Evaluation of equivalent circuit models of uncontrolled generation:

- The VI loci experimentally measured from a rectifier and resistive load could be used to accurately predict the stator current versus speed characteristic measured with a rectifier and DC voltage source load, therefore the modelling of a DC voltage source load as a resistive load can be considered valid.

- Several differences were found between the VI loci measured from a three-phase resistive load and those measured from a rectifier and resistive load. Specifically, the output voltages obtained in the overshoot portion of the VI loci were lower with a rectifier and resistive load than with a three-phase resistive load. Examination of the current and voltage waveforms in this operating region showed that the currents were highly discontinuous due to the action of the rectifier. As this goes against the steady-state model assumption of sinusoidal current waveforms, this may be a factor in the observed discrepancy.

- The simulation results were experimentally validated using two high-saliency interior PM machines. An extensive comparison of the simulation and test results were performed including short-circuit, three-phase resistive load, rectifier and resistive load, and rectifier and voltage source load.
- The predicted stator current hysteresis was demonstrated in one of the test machines.

Chapter 3

Switched-Mode Rectifier Control

In this chapter, the use of a switched-mode rectifier (SMR) at the output of the interior PM alternator is examined. The basic operating principles of an SMR and its application to power generation in the interior PM alternator are discussed and the steady-state and dynamic response of the alternator and SMR system to duty-cycle control are theoretically and experimentally investigated.

3.1 Introduction to Switched Mode Rectification

A switched-mode rectifier is a form of power converter which employs semiconductor switches switching at high frequency to convert an AC input to a DC output. While switched-mode rectifiers may exist in various configurations, they generally consist of rectifier diodes and one or more controlled switches. In this respect they can be considered an intermediate step between a passive rectifier and an inverter, as depicted in Fig. 3.1, reproduced from Chapter 1, which also shows circuit diagrams of two SMR variants - the single-switch SMR and the semi-bridge SMR.

The semi-bridge SMR offers more flexibility as compared to the single-switch SMR by having three switches which can be independently controlled by separate switching signals. However, if the same signal is used to control all three switches, the operation of the semi-bridge SMR is similar to that of a single-switch SMR. In this case, the semi-bridge SMR still has the advantage of one less diode voltage drop in delivering output power, at the cost of the two additional switches. If Field Effect Transistors (FETs) are being used as switching devices, however, it may still be necessary to use multiple devices in parallel to achieve the required current rating.

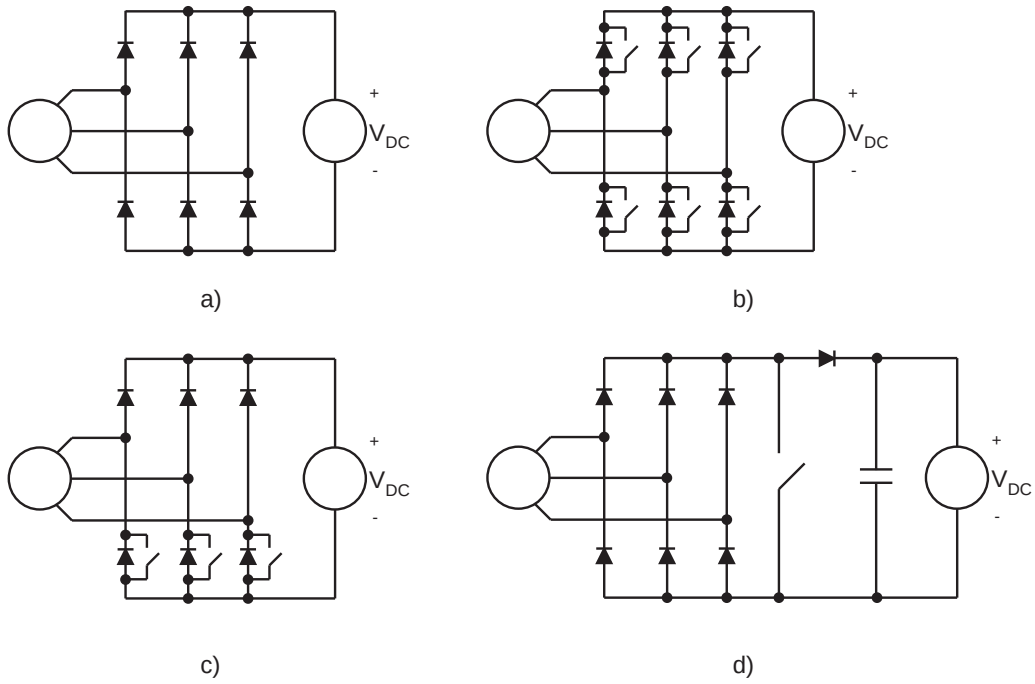

Figure 3.1: *Three-phase AC machines operating into a voltage source load via: a) a bridge rectifier, b) an inverter, c) a semi-bridge SMR, and d) a single-switch SMR*

The use of a switched-mode rectifier at the output of the interior PM alternator in this study was investigated as a means to accomplish two objectives - to maximise output power at any alternator speed when operating into a constant voltage source and to perform output voltage regulation, particularly to reduce output voltage transients under load dump conditions.

Both SMR configurations were used in this study - the semi-bridge rectifier is examined in Chapter 4 for the improvement of low speed output power, but for the purpose of investigating the basic characteristics of switched-mode rectifier operation, a single-switch SMR is considered. Similar work with a single-switch SMR was previously undertaken by Perreault, who investigated the load-matching performance of an SMR to maximise power transfer from a Lundell alternator [9]. This study demonstrated the ability of the SMR to improve alternator power output at high speeds, as well as to suppress voltage transients.

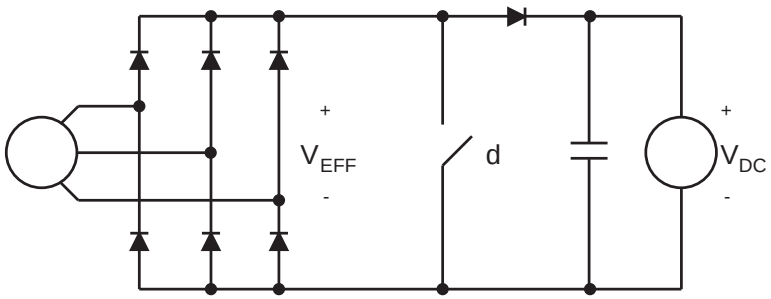

Figure 3.2: *Interior PM alternator operating with an SMR into a DC voltage source load*

3.2 SMR Operation

Figure 3.2 shows the interior PM alternator operating into a DC voltage source load with a single-switch SMR. A pulse width modulated (PWM) control signal is used to turn the SMR switch on and off at high frequency. With the switch turned on, the alternator windings are short-circuited and current increases in the machine windings. When the switch is off, the current flows through the diode into the DC link. With a sufficiently large alternator winding inductance, the machine sees only the time-averaged effect of the switching. This serves two purposes, depending on the operating speed of the alternator.

At low speeds where the rectified alternator back-emf is less than the DC link voltage, no generation will occur if the switch is off. However, during SMR switching, the buildup of current in the machine winding inductances while the switch is closed allows a portion of current to pass through to the DC link after the switch opens, even against the higher voltage. In this manner, the SMR acts similarly to a boost rectifier, effectively increasing the machine output voltage but reducing its effective output current. This effect can also be viewed as a reduction in the effective DC link voltage seen by the alternator (see Fig. 3.3). Thus, if a voltage V_{DC} is present at the DC link, applying a PWM control signal of duty-cycle d will lower the effective DC link voltage V_{EFF} seen by the alternator, according to (3.1).

$$V_{EFF} = (1 - d)V_{DC} \tag{3.1}$$

Note that although the effective DC link voltage decreases with increasing SMR duty-cycle, so does the proportion of current actually delivered to the DC link as shown in

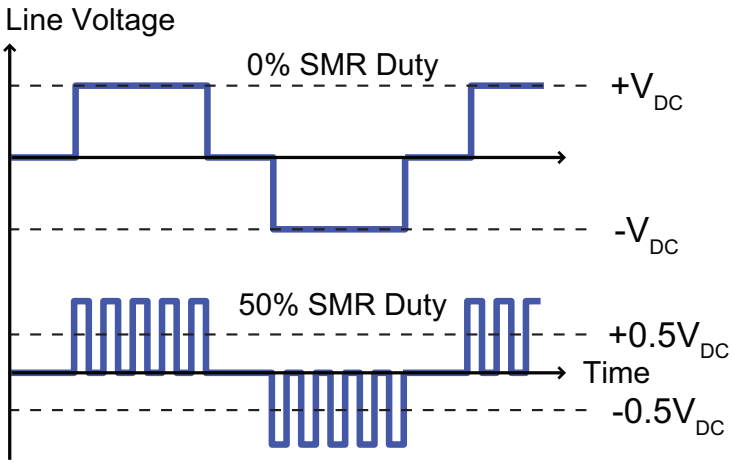

Figure 3.3: *The effect of switched-mode rectifier operation on the alternator stator line voltage waveform (solid lines) and effective DC link voltage seen by the alternator (dashed lines).*

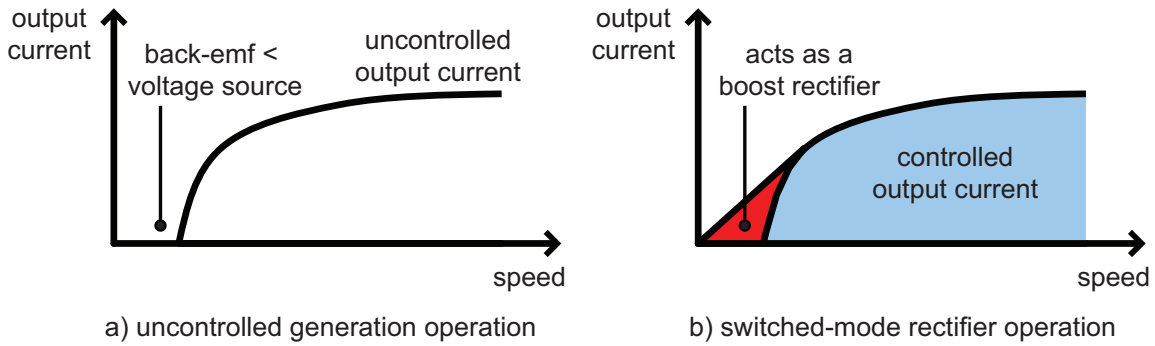

Figure 3.4: *Comparison of the operation of an uncontrolled rectifier and a switched-mode rectifier*

(3.2). This is useful at higher speeds, when the alternator back-emf is much greater than the DC link voltage. At high speeds, the alternator output current does not vary significantly with the DC link voltage, thus the alternator can be considered a constant current source. In this case the SMR acts as a current chopper, with the duty-cycle d of the switch determining the fraction of the input current which is delivered to the load versus that which flows through the switch to ground (see Fig. 3.5). This allows for simple control of the output power between zero and maximum and is the basis for output voltage regulation in the interior PM alternator. The output current vs. speed curve of the alternator when using a switched-mode rectifier as compared with an uncontrolled rectifier is illustrated in Fig. 3.4.

The constant duty-cycle control, which effectively produces a six-step voltage waveform at the motor terminals, causes distortion of the current waveform, particularly at lower speeds.

$$I_{OUT} = (1 - d)I_{IN} \tag{3.2}$$

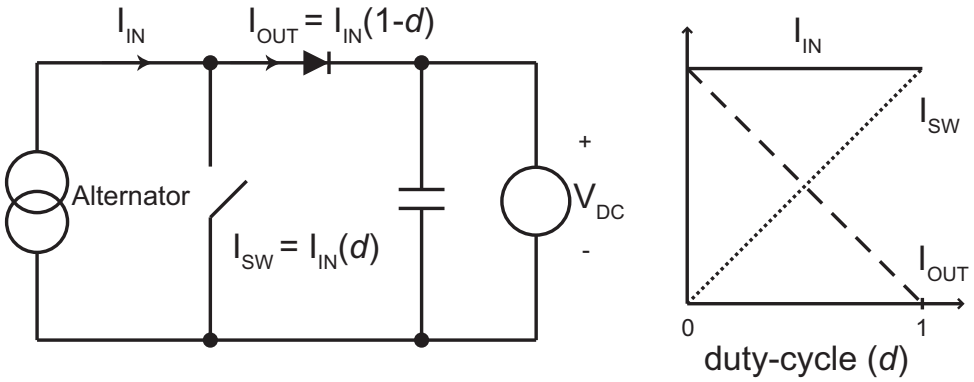

Figure 3.5: *Duty-cycle control of alternator output current with the alternator operating as a constant current source at high speeds*

3.3 SMR Modelling

The effects of SMR switching using (3.1) and (3.2) can be illustrated in the scaling of the calculated interior PM machine VI loci as duty-cycle is varied. Figure 3.6 shows VI loci calculated using the steady-state model developed in the previous chapter after modifications to incorporate the effects of SMR switching. The ability to lower the effective DC link voltage allows the alternator to generate current at speeds below the normal generation threshold (see Fig. 3.4) and so the SMR duty-cycle can be adjusted to obtain useful output power down to very low speeds, as indicated by the line of maximum current in Fig. 3.7.

The output current of the SMR is dependent on the switching duty-cycle according to the relationship in (3.2), while the output power of the alternator is dependent on both the operating speed and the effective DC link voltage seen by the machine, as discussed in the previous chapter. If the actual DC link voltage is assumed to be the constant 200 V as specified for the SMR module, varying the parameters of duty-cycle and alternator speed

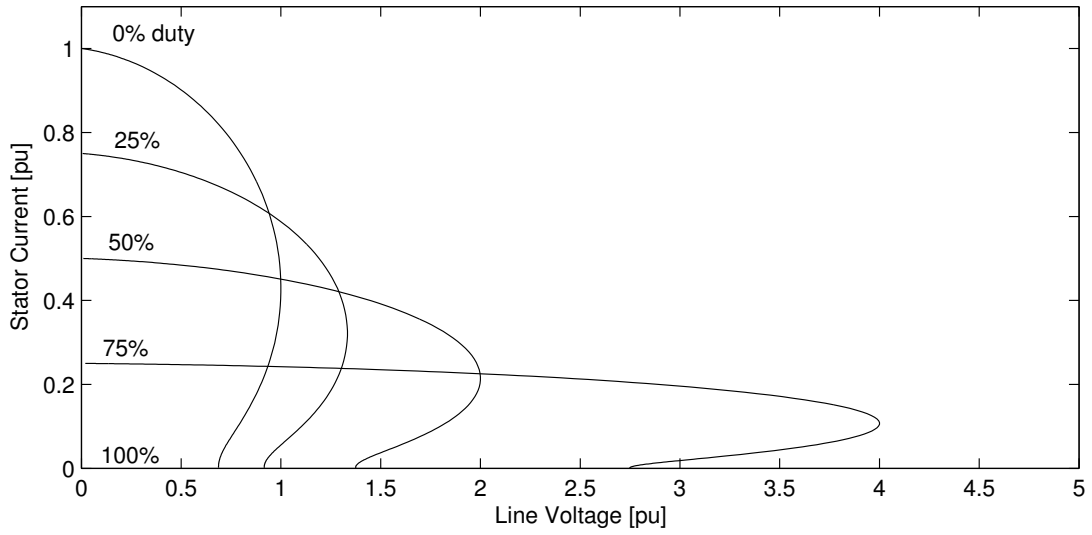

Figure 3.6: *Calculated scaling effect of duty-cycle on interior PM alternator VI locus*

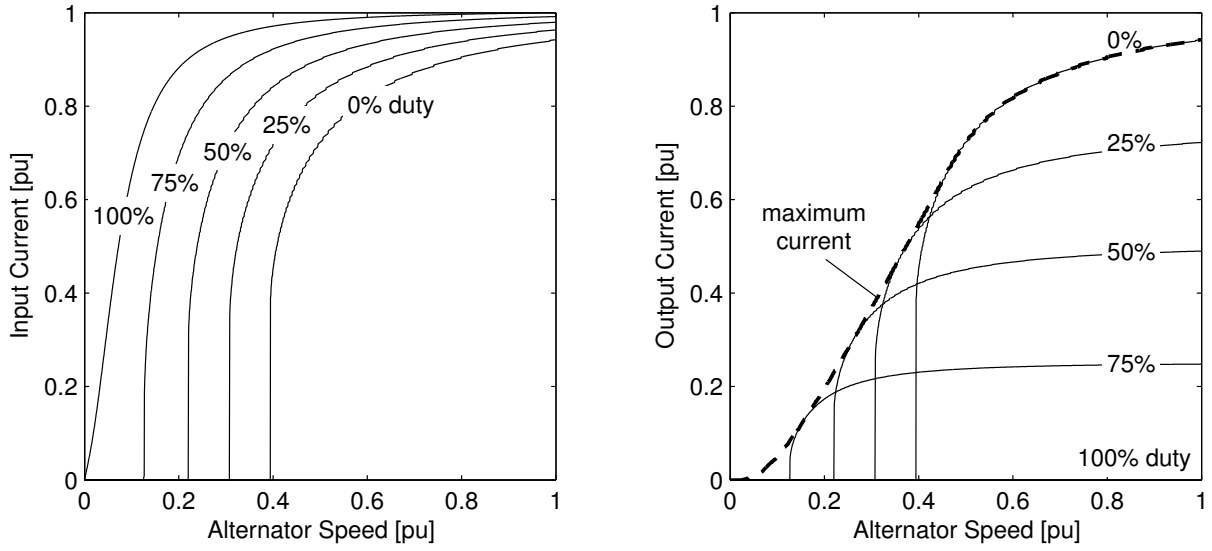

Figure 3.7: *Calculated scaling effect of duty-cycle on alternator input and output current*

produces a contour plot of DC output current as shown in Fig. 3.8. In the lower-left region of the contour plot, no output current is produced as the back-emf of the machine cannot overcome the DC link voltage. The slope of the contour illustrates the characteristic of the SMR whereby increasing the duty-cycle at operating speeds below 3,000 rpm may allow more current to be obtained but at the same time imposes an upper limit to the maximum obtainable output current. It can be seen that the traces in the right-hand

plot of Fig. 3.7 correspond to horizontal cross-sections of Fig. 3.8 at different duty-cycles. The line of maximum output current for a given speed is also similarly indicated on the contour plot.

A contour plot of efficiency can also be plotted (see Fig. 3.9). The efficiency is generally greater at lower speeds and at lower duty-cycles - the iron losses increase rapidly with speed and higher duty-cycles mean that a higher proportion of current flows through the SMR switch rather than to the load and hence the output power is lower.

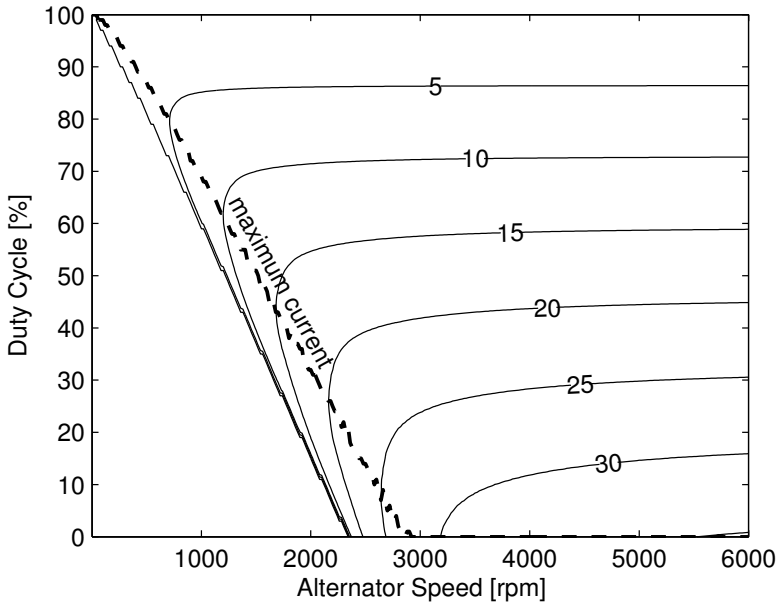

Figure 3.8: *Contour plot of calculated DC output current vs. duty-cycle and alternator speed for a 200 V DC link voltage.*

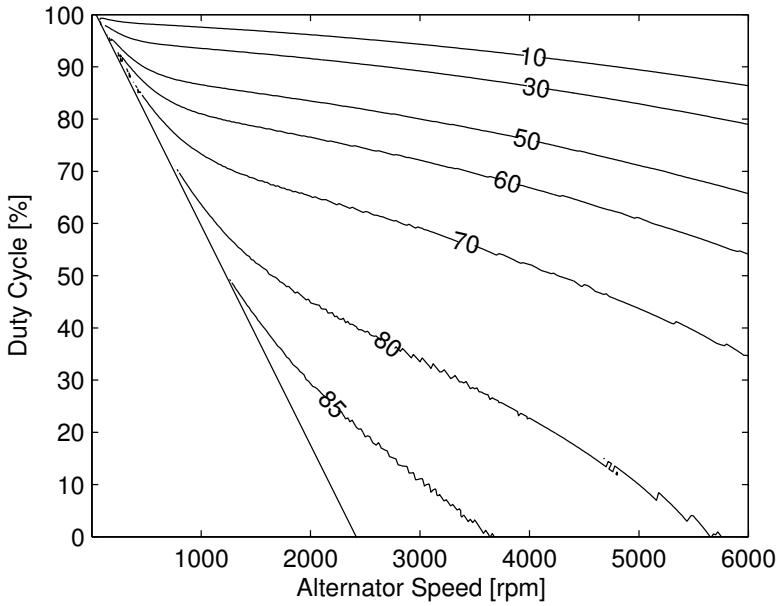

Figure 3.9: *Contour plot of calculated machine efficiency (%) vs. duty-cycle and alternator speed for a 200 V DC link voltage.*

3.4 Experimental Setup

The switched-mode rectifier power electronics unit used was based on an existing 200 V, 50 A, three-phase inverter (see Fig. 3.10). So as to match the inverter voltage rating, the interior PM alternator was fitted with a 135 V stator instead of the 415 V stator used in Chapter 2. This stator was wound with the same total amount of copper as the 415 V stator but using a third of the original number of turns and triple the original wire cross-sectional area. The reduction in the line voltage by a factor of three means the stator current is increased by the same factor, thus the 135 V alternator has a rated phase current of 26.9 Arms. Since the 135 V and 415 V stators are identical apart from the number of turns and they have the same stator slot copper packing factor, they should have the same performance and efficiency.

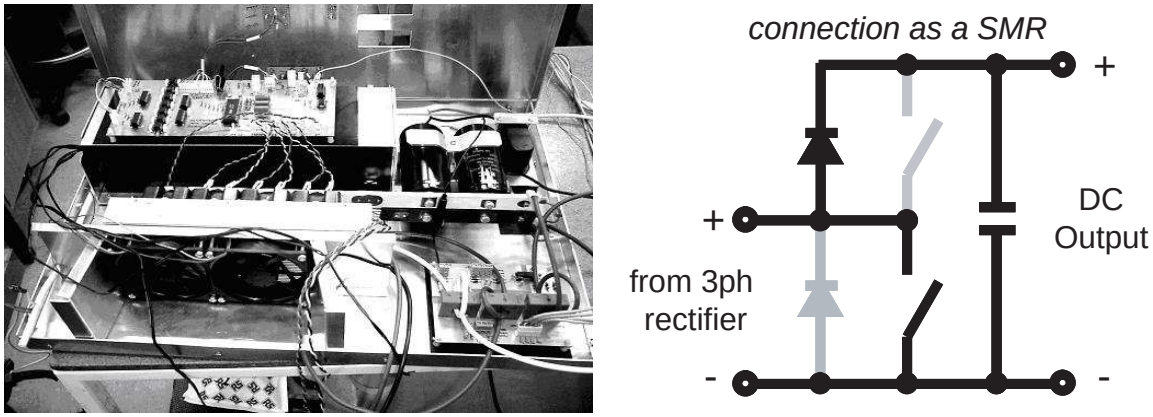

Figure 3.10: *Three-phase inverter used as a switched-mode rectifier*

The output of the alternator was connected to an external three-phase rectifier and the DC output of the rectifier was in turn connected to the "output" of one phase leg of the three-phase inverter. As illustrated in Fig. 3.10, the lower switch of the phase leg was used as the PWM-controlled SMR switch and the upper switch was kept open to allow current to pass through its free-wheeling diode into the 200 V DC link voltage.

During open-loop testing which required a constant DC link voltage, this was supplied from the rectified output of a three-phase variable transformer connected to 240 V mains voltage (see Fig. 3.11). A resistor bank was connected across the DC link to absorb the power generated by the alternator. During tests, the variable transformer was constantly adjusted to maintain a steady 200 V DC link voltage despite changes due to its voltage regulation.

During closed-loop tests where the output voltage of the SMR was regulated by a microcontroller, the output of the SMR was connected only to a resistive load. The SMR unit also incorporates an internal overvoltage protection circuit which, when triggered by a DC link voltage exceeding 330 V, shunts all generated power to an externally connected load bank in order to maintain a safe DC link voltage. To ensure safety, this feature was tested at the start of each experiment.

In both open-loop and closed-loop tests, a Mitsubishi MSA0654 microcontroller was used to provide the PWM control signal to the SMR. In open-loop tests, the duty-cycle was manually adjustable in real-time using control buttons. In closed-loop tests, the appropriate duty-cycle was calculated by the microcontroller based on the DC link voltage. In order to improve the DC link voltage measurement, it was low-pass filtered to remove high-frequency noise and averaged based on multiple readings taken simultaneously using several pins of the analog-to-digital converter module of the microcontroller.

The DC input current I_{IN} entering the SMR switch and the DC output current I_{OUT} delivered to the load were measured using 200 A shunts connected to voltmeters.

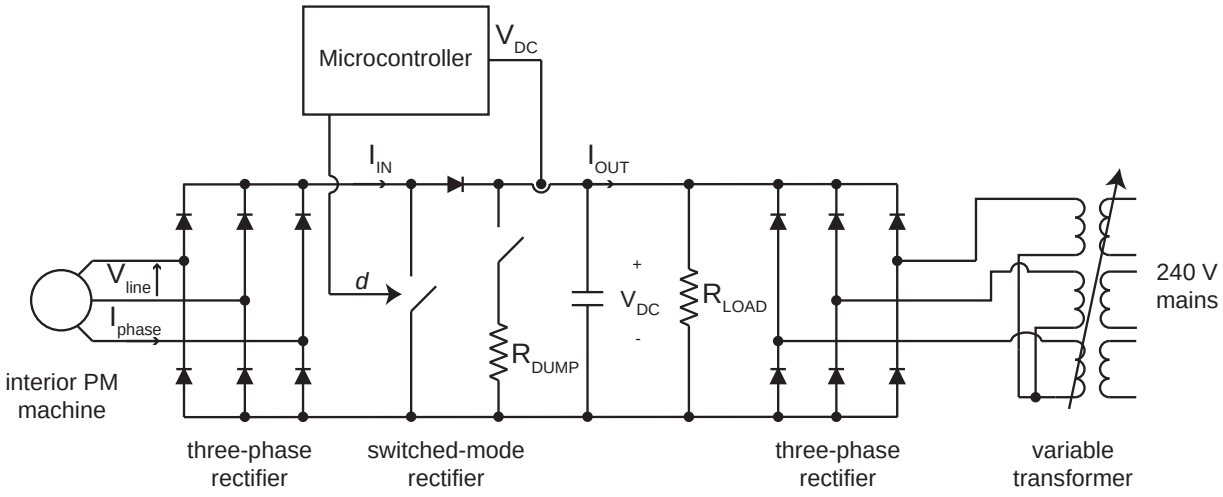

Figure 3.11: *Experimental configuration for open-loop SMR testing*

The data in Table 3.1 and the inductance curves (see Fig. 3.12) for the 135 V stator were used with the steady-state model introduced in Chapter 2 to predict the steady-state performance of the alternator. These inductance curves were obtained by scaling the curves from the 415 V stator (see Fig. 2.23) by the square of the ratio of the measured open-circuit back-EMF voltages.

A simple check performed by comparing the measured alternator short-circuit current

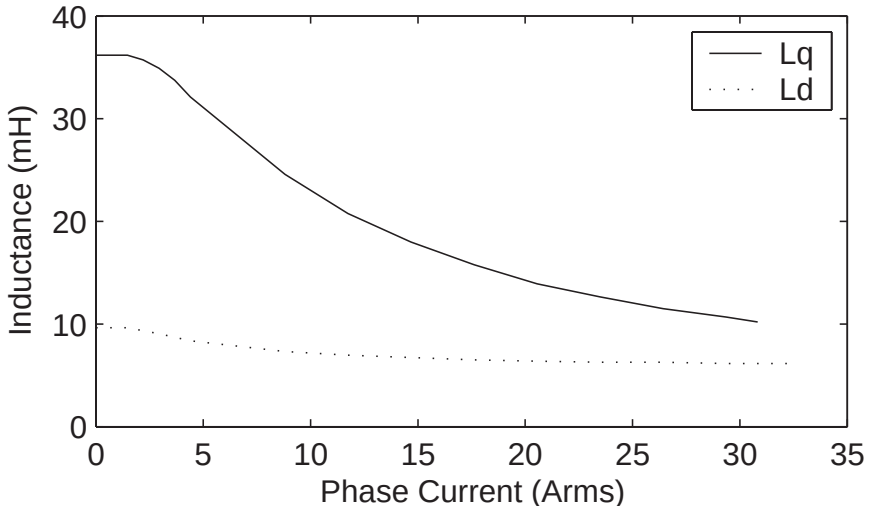

Figure 3.12: *d-axis and q-axis inductance saturation curves for the interior PM alternator with 135 V stator obtained by scaling the 415 V stator measurements*

and torque versus speed against the calculated curves (see Fig. 3.13) showed good accuracy in predicting the high-speed short-circuit current however there is a slight discrepancy at low speeds. This indicates that the saturated d-axis inductance is accurately modelled but the calculated q-axis inductance may be slightly in error.

Calculated DC voltage-current (VI) and voltage-power (VP) loci are shown in Fig. 3.14, together with measurements taken from the alternator operating into a rectifier and resistive load. As seen in Chapter 2, the measured voltage overshoot is substantially less than the predicted overshoot, and in fact the measured overshoot is almost zero. Hysteresis

Table 3.1: *Interior PM alternator parameters with 415 V and 135 V stators*

Parameter	**415 V Stator**	**135 V Stator**
q-axis inductance (mH, unsat'd)	312	36.3
d-axis inductance (mH, sat'd)	53	6.15
max. saliency ratio	5.87	5.87
stator phase resistance (Ω)	3.0	0.33
magnetic flux-linkage (Vs peak)	0.704	0.204
open-circuit line-to-line back-emf @ 1,500 rpm (Vrms)	271.2	92.4
short-circuit current @ 1,500 rpm (Arms)	9.4	26.9

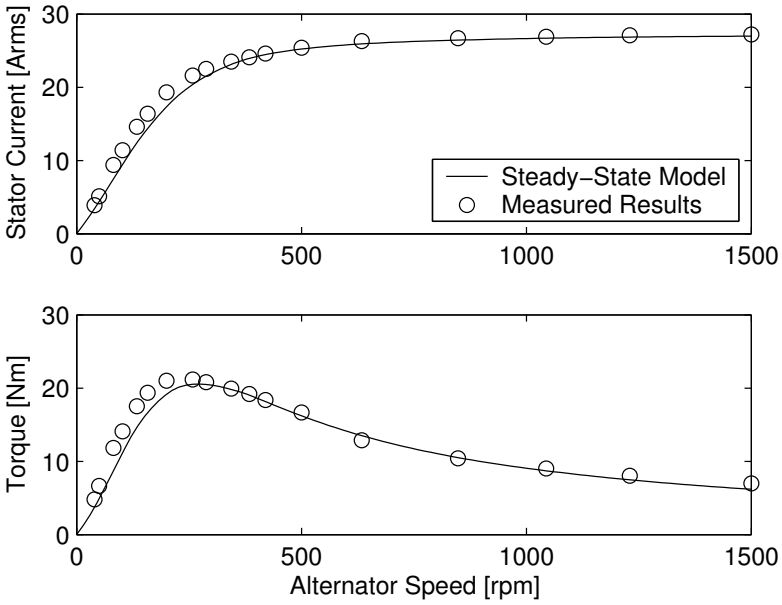

Figure 3.13: *135 V alternator short-circuit current and torque vs. speed*

therefore has little effect on the operation of the machine as an alternator with an SMR. A solid vertical line indicates the 200 V DC link voltage of the SMR. It can be seen that the 1,800 rpm locus does not intersect this line and therefore if the alternator was operating in uncontrolled generation, i.e. with a rectifier and 200 V voltage source load, no power would be generated at that speed. At 3,000 rpm, a measured output power of approximately 6 kW is obtained.

3.5 Open-Loop System Response

This section examines the test results obtained from the 135 V interior PM alternator with SMR operating into a constant voltage source load of 200 V DC. The steady-state response of alternator output current, power and efficiency to varying duty-cycle was investigated over several operating speeds.

3.5.1 Voltage and Current Waveforms

Typical stator voltage and current waveforms recorded from the alternator during operation with the switched-mode rectifier are shown in Fig. 3.15. A low PWM switching frequency of 800 Hz was used instead of the 4 kHz used in actual tests in order to clearly

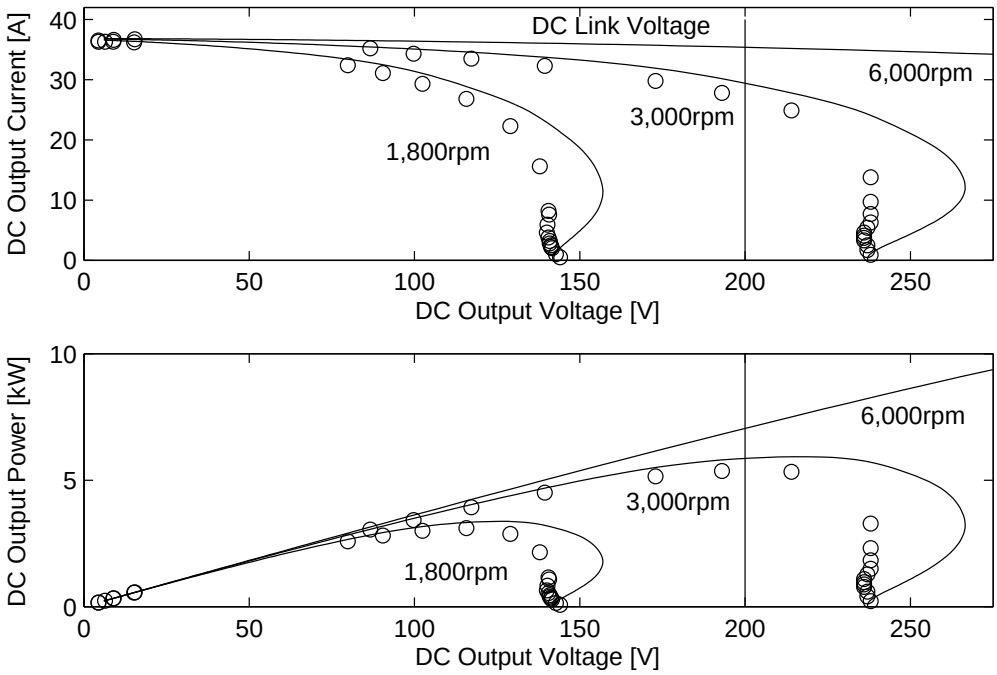

Figure 3.14: *Calculated alternator DC VI and VP loci at various speeds, with experimental points (circles) for 1,800 and 3,000 rpm*

demonstrate the effect of the switching on the line voltage waveform. Even at this low switching frequency it can be verified that although the voltage waveform shows the effects of the SMR pulse-width modulation, the high-frequency switching transients are filtered by the large inductance of the alternator so that the stator current waveform remains largely sinusoidal. Small ripples are present at the peaks of the current waveform, however at the higher switching frequency used in actual experiments, these ripples were absent.

3.5.2 Steady-State Output Current Response

The steady-state response of the alternator DC input and output currents to duty-cycle commands was measured at speeds of 900, 1,800, 3,000, and 6,000 rpm while operating into a 200 V DC link voltage. Figure 3.16 shows measurements taken for each speed as the duty-cycle was varied from 0% to 100% as well as the calculated results using the steady-state model. Note that the shapes of these current versus duty-cycle curves are similar to those of the current versus voltage loci of the machine (see Fig. 3.14), except with a reversed x direction, as increasing the duty-cycle effectively decreases the DC link

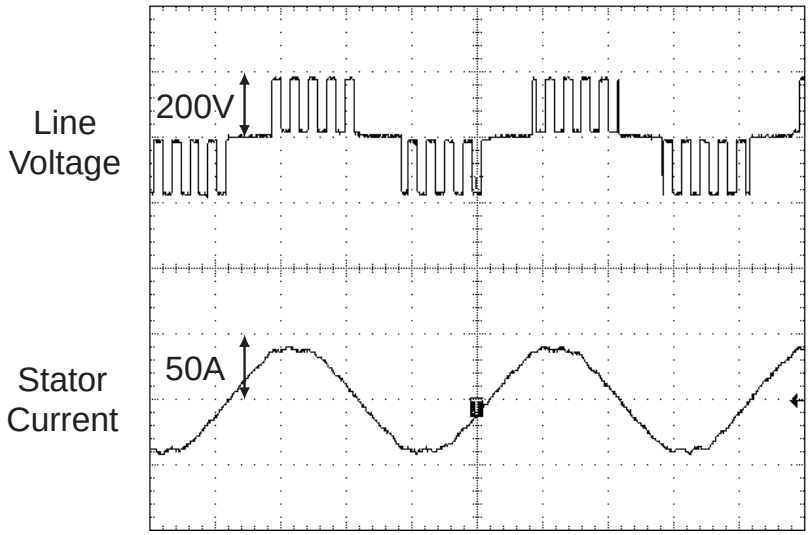

Figure 3.15: *Measured waveforms illustrating the effect of 50% duty-cycle SMR switching on the stator voltage and current*

voltage seen by the machine.

At lower speeds, there is a minimum duty-cycle below which the output power falls to zero. At this point, the effective DC link voltage $V_{EFF} = (1-d)V_{DC}$ becomes greater than the back-emf of the machine at that speed and hence no generation occurs. At 1,800 rpm, for example, this occurs at a measured duty-cycle of about 30%. There is also a value of duty-cycle which gives maximum output current and hence power, which occurs at 40% duty-cycle for this speed.

At higher speeds such as 6,000 rpm where the machine back-emf is much higher than the DC link voltage, the DC input current is relatively constant at about 34-37 A over the entire duty-cycle range. The output current shows the expected relationship described in (3.2), however it is not perfectly linearly proportional to $(1 - d)$, as illustrated by Figure 3.17, due to the input current variation. The maximum alternator output current of 34 A with a 200 V DC link corresponds to an output power of 6.8 kW, which is significantly greater than the 6 kW high-speed output power specification.

3.5.3 Output Power and Efficiency

Calculated curves of efficiency versus output power for the alternator were compared against efficiency data derived from experimental measurements of input torque and speed, which were recorded at the same time as the data shown in Fig. 3.16. In Fig. 3.19, the

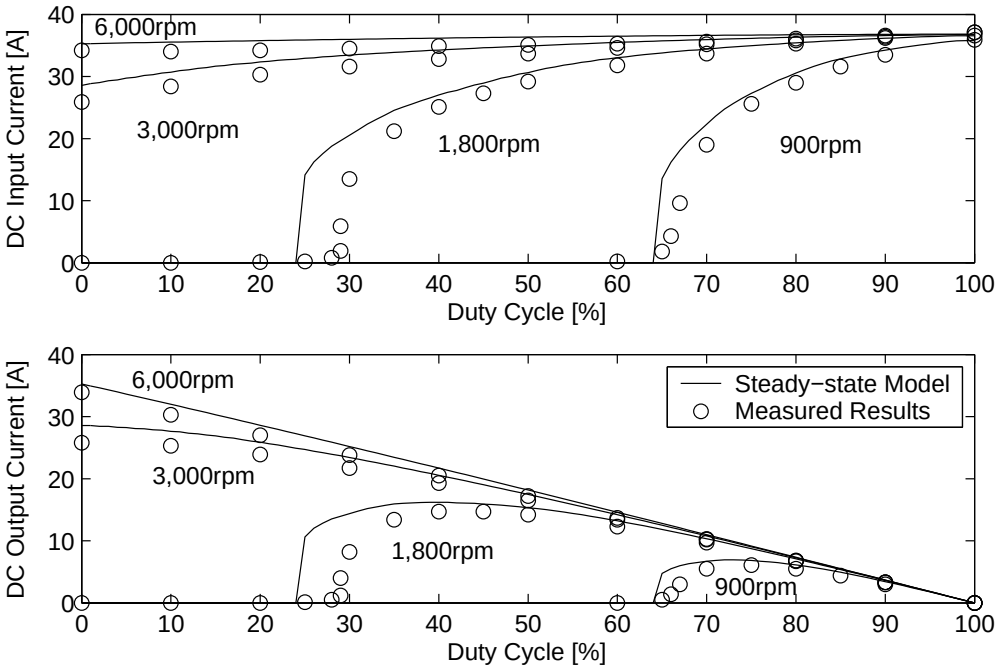

Figure 3.16: *DC input and output currents vs. duty-cycle at various speeds, with a 200 V DC link voltage*

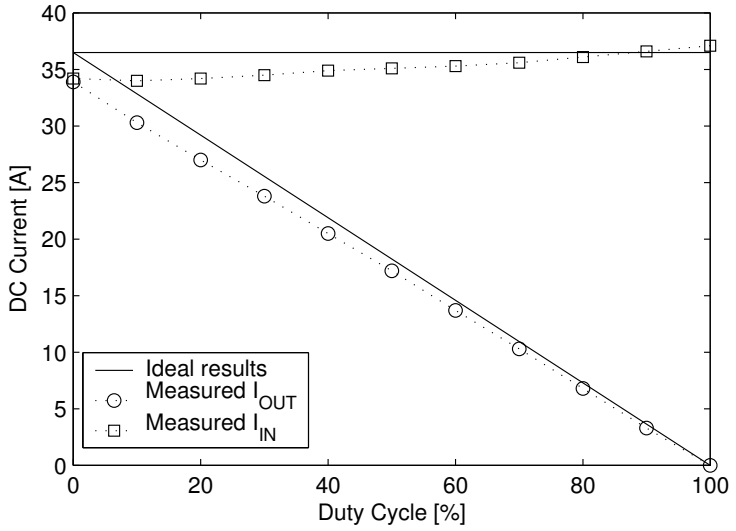

Figure 3.17: *Measured SMR DC input and DC output current versus duty-cycle from the alternator operating at 6,000 rpm plotted against ideal curves which assume that input current is independent of duty-cycle and is equal to 37 A*

calculated curves (solid lines) neglect the effect of iron losses and hence substantially over-predict the efficiency, particularly at higher speeds. As shown in Fig. 3.18, these losses increase rapidly with speed and are significant. In Fig. 3.20 the steady-state model was modified assuming that the iron losses under field-weakening are equivalent to the short-circuit iron losses. This approximation is reasonable as the output voltage is much less than the back-emf over most of the speed range. Taking this into account, the measured results now show a good match with the model predictions.

Figure 3.20 shows that the machine efficiency is poor at light loads but improves rapidly with increasing load. The maximum efficiency obtained is around 85% at 3,000 rpm and 82% at 1,800 rpm. At 6,000 rpm the efficiency is about 75% at an output power of 6 kW. For a given output power, efficiency drops significantly with increasing speed due to the high iron losses, e.g. with a 2 kW output power, the efficiency at 1,800 rpm is 65% but this drops to 50% at 6,000 rpm.

This poor light load efficiency is inherent in the inverterless concept - there exist high stator currents and hence high copper losses under all operating conditions, including light loads. The light load efficiency could be improved by oversizing the alternator to reduce the stator resistance and hence the copper losses. Reducing the stator resistance would increase the low speed output power slightly but have no effect on the high speed output power. An interesting point is that at lower speeds, higher efficiency can be achieved by operating in the 'non-linear' region of the curve, that is, using a duty-cycle which is less than the duty-cycle at which maximum output power is obtained. For instance, at 900 rpm it is possible to produce an output power of 500 W at 80% efficiency. This is in contrast with an efficiency of about 15% while operating in the linear region of the curve to obtain the same output power. The higher efficiency is due to the lower stator currents and hence copper losses in this condition. The disadvantage of this approach is that it incurs greater control complexity due to the sensitivity to the operating speed at this operating point.

The steady-state model prediction for the maximum generating power of the interior PM alternator with an SMR over speeds from 0 to 6,000 rpm is shown in Fig. 3.21 while operating into a 200 V DC link voltage. The experimental points were obtained by manually adjusting the duty-cycle at each speed to maximise the output power. The output power increases linearly from standstill up to about 3,000 rpm, after which the output power remains relatively constant. Below this speed, the SMR is acting as a boost rectifier, applying a non-zero duty-cycle to match the alternator output voltage to the higher DC link voltage.

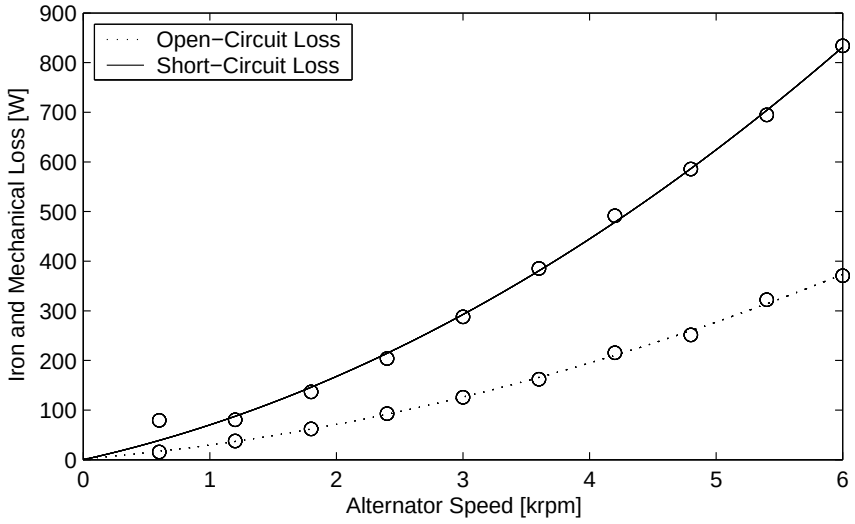

Figure 3.18: *Measured alternator open-circuit and short-circuit iron and mechanical losses with speed*

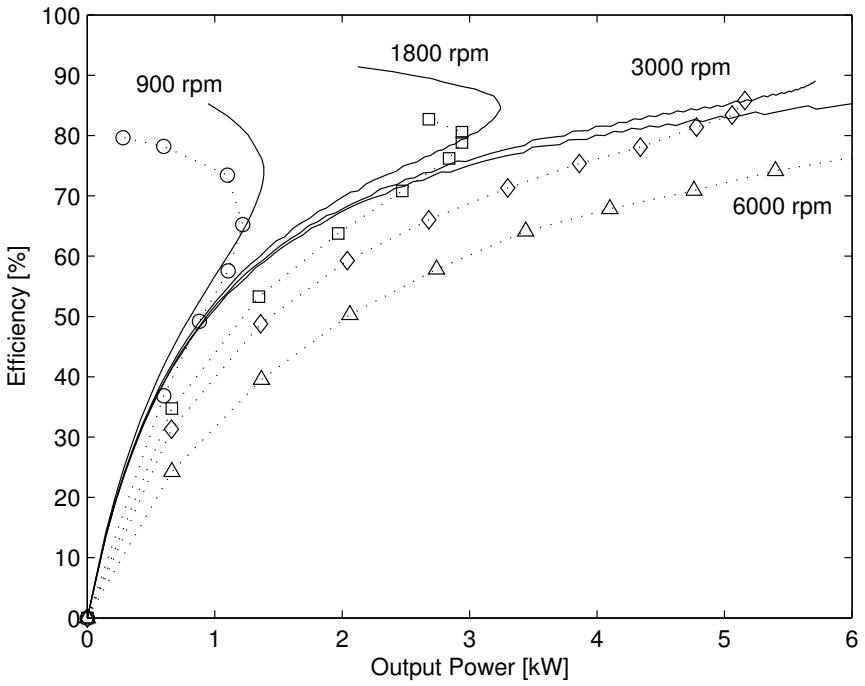

Figure 3.19: *Alternator efficiency vs. DC output power for various alternator speeds, showing steady-state model predictions neglecting iron loss (solid lines) and measured results (dotted lines)*

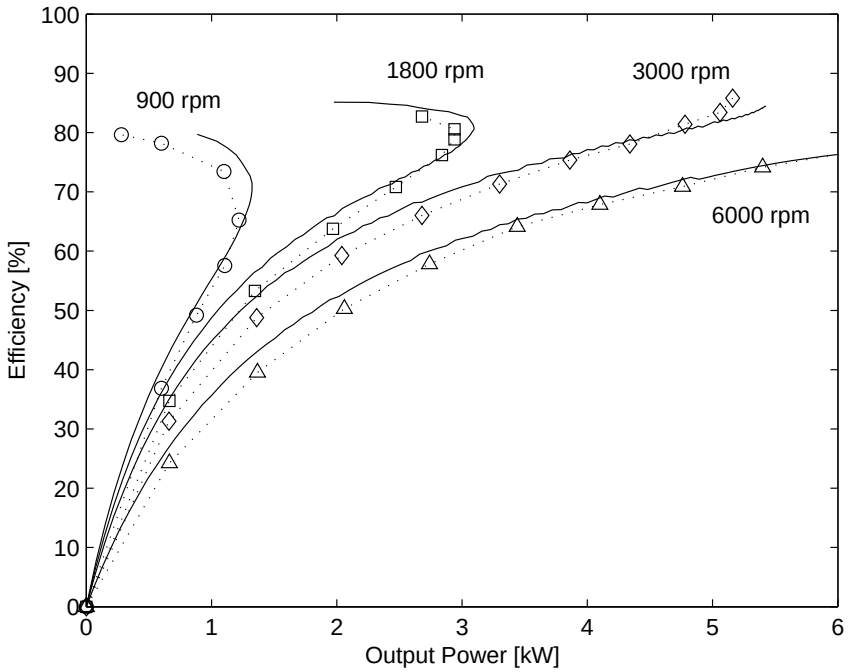

Figure 3.20: *Alternator efficiency vs. DC output power for various alternator speeds, showing steady-state model predictions incorporating iron loss (solid lines) and measured results (dotted lines)*

At 6,000 rpm, the maximum measured output power obtained is around 6.6 kW, with an efficiency of about 80%. The measured output power at engine idle (1,800 rpm at the alternator, assuming a 3:1 belt ratio) is 2.8 kW, which is significantly below the 4 kW high power alternator specification (dashed line). This measured 2.8 kW idle-speed power result is also approximately 20% lower than the expected 3.5 kW as calculated by the steady-state model. This is addressed in Chapter 4, which examines an approach to increase the idle-speed output power.

Whereas the earlier power measurements taken with a three-phase resistive load (see Fig. 2.28) matched the steady-state model predictions very closely, it can be seen that the measured output power with the SMR is slightly lower due to the additional losses. The plots of input torque and efficiency in Fig. 3.21 show steady-state model predictions both with iron losses (solid lines) and without iron losses (dashed lines). To a first approximation, iron losses do not affect the electrical output power but only increase the required input torque, thus decreasing the system efficiency. The measured results show a good correspondence to the steady-state model predictions with iron loss.

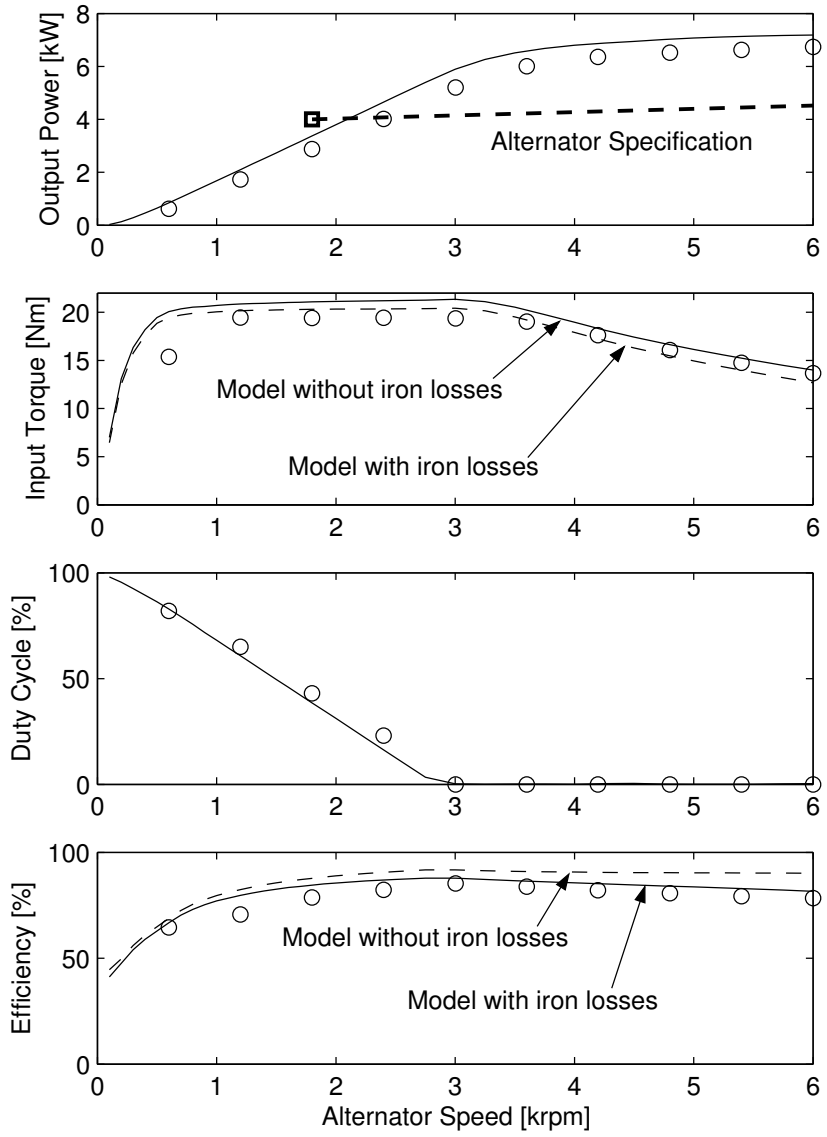

Figure 3.21: *Alternator maximum generating output power, input torque, duty-cycle and efficiency vs. speed, showing steady-state model predictions (lines) and measured results (circles), for a 200 V DC link voltage*

3.5.4 Dynamic Duty-Cycle Response

The frequency response of the SMR output current was measured by subjecting the SMR to a sinusoidally-varying duty-cycle command while the alternator generated current into a DC voltage source load. In this case the dynamometer was limited to 1,800 rpm to avoid thermal issues when conducting tests for extended periods of time.

A 50 V DC link voltage was chosen as this is much smaller than the back-emf at

1,800 rpm and so allows for a larger range over which the output current to duty-cycle characteristic is linear (see Fig. 3.22).

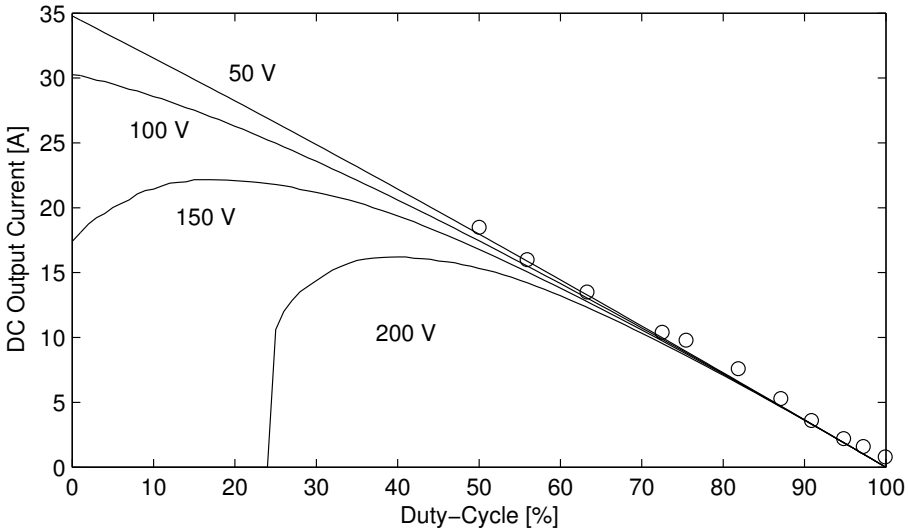

Figure 3.22: *Calculated DC output current (lines) vs. duty cycle at 1,800 rpm for various DC link voltages, with measured current (circles) for a 50 V DC link.*

To measure the duty-cycle frequency response, the MSA0654 microcontroller was programmed to accept a 0 - 5 V input voltage and generate a PWM waveform with a duty-cycle dependent on the input voltage. The PWM output from the microcontroller was set to have lower and upper duty-cycle limits of 55% and 75% respectively. This range was chosen because the output current to duty-cycle response of the alternator and SMR system was more linear towards higher duty-cycles. These duty-cycle limits correspond to output current commands of 16 A and 9 A respectively (see Fig. 3.22). A sinusoidal voltage from a signal generator was fed to the microcontroller in order to obtain a PWM signal with a sinusoidally-varying duty-cycle, which was then used as the control input to the SMR switch. A 4 kHz PWM frequency was used and the SMR output current waveform was recorded for various input signal frequencies from 1 Hz to 700 Hz, in order to measure the frequency response of the system.

An example measurement of the input signal and alternator output current waveform is shown in Fig. 3.23, at a frequency of 200 Hz. The input duty-cycle sinusoid has an amplitude of 12% duty, which corresponds to an expected output current amplitude of 3.45 A, however the observed output current amplitude is only about 2 A at this frequency.

Figure 3.24 shows plots of the system gain (ratio of output current amplitude to the expected amplitude) and the phase difference between the output and the input. The gain

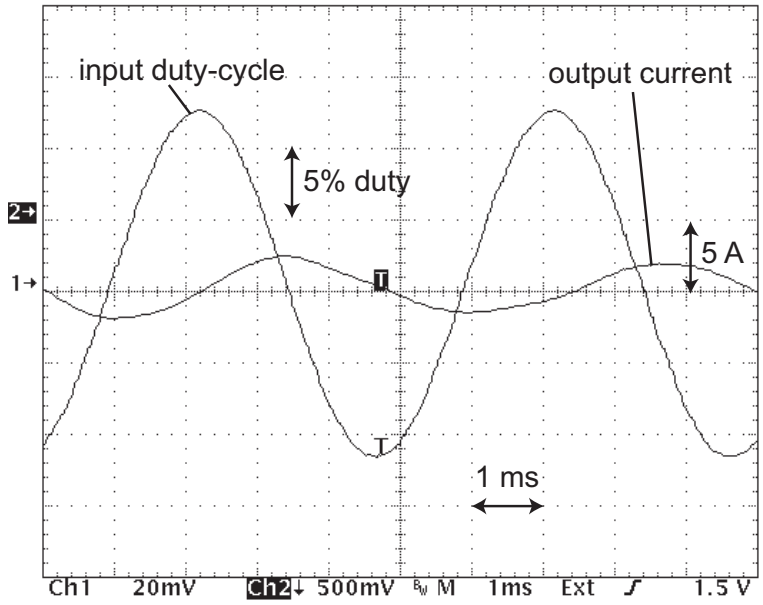

Figure 3.23: *Duty-cycle command with a frequency of 200 Hz and corresponding alternator output current waveform (averaged signals shown)*

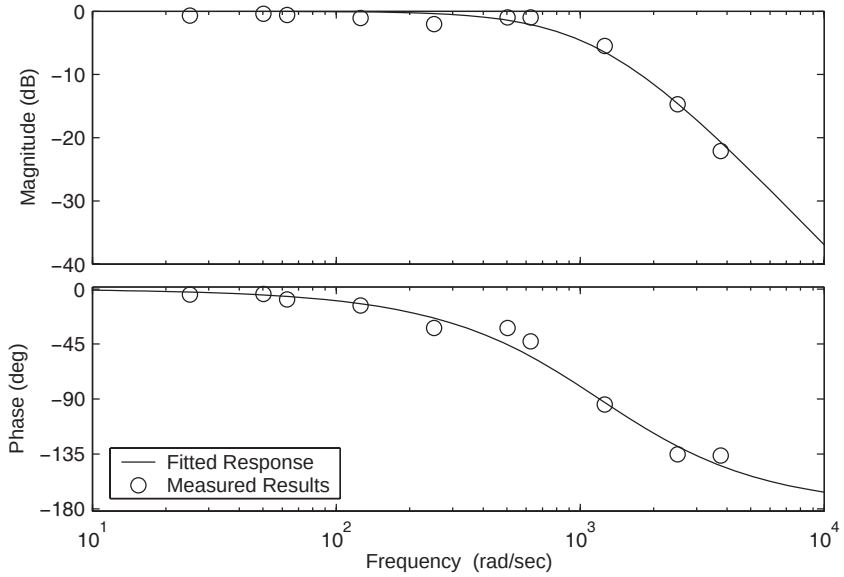

Figure 3.24: *Measured open-loop frequency response (circles) and fitted curves (lines) for the alternator and SMR at 1,800 rpm with a 50 V DC link voltage*

response of the system remains flat up to a corner frequency of around 600rad/s (95 Hz). The system transfer function was approximated by fitting a second-order response to the

measured results, giving the following open-loop system transfer function $G(s)$, with a double pole at 1200 rad/s:

$$G(s) = \frac{1200^2}{(s + 1200)^2} \tag{3.3}$$

From (3.2) and (3.3), the complete open-loop response of the alternator output current to duty-cycle can be described by (3.4):

$$I_{OUT} = 36 \cdot d' \cdot \frac{1200^2}{(s + 1200)^2}, \text{ where } d' = (1 - d) \tag{3.4}$$

A Simulink model incorporating the transfer function $G(s)$ was developed to predict the dynamic response of the alternator output current.

As a simple validation of the model, Fig. 3.25 compares the alternator step response predicted by the model to the experimentally measured waveform. The experimental waveform was obtained by applying a periodic step change between 80% and 90% duty-cycle to the SMR switch while the alternator was generating at 1,800 rpm into a DC voltage source load of 50 V. As expected from Fig. 3.22, as the duty-cycle changes from 80% to 90%, the output current changes from 7.2 A to 3.6 A respectively. Although the steady-state output matches the predictions, the time constant predicted by simulation appears slightly longer than the measured time constant. Note that there is a 600 Hz ripple modulated onto the current waveform. This is due to the three-phase rectifier, which causes a ripple of six times the electrical frequency of the machine. There is also a 4 kHz ripple corresponding to the switching frequency of the SMR.

The mismatch in the predicted time constant suggests that the measured open-loop frequency response is inaccurate. The reason for this discrepancy is unknown but for the purpose of controller design, a transfer function with double poles at 4000 rad/s instead of 1200 rad/s was used, which provides an output consistent with the measured step response.

3.6 Controller Design and Implementation

The purpose of the closed-loop controller is to regulate the output voltage of the alternator. This is achieved by adjusting the duty-cycle of the SMR switch in order to control the output current flowing to the load. It was decided to design a proportional controller to control the closed loop system, as represented in Fig. 3.26. This system could then

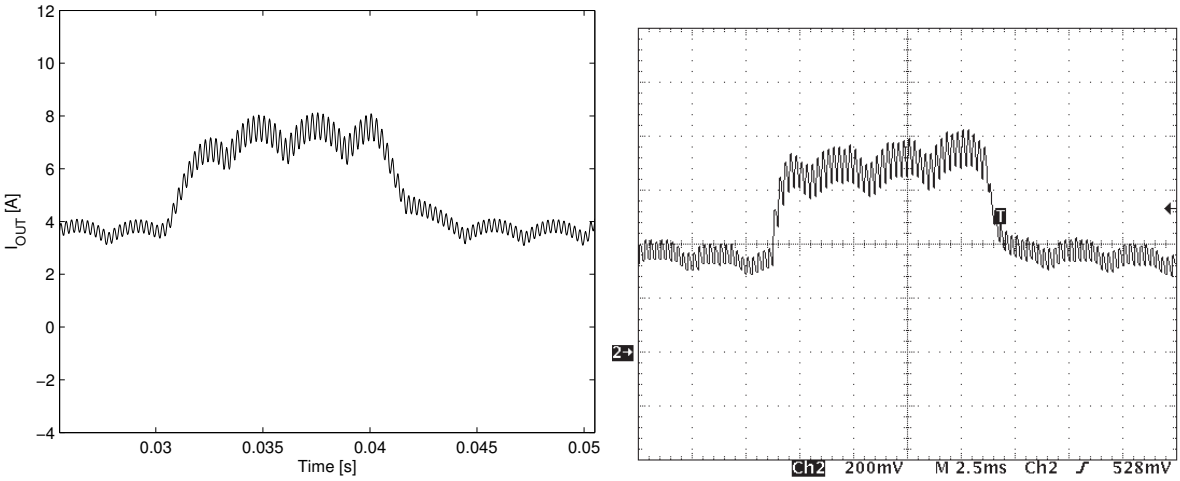

Figure 3.25: *Calculated (left) and measured (right) dynamic response of the DC output current to step changes in switching duty-cycle at 1,800 rpm*

regulate the output voltage using a simple linear control law (see Fig. 3.27).

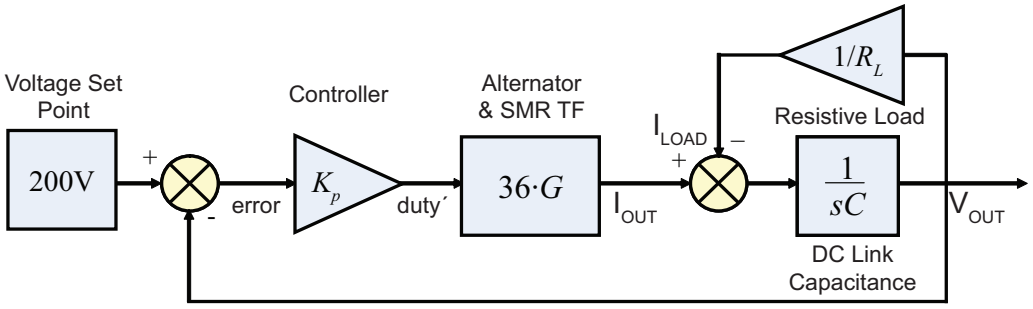

Figure 3.26: *System diagram of the closed-loop system with a proportional controller*

The value of the DC link capacitance, C in Fig. 3.26 is 3,000 μF. The forward transfer function $F(s)$ is then:

$$F(s) = 36 \cdot G(s) \cdot \frac{1}{sC} = \frac{5.76 \times 10^8}{0.003s^3 + 24s^2 + 48000s} \tag{3.5}$$

3.6.1 Limits of Stability

With a simple proportional controller, the design variables to be selected are the value of proportional gain, K_p and the control loop period. As illustrated by Fig. 3.27, larger values of proportional gain result in lower steady-state error and tighter regulation around

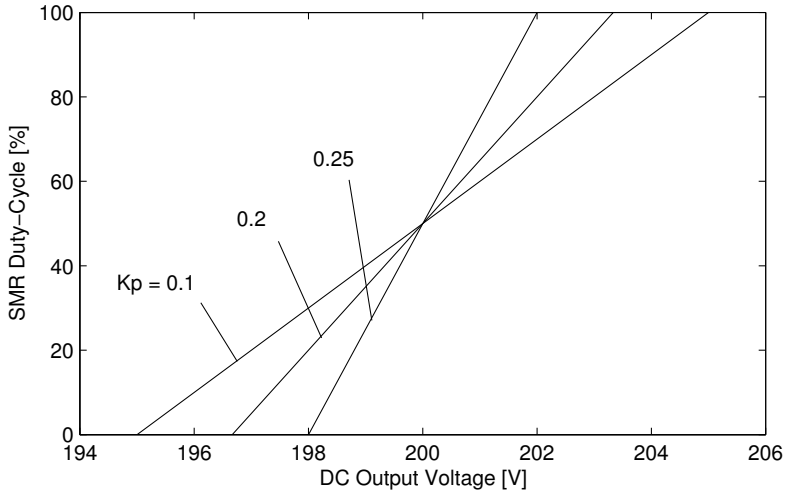

Figure 3.27: *Linear control law for the controller, for various values of proportional gain, K_p*

the voltage set point, however the maximum allowable gain is constrained by the limits of stability of the system.

The frequency response of $F(s)$ is shown in Fig. 3.28. The combined phase delay imposed by the alternator and the DC link capacitance causes the phase of the closed-loop system to exceed -180°at a frequency lower than the gain crossover frequency. The gain margin, G_m is -3.52 dB, indicating that for stability, the gain should be at least 1.5 times smaller than unity, i.e. a stability threshold of $K_p = 0.67$.

The loop period or sampling time T_s of the digital controller affects how quickly the controller responds to changes in the system. As the sampling time increases, the bandwidth decreases, which means that the controller responds more slowly to output voltage changes. It was decided that rather than setting the sampling time through the timing of an interrupt routine, the Mitsubishi microcontroller would be allowed to iterate through the control loop continuously in order to obtain the best possible performance. The time taken to execute one iteration of the control loop was measured to be 284 μs.

Figure 3.29 shows the general shape of the discrete root locus plot of the alternator open-loop system with a sampling time of 284 μs. The area of interest is the region which is within the unit circle as these represent values of proportional gain which produce a stable system. A close-up of this area is shown in Fig. 3.30, where loci for sampling times of 80, 284 and 800 μs are also plotted. It can be seen that as sampling time increases, the complex poles move towards the origin. This causes the oscillatory mode associated

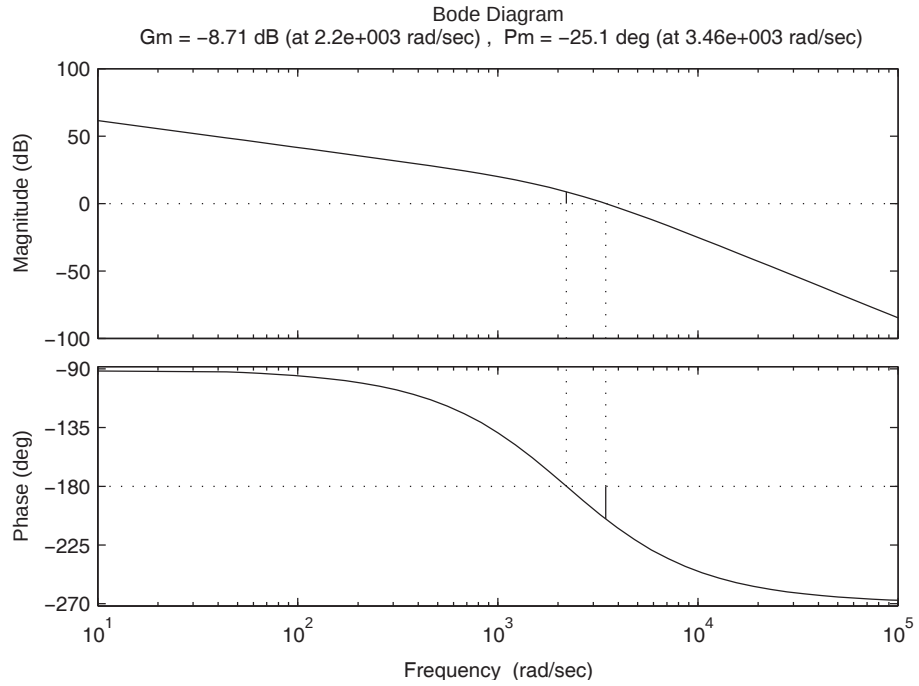

Figure 3.28: *Calculated open-loop frequency response of the interior PM alternator and SMR, showing gain and phase margins*

with the complex poles to decay faster, however this also decreases the maximum stable proportional gain, meaning that there is a trade-off between shorter settling time and smaller steady-state error. For the case of a sampling time of 284 μs, a proportional gain of greater than approximately 0.015 produces complex poles, while a gain of greater than 0.15 is unstable.

The closed-loop proportional gain is generally chosen to satisfy the steady-state error requirement of the system. For example, the 42 V specification demands steady-state variation not exceeding an upper limit of 50 V and a lower limit of 30 V. For the purpose of comparison, this range represents 47.6% of the nominal voltage. A proportional gain of $K_p = 0.1$ was chosen for the closed-loop controller, providing regulation of the DC link voltage between 195 V and 205 V as the duty-cycle changes between 0% and 100% respectively. This corresponds to a range of 5% of the nominal voltage, satisfying the steady-state specification. The root locus plot indicates that this gain should give a stable response, although the complex poles would result in some underdamped response to input transients.

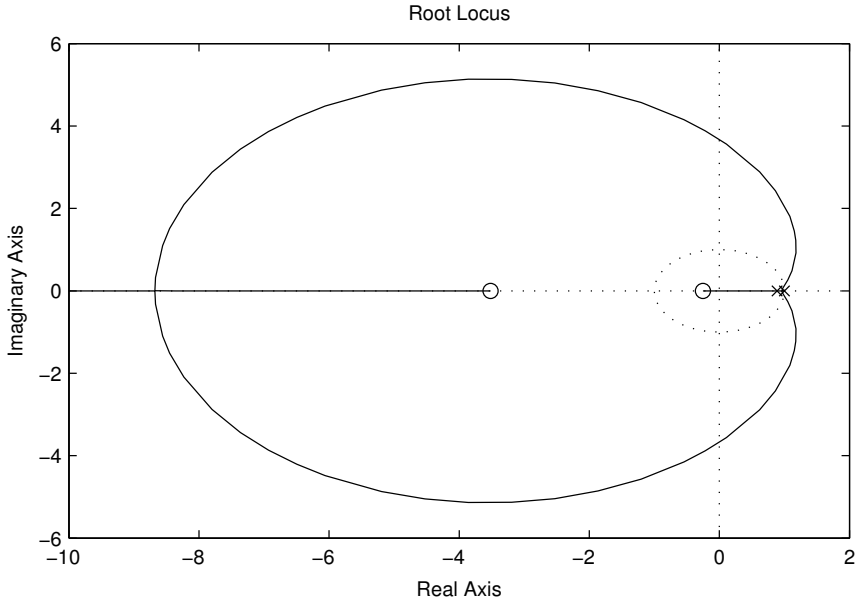

Figure 3.29: *Calculated discrete root locus plot of the open-loop system with a sampling period of 284 μs*

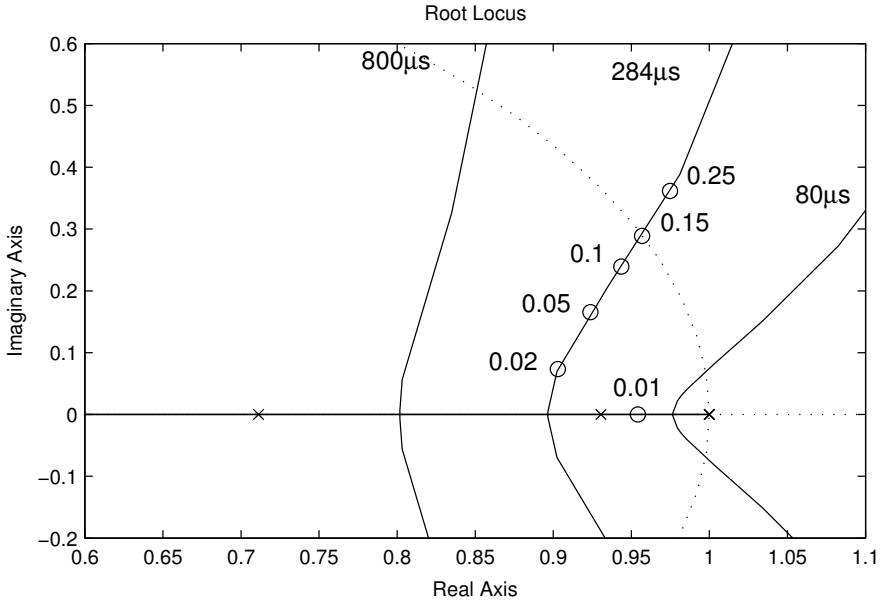

Figure 3.30: *Enlarged view showing root loci for various values of sampling time T_s, with values of proportional gain shown at various points on the locus for sampling time T_s = 284 μs*

3.6.2 Simulation

A dynamic model was developed in Simulink to predict the transient behaviour of the closed-loop alternator and SMR system. The model incorporated the effects of microcontroller loop delay and voltage signal quantisation due to analogue-to-digital conversion. Several test cases were tried on the control loop model to examine its stability and to observe its response to various stimuli such as load changes and startup transients. These results are shown in comparison with actual experimental measurements in the following section.

3.7 Closed-Loop System Response

3.7.1 Steady-State Voltage Regulation

The closed-loop voltage regulation capability of the alternator was initially tested at a low DC link voltage of 50 V to observe the control performance and then at progressively higher voltages of 100, 150 and 200 V. To obtain a regulation curve, resistive load banks were connected at the output of the SMR and the output voltage measured while the load was varied.

Figure 3.31 shows captures of the duty-cycle signal and the output voltage waveform during regulation at a 50 V DC link voltage. These three captures were taken at increasing load currents, I_{LOAD}. The output voltage appears constant and as the load current is increased the duty-cycle decreases, as expected. However, there is a slight oscillation with a frequency of about 300 Hz present in the duty-cycle signal which corresponds to the rectifier output ripple frequency. Note that this signal is actually a 0-4.9 V signal which corresponds to 0-100% duty and is produced by the control loop code in the microcontroller as a means of reporting the calculated duty-cycle command.

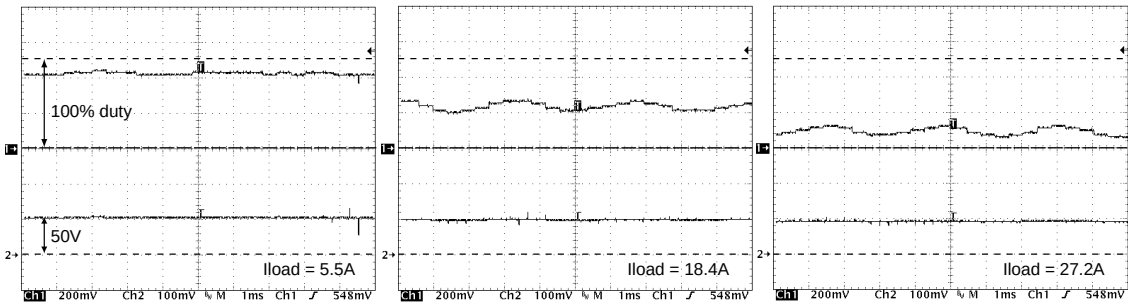

Figure 3.31: *Measured duty-cycle (top trace) and DC link voltage (bottom trace) during 50 V regulation at 1,500 rpm, at load currents of 5.5, 18.4 and 27.2 A*

The oscillation is more pronounced at a higher DC link voltage, as can be seen in Fig. 3.32, which shows the duty-cycle and output voltage for regulation at 100 V. In this particular capture the alternator is running at 1,800 rpm and the resistive load is 6.0 Ω. Hence, the alternator should supply 17.5 A to the load to maintain the output voltage. However, instead of a steady duty-cycle of 51% as dictated by the control law, the duty-cycle waveform oscillates between 0% and 80% duty-cycle with a frequency of around 33 Hz. This produces a corresponding oscillation in the output voltage between 95 V and 105 V. While the output voltage still meets the specified steady-state ripple requirements

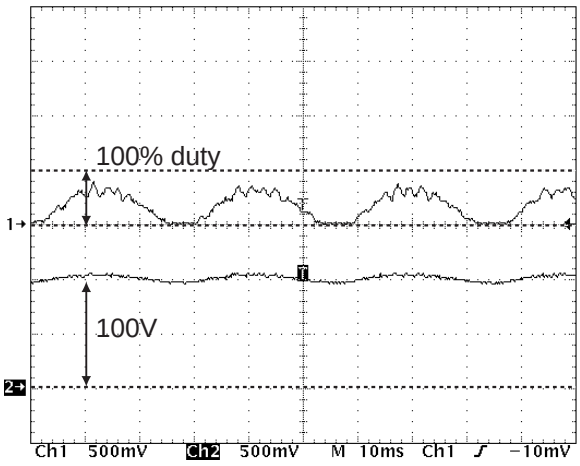

Figure 3.32: *Measured duty-cycle (top trace) and DC link voltage (bottom trace) during 100 V regulation at 1,500 rpm, with a 6.0 Ω load*

and is no doubt sufficient for the purpose of charging a battery, this undesirable oscillation produced a slight mechanical vibration in the dynamometer test rig.

Despite the oscillations observed in the closed-loop system, the steady-state results were nevertheless in accordance with the theoretical values. Figure 3.33 shows the experimentally measured points compared against theoretical curves. As the alternator operating speed was 1,500 rpm for this test, the maximum output power was limited to 2.4 kW. The value of the proportional gain ($K_p = 0.1$) determines the voltage regulation and hence the slope of the theoretical curves. There is a good correspondence between the calculated and measured results, however the theoretical curves do not take into account the power limit (shown as a dotted line), which causes the voltage to drop at high currents.

3.7.2 Transient Voltage Regulation

The closed-loop alternator system was subjected to load dumps of varying magnitude and the output voltage and SMR duty-cycle waveforms were recorded. The equipment was set up in the same way as for steady-state tests except that a second, smaller resistive load was periodically switched in parallel with the existing resistive load in order to simulate load dumps. The switching of this load was triggered by a square wave signal fed into a separate switch of the inverter as shown in Fig. 3.34.

Figure 3.35 shows captures of the duty-cycle command and the DC link voltage of the closed-loop controller running at 100 V while being subjected to load dumps of 4.4, 8.8

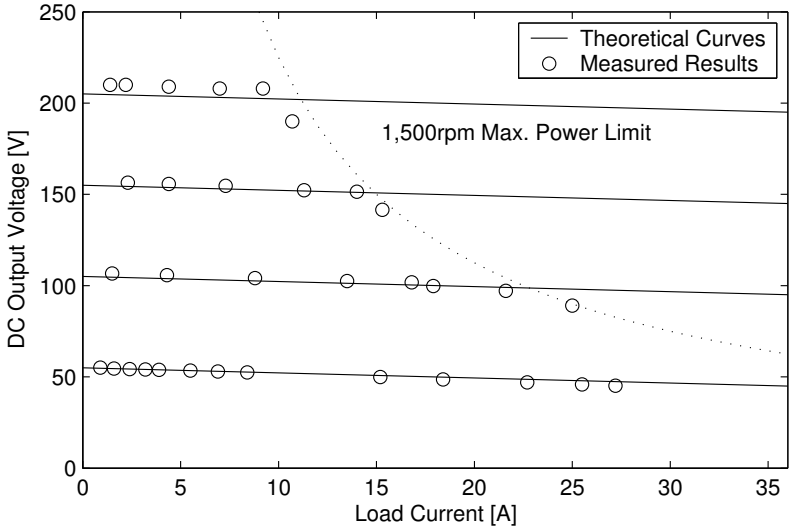

Figure 3.33: *Closed-loop voltage regulation vs. load current at 1,500 rpm, for DC link voltages of 50, 100, 150 and 200 V*

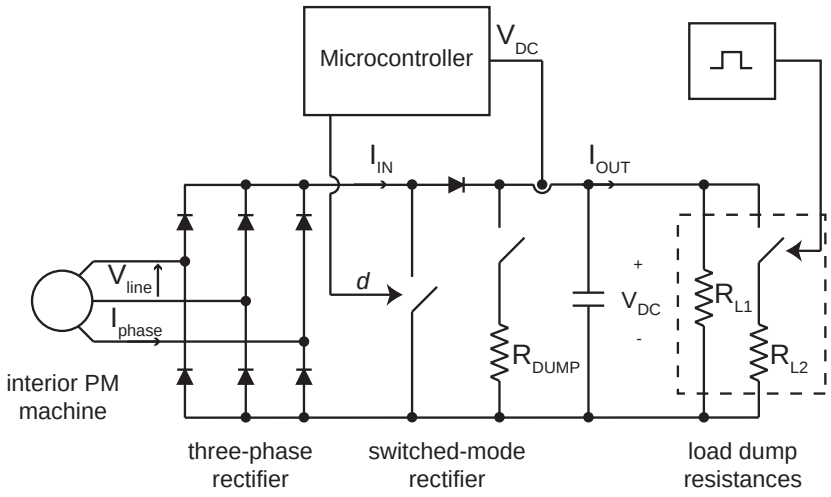

Figure 3.34: *Experimental configuration for closed-loop load dump tests*

and 12.3 A. It can be seen that the overvoltage peak is small enough that it is only readily discerned in the 12.3 A load dump. In these cases, the peak voltage reached was 110 V, i.e. 110% of nominal voltage, which is within the 42 V specification for maximum transient overvoltage. This minimal overshoot is in accordance with what should be expected given the short control loop period of 284 μs. The time required for the overvoltage to settle to steady-state level was approximately 20 ms.

The measured waveforms differ notably from the simulated waveforms, particularly at

lower duty-cycles, where the oscillations previously observed in the steady-state regulation are once again present in the measured waveform. While the simulated waveforms exhibit a slight ripple which increases in amplitude at lower duty-cycles, no large oscillations are present. The oscillations do not seem to have any impact on the load dump transient response since they do not manifest for the high duty-cycles which are applied to limit overvoltage.

The DC link was reduced from its nominal value of 200 V (corresponding to the 135 V machine rating) to 100 V to reduce the risk of causing an over-voltage on the DC link during the testing. The results obtained are effectively scaled versions of what would be obtained in a 42 V system.

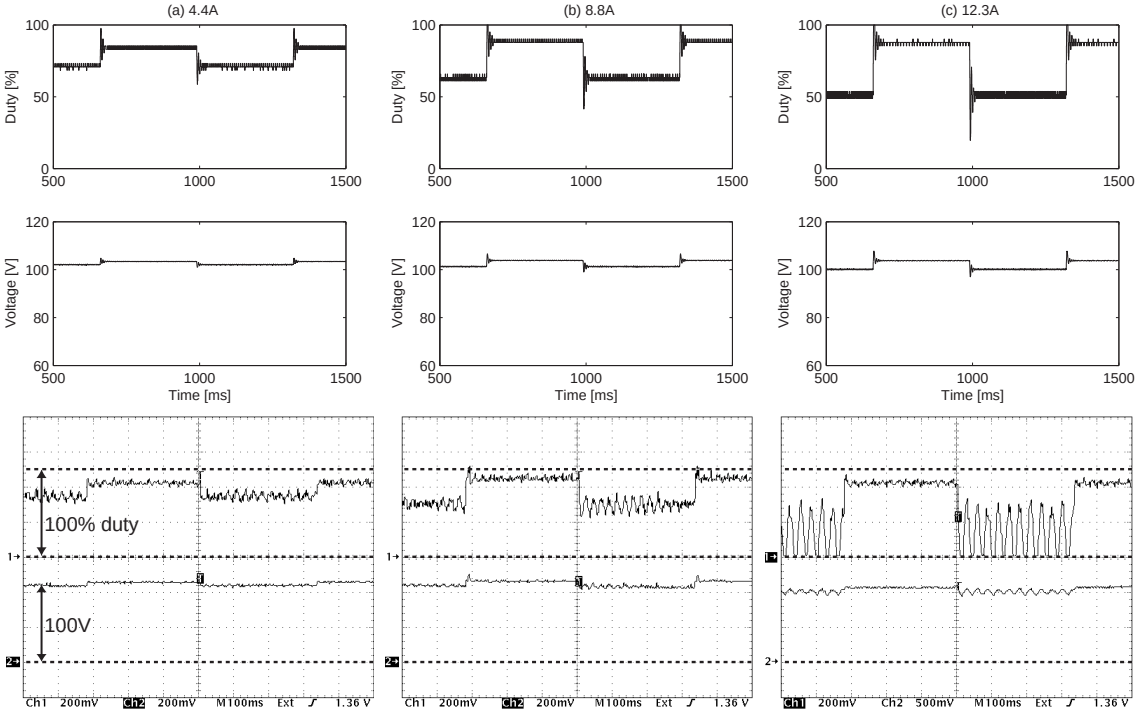

Figure 3.35: *Simulated (upper) and measured (lower) duty-cycle and DC link voltage waveforms showing the load-dump response of the closed-loop system operating at 1,800 rpm with a 100 V DC link*

3.8 Summary of Findings

This chapter has investigated the control and performance of an inverterless interior PM alternator based on a switched-mode rectifier. A simple closed-loop control system was

designed and the performance evaluated in terms of stability, transient voltage suppression and output voltage regulation versus load. The main findings are:

- A simple proportional controller is capable of regulating the alternator steady-state output voltage. Results show a 1% decrease in output voltage for 25% increase in load current, which is within the specified steady-state range of 48% of nominal voltage.
- The maximum overvoltage produced by the closed-loop system in response to a load current step of 8.8 A, representing an 880 W load dump, was 10 V. The load dump transient settled to its steady-state value after roughly 20 ms. The peak value is 110% of the nominal output voltage, which is well below the 42 V specification of 138%.

In summary, the closed-loop inverterless alternator shows promising performance as an automotive alternator, with indications that it will be able to satisfy the high power alternator specifications. However, further work is required in some areas:

- The controller duty-cycle exhibits oscillations which increase in amplitude as load current increases. These cause a corresponding output voltage ripple. Some possible causes are non-linearity in the output current response, mechanical oscillations, or digital control loop limitations.
- The open-loop transfer function derived from the measured frequency response of the alternator predicts an output current frequency response with a larger time constant than exhibited by a measured step response. This needs to be further investigated as both measurements were taken under similar conditions.
- With regards to the suppression of load dump overvoltage transients, more severe tests should be attempted. It would however be prudent to first address the issue of controller oscillations so that the mechanical effect on the dynamometer rig is minimised.

Chapter 4

Idle-Speed Power Improvement

4.1 Introduction

Obtaining sufficient alternator output power at idle speed is essential for a vehicle's electrical system to be able to sustain active electrical loads for a reasonable amount of time without undue drain on the battery. Although it is possible to adjust the engine idle speed in some vehicles such that the alternator output power alone is sufficient to supply all active loads, this is generally not desirable as the higher speed causes increased wear on both the engine and the alternator. Hence, any shortfall in electrical supply at idle speed is taken up by the battery and it is thus possible to drain the battery under heavy electrical loading.

For the high-power automotive alternator, the requirement for output power at idle speed (1,800 rpm) was specified as 4 kW. The top graph in Fig. 4.1 shows that the idle-speed output power of a conventional Lundell alternator is much less than this. Using a conventionally modulated SMR allows higher output power at high speeds but only a small improvement at idle speed. Using an inverter would substantially increase the output power (neglecting saturation) but still not meet the 4 kW requirement.

In previous chapters, the use of a load-matching SMR as a power converter was investigated as an alternative to the relatively high cost and control complexity of an inverter. It was found that although the interior PM alternator investigated in this study would easily satisfy the 4 kW idle-speed output power requirement if operated with an inverter, tests showed that it produced only 2.8 kW (see Fig. 4.1) when operated in conjunction with a SMR for load-matching. With an SMR, the output power rises linearly from zero until approximately 3,000 rpm and the required idle-speed output power of 4 kW is reached on

this slope at 2,400 rpm.

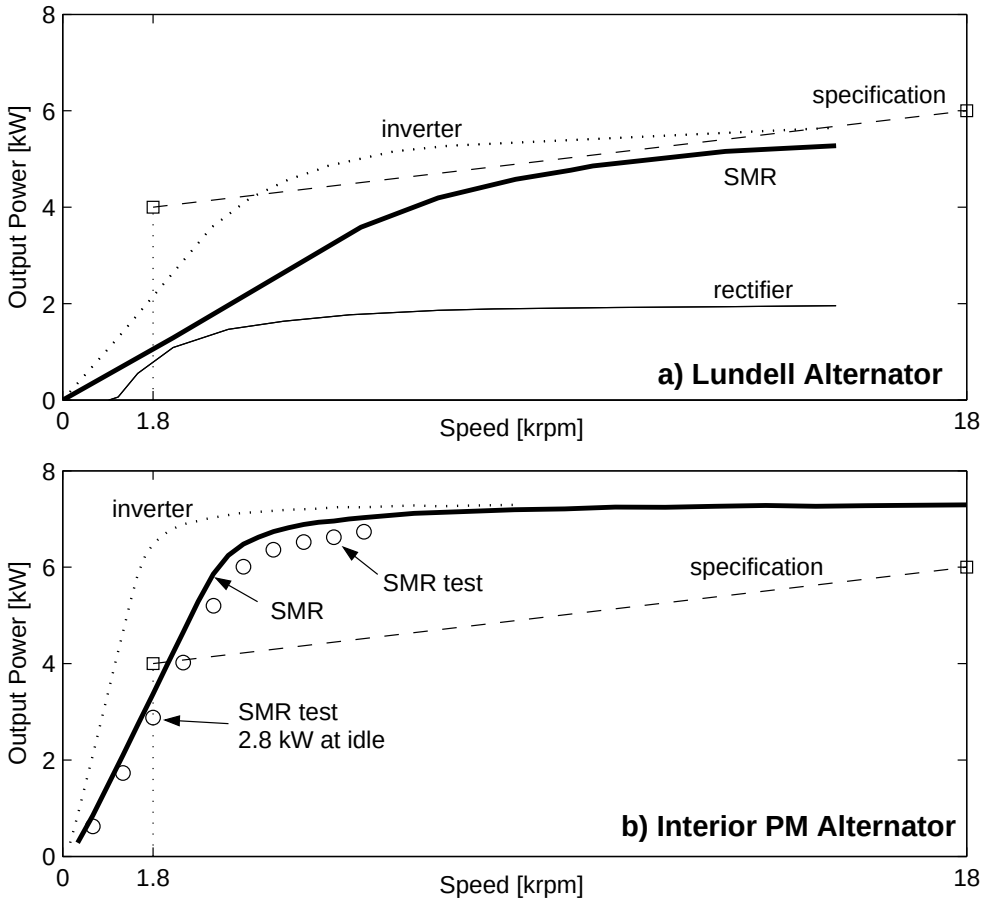

Figure 4.1: *Output power versus speed characteristics for an example a) Lundell and b) interior PM alternator using different power electronics topologies, showing calculated curves (lines) and test data using a SMR (circles)*

It is the presence of two controllable switches on all phase legs of an inverter which allows better optimisation of output power as compared to a single-switch SMR and there have been several studies which make use of the added flexibility of such controlled rectifiers to improve alternator output power. Liang et al. applied six-step waveform modulation using an inverter to achieve an increase of 43% in the idle-speed output power of a Lundell alternator [28]. Kikuchi, Manjrekar and Lipo carried out a detailed analysis of the operation of the semi-bridge rectifier for improving the shape of the input current waveform compared to an uncontrolled rectifier in a motor drive [40].

In terms of control flexibility, the semi-bridge SMR with its three controllable switches can be considered an intermediate step between an inverter and a single-switch SMR and

recent work by Rivas, Perreault and Keim [15] on a semi-bridge SMR modulation scheme achieved a 15% increase in output power of a Lundell alternator at idle speed.

In this chapter, the difference in the operation and output power capability of an inverter and a conventional single-switch SMR is discussed. The SMR modulation scheme proposed by Rivas, Perreault and Keim for a semi-bridge SMR is examined and the way in which it improves the output power at low speeds is discussed. The application of the modulation scheme to the interior PM alternator and the resulting output power performance is theoretically investigated and simulated models are constructed. The modulation scheme is implemented on a microcontroller and experimental results are obtained.

4.2 Power Converters

4.2.1 Single-Switch SMR and Inverter Low-Speed Performance

The purpose of a power converter in an automotive alternator system is to convert AC input power to DC output power with high efficiency. At any speed, the converter should maximise output power while not exceeding the rated output voltage and current of the alternator. The output power of an alternator can be expressed as the product of its voltage, current and power-factor (4.1). These quantities are in turn dependent on the load to which the alternator is connected and the operating speed. Neglecting voltage or current limits, optimum power transfer is obtained with a matched load, i.e. a load with an impedance which is the conjugate to the alternator output impedance. When comparing alternator operation using a SMR as opposed to an inverter, the difference in performance is due to the extent to which each converter is capable of adjusting the effective load impedance and power factor seen by the alternator to maximise the output power.

$$P = V I \cos\phi \tag{4.1}$$

As depicted in Fig. 4.2, to a first approximation the alternator has a purely inductive output impedance, X_s. In order to extract the optimal power, a load with a leading power factor needs to be applied. Although the single-switch SMR can adjust the magnitude of its input impedance by varying the switching duty-cycle, the input rectifier of the SMR forces the alternator phase voltage and current to be in phase and thus the alternator

is constrained to operate at unity power-factor. The SMR can therefore be considered a variable purely resistive load. In comparison, the control flexibility afforded by the additional switches in an inverter allows both its input impedance and power-factor to be varied. The inverter can therefore be modelled by a variable passive RC load. In a previous study [16], an RC load was in fact used to extract maximum power from the interior PM alternator, thus simulating the alternator performance delivered by an inverter. Figure 4.3 shows the calculated parallel three-phase resistances and capacitances required to simulate inverter operation with maximum output power without exceeding the rated voltage or current of the machine. Note the load resistance is fairly constant but the required capacitance falls rapidly with speed.

Consider in Fig. 4.2 the speed corresponding to the 'knee' in the inverter voltage versus speed characteristic (leftmost vertical dashed line). At this speed, both the inverter voltage and current are at their rated values (1 pu), the power-factor is optimum at 0.7 leading and hence the inverter output power is 1 pu x 1 pu x 0.7 = 0.7 pu. With the SMR at the same operating speed, the unity power-factor constraint means that at the maximum output power operating point the output current is only 0.7 pu and the output voltage is only 0.5 pu. The SMR output power is then 0.5 pu x 0.7 pu x 1 = 0.35 pu, or half the inverter output power.

It can be seen that at low speeds, the inverter can supply the required load impedance and input power-factor (0.7 leading) to maintain rated output current and so extracts twice the power achievable with a SMR at that speed. At high speeds, the optimal power-factor approaches unity and hence the output powers obtained with both SMR and inverter are comparable.

4.2.2 Proposed Semi-Bridge SMR Modulation Scheme

In the proposed semi-bridge SMR modulation scheme, the PWM duty-cycle is modulated to control the effective voltage applied to each phase. Since only the lower switch in each phase of the semi-bridge SMR is used, the voltage can only be controlled during the positive half-cycle of the phase current. When the phase current is positive, controlling the duty-cycle d of the switch controls the effective phase to ground voltage V_{EFF} applied to the phase, where the effective voltage $V_{EFF} = V_{DC}(1 - d)$ and V_{DC} is the DC link voltage. When the phase current is negative, the lower phase leg diode conducts. The effective voltage is zero and is independent of the switch duty-cycle. This is illustrated in Fig. 4.4, which shows that a time-varying phase A effective voltage during the phase

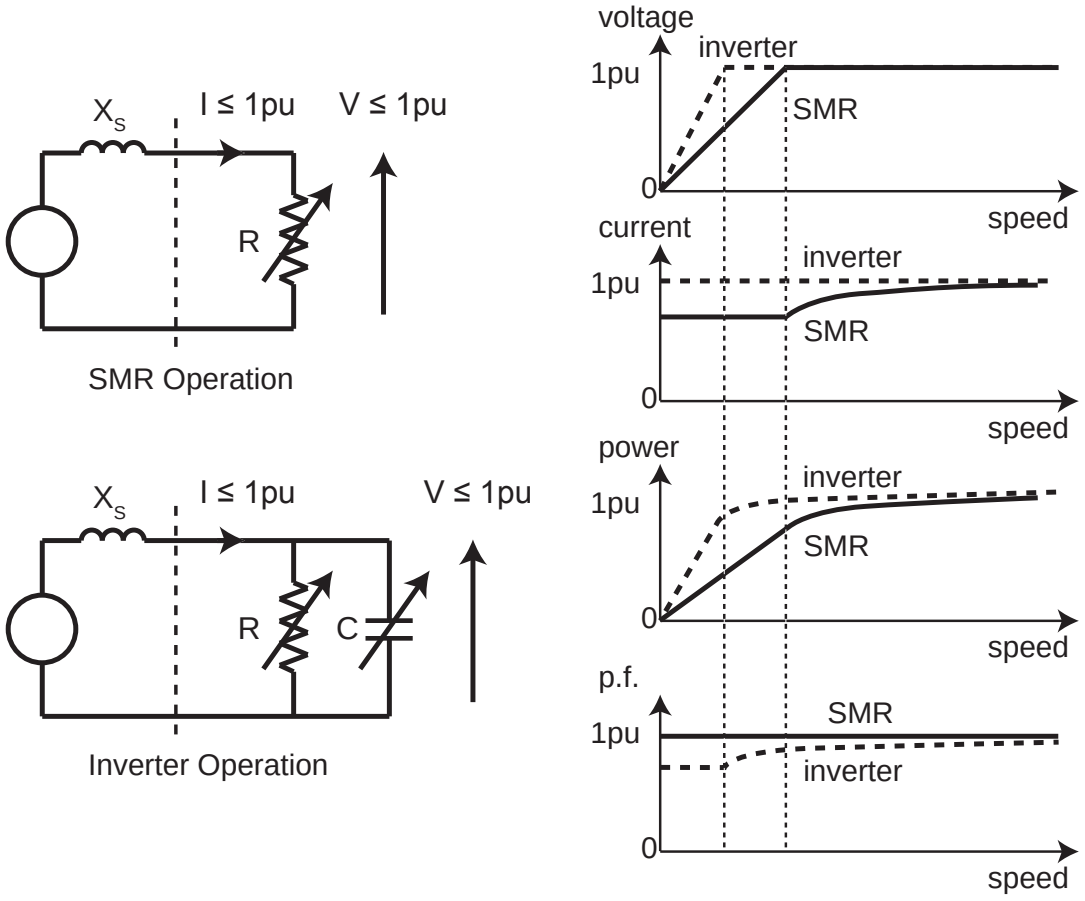

Figure 4.2: *Comparison of SMR and inverter operation: the SMR acts as a resistive load with fixed unity power factor while the inverter produces a controllable power-factor allowing it to extract more power at low speeds*

A positive current half-cycle is obtained by appropriately changing the duty-cycle. Note that for the conventional load-matching SMR operation, a constant value of duty-cycle and hence effective voltage would be used on all phases.

The proposed modulation scheme divides the positive half-cycle of the phase current waveform into three intervals - a first interval δ where V_{EFF} is set to a low value allowing the current to build up rapidly, a second interval ϵ during which V_{EFF} is set to V_{BASE} in order to achieve the normal load-matching condition and a third interval ϕ, during which V_{EFF} is increased by the amount V_{OV} in order to force the current down rapidly. These differing levels of V_{EFF} are obtained by modulating the duty-cycle of each phase-leg switch appropriately. The switching signals to each phase are identical but shifted by 120° from each other, as shown in Fig. 4.5.

Figure 4.3: *Three-phase parallel resistance and capacitance per phase used to produce the "inverter" maximum output power characteristics [16]*

The effect of the modulation scheme can be viewed as a change in the magnitude and phase of the fundamental of V_{EFF}, in a similar manner as was investigated in [40]. The presence of the δ interval at the beginning of the positive current half-cycle both increases the current amplitude and shifts the fundamental of the V_{EFF} waveform later in time, causing the phase current to lead V_{EFF}. This leading phase shift is similar to that obtained with an inverter and so the semi-bridge SMR operating under this modulation scheme thus represents an intermediate step between the single-switch SMR and the inverter which utilises six switches. The additional control flexibility offered over a single-switch SMR allows the operating power-factor to be adjusted to increase output power. However, it is expected that the maximum achievable power with this scheme will be less than that obtained with an inverter. Additionally, due to the asymmetry in the semi-bridge SMR, the phase current waveforms will be distorted.

4.3 Simulation Studies

The steady-state $d-q$ model of the interior PM alternator described in previous chapters was used to examine and contrast the performance of the interior PM machine under inverter operation with the performance under conventional single-switch SMR operation. A time-stepping dynamic model of the semi-bridge SMR modulation scheme was devel-

Figure 4.4: *Diagram illustrating modulation scheme intervals in relation to phase current and effective voltage [15]*

oped to simulate the response of the interior PM alternator over the modulation scheme parameter space in order to explore the potential output power improvement and key trends.

In all cases, the calculations were carried out for the idle speed of 1,800 rpm, using a DC link voltage of 200 V which corresponds to an effective machine AC line voltage of 156 V. The steady-state and dynamic models incorporated the effects of magnetic saturation and stator resistance.

4.3.1 Inverter Control versus Conventional SMR Control

Figure 4.6 examines the calculated operating trajectories in the $d-q$ current plane of SMR operation and inverter operation both with and without a voltage limit. The rated current limit circle and voltage limit ellipse are shown for reference. The operating curve for the inverter without a voltage limit corresponds closely to the maximum torque per ampere operating line. Without saturation this would be expected to follow a 45° slope at high currents, however the heavy saturation in this machine causes the slope to be lower. The voltage-limited inverter trajectory is shown as a bold line. This curve departs from the maximum torque per ampere trajectory when it reaches the voltage limit ellipse and is constrained to follow this ellipse at higher currents. The SMR operating curve is restricted to a smaller ellipse, associated with its unity power-factor operation.

Figure 4.5: *Relationship between phase currents, phase effective voltage and gate drive signals for the new modulation scheme (modified from [15])*

Figures 4.7, 4.8 and 4.9 show the calculated output power, phase voltage and power-factor versus current associated with the three trajectories shown in Fig. 4.6. It can be seen in Fig. 4.7 that despite the large apparent difference between the *d-q* current plane trajectories of inverter operation with and without a voltage limit, the output power versus current curves do not show significant difference until above rated current. The calculated output power with voltage-limited inverter operation at rated current (28 A) is about 6.5 kW. For the SMR the maximum power of 3.6 kW occurs at about 20 A. This is significantly less than rated current, so there is some leeway for the current to be increased in order to improve the output power.

Figure 4.8 shows that the maximum torque per ampere inverter operation produces a terminal voltage which is equal to the back-EMF voltage (≈65 V) at zero current and increases with output current. The voltage-limited inverter operation alters the *d-q*

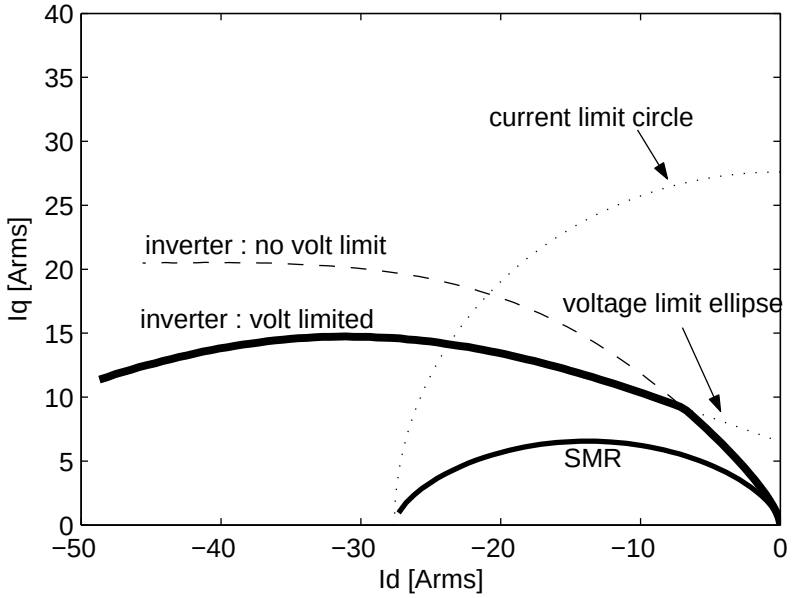

Figure 4.6: *Calculated d-q current plane operating trajectories for the SMR and the inverter with or without a voltage limit, operating at 1800 rpm with a DC link voltage of 200 V*

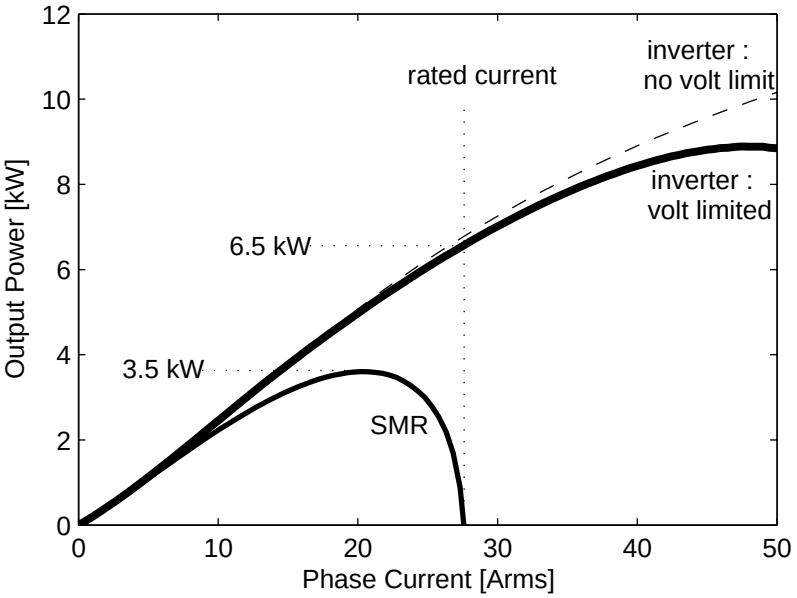

Figure 4.7: *Calculated output power versus phase current for the SMR and the inverter with and without voltage limit*

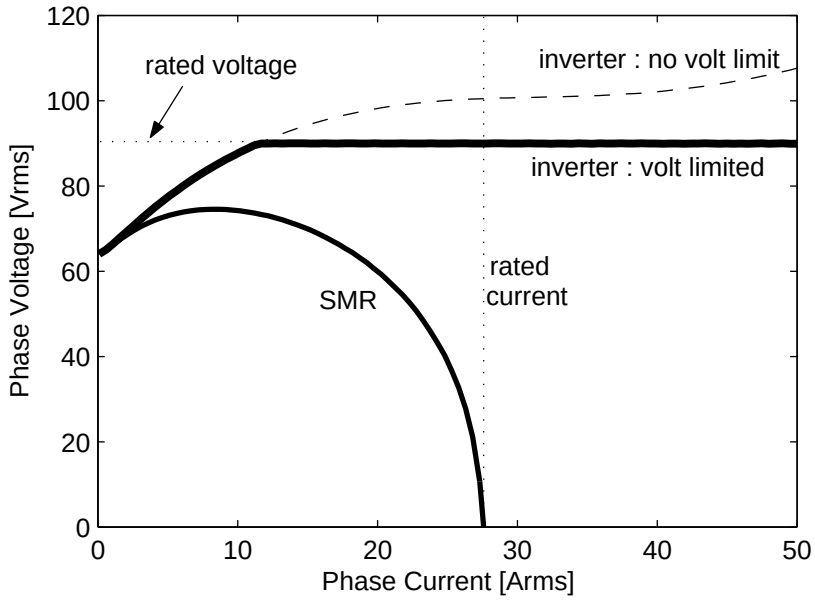

Figure 4.8: *Calculated phase voltage versus phase current for the SMR and the inverter with and without voltage limit*

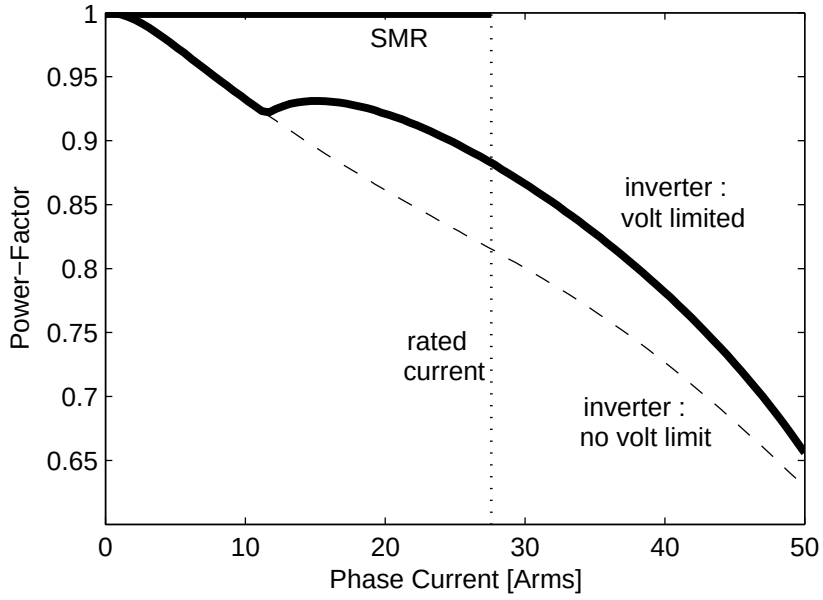

Figure 4.9: *Calculated power factor versus phase current for the SMR and the inverter with and without voltage limit*

current plane trajectory to keep this within the voltage limit. With SMR operation the generator phase voltage never reaches its rated value and falls rapidly at higher currents.

At the current corresponding to maximum power the output voltage is about 60 V, which is significantly less than rated voltage.

Figure 4.9 shows that the calculated power-factor for the SMR is unity as expected, while the inverter voltage-limited power-factor curve shows a higher power-factor than the maximum torque per ampere trajectory past the voltage limit.

The results shown in these figures are consistent with the discussion in Section 4.2.1. Given that electrical output power is proportional to the product of voltage, current and power-factor it can be seen how the inverter is able to generate more output power than the SMR at idle speed. The inverter can maintain operation at rated voltage and current, whereas with the SMR the unity power-factor restriction means that the maximum power is obtained with a voltage and current significantly below their rated values. This difference is only partially offset by the higher power-factor of the SMR.

4.3.2 SMR Modulation Strategy

The time-stepping simulation of the SMR modulation scheme was based on the interior PM machine dynamic model described in earlier chapters. The model was capable of simulating the alternator response to various parameters such as δ, ϵ and ϕ, which represent the duration of the switching intervals in the modulation scheme, as well as the effective voltage levels for each of these intervals.

In the simulation, the effective voltage was chosen to be 0 V during the δ interval, 126 V during the ϵ interval and 200 V during the ϕ interval. 126 V is the value of effective voltage which extracts maximum power from the alternator during conventional load-matching SMR operation (V_{BASE}).

Figure 4.10 shows a contour plot of the calculated rms phase current and Fig. 4.11 shows a corresponding plot of output power, obtained as the modulation control parameters δ and ϵ were varied in steps of 2°. Each point on the contour plots corresponds to operation with a particular value of δ and ϵ. There are several points of interest over the parameter space for which we will examine the current and voltage waveforms as well as the output power obtained.

The familiar case of conventional load matching can be found in the upper-left corner of the contour plot, at point C. The effective voltage waveform for this operating point is shown (solid line, not to scale) superimposed on the phase current waveform (bold line) in the upper trace of Fig. 4.12. In the lower trace the instantaneous power waveform is shown indicating the output power due to this phase (solid line) as well as the total

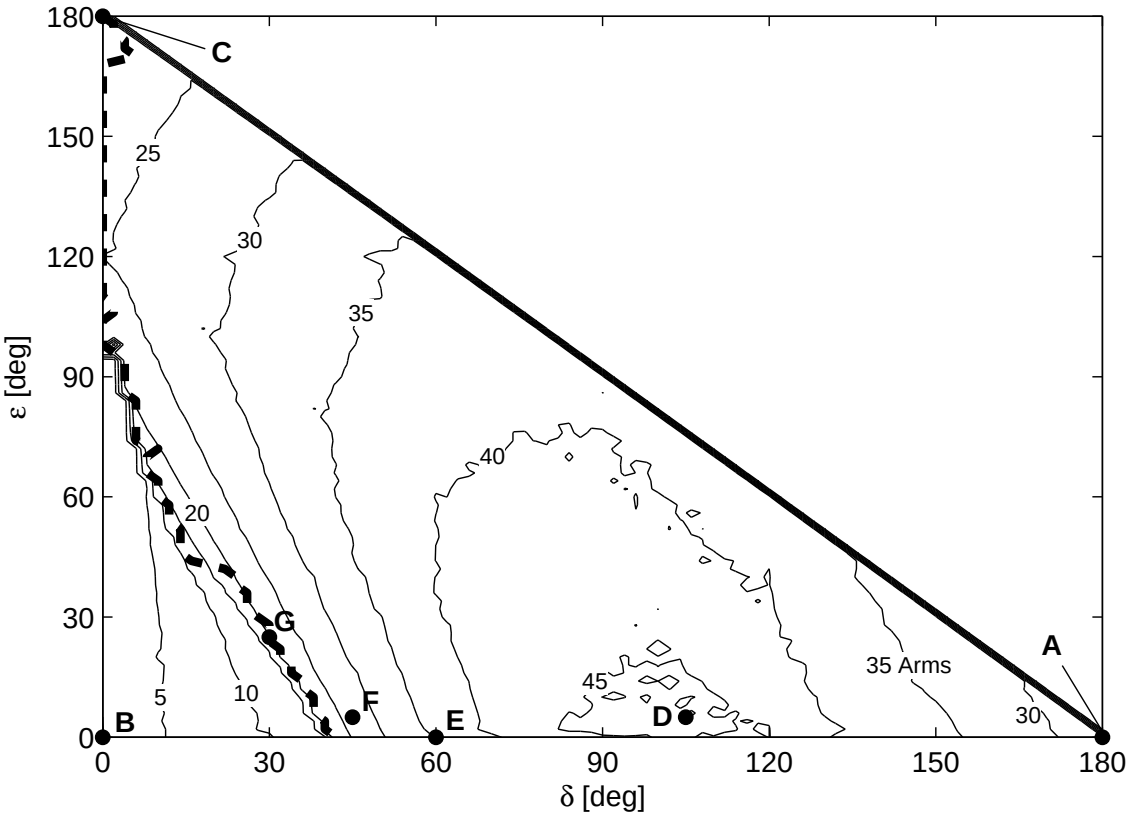

Figure 4.10: *Contour plot of calculated rms phase current versus modulation parameters δ and ϵ at 1,800 rpm, showing operating points of interest*

three-phase instantaneous output power (dashed line). With a constant load-matching V_{EFF} of 126 V, the phase current of 20 A is sinusoidal and the total instantaneous output power is relatively smooth and has an average value of 3.5 kW.

Operating point A corresponds to the short-circuit case where the δ interval takes up the entire period ($V_{EFF} = 0$ V). The phase current is equal to the short-circuit current of 27 A and the output power is zero (see Fig. 4.13).

Moving to the origin, point B corresponds to the open-circuit case, where $V_{EFF} =$ 200 V. This is greater than the back-EMF voltage at this speed, hence no current flows and the power is again zero.

Assuming a symmetrical current waveform, $\delta + \epsilon = 180°$, hence it is not possible to operate in the upper-right half of the contour plots of Figures 4.10 and 4.11. The operating points A, B and C which mark the three corners of the usable parameter space represent conventional modes of operation. By varying the modulation parameters within

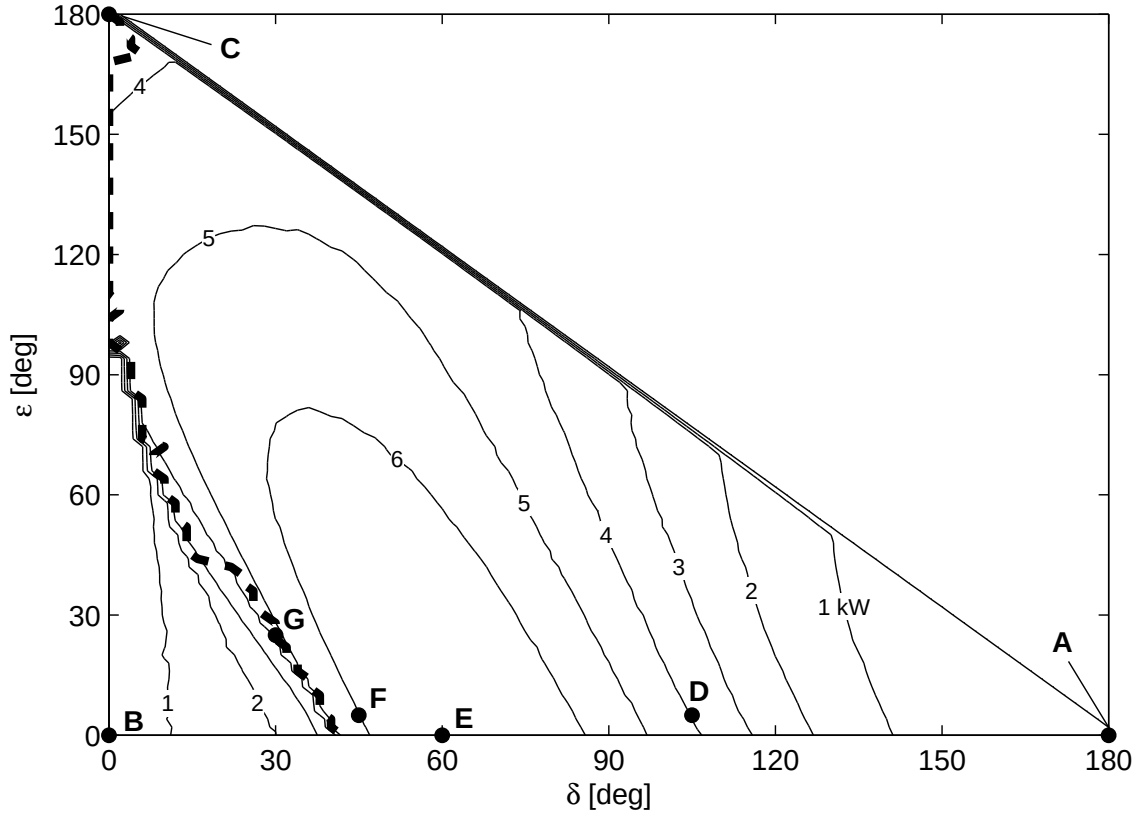

Figure 4.11: *Contour plot of calculated average output power (kW) versus modulation parameters δ and ϵ at 1,800 rpm*

this space, it is possible to increase both the phase current and the output power. For instance, the maximum value of phase current obtained is 46 A, at operating point D (see Fig. 4.14). It can be seen that the current waveform has become less sinusoidal and the instantaneous output power is highly discontinuous, with an average value of 4 kW.

The current obtained at point D greatly exceeds the 27 A rating of the alternator and would involve excessive heat dissipation, with the associated increased risk of demagnetisation. Of perhaps more practical interest is the maximum power point, at E. The output power obtained approaches 7 kW, achieved by keeping the effective voltage at zero to build the current up and then using maximum bus voltage to extract as much power as possible. The time domain waveforms corresponding to this case are shown in Fig. 4.15, where a large ripple content can be observed in the instantaneous power waveform. The current is approximately 37 A, which is still significantly greater than rated current. There is an interesting similarity between this type of control and that used for

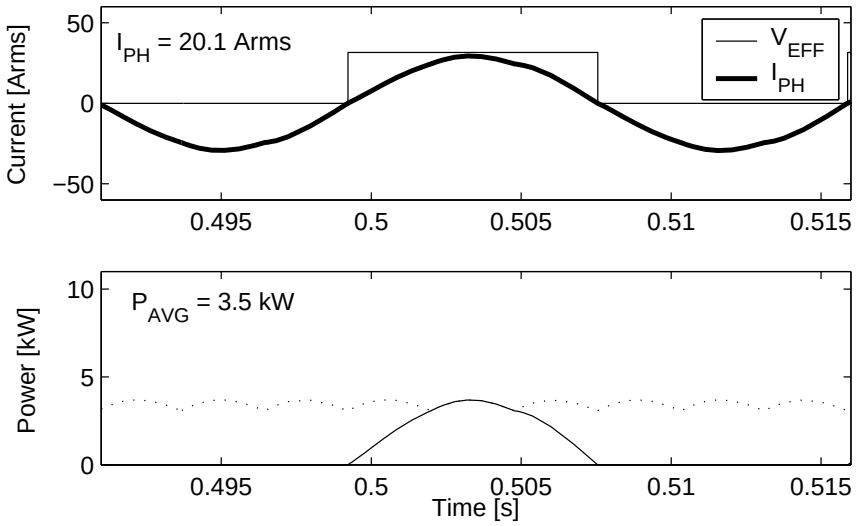

Figure 4.12: *Conventional SMR 'load-matching' operation at point C ($\delta = 0°$, $\epsilon = 180°$)*

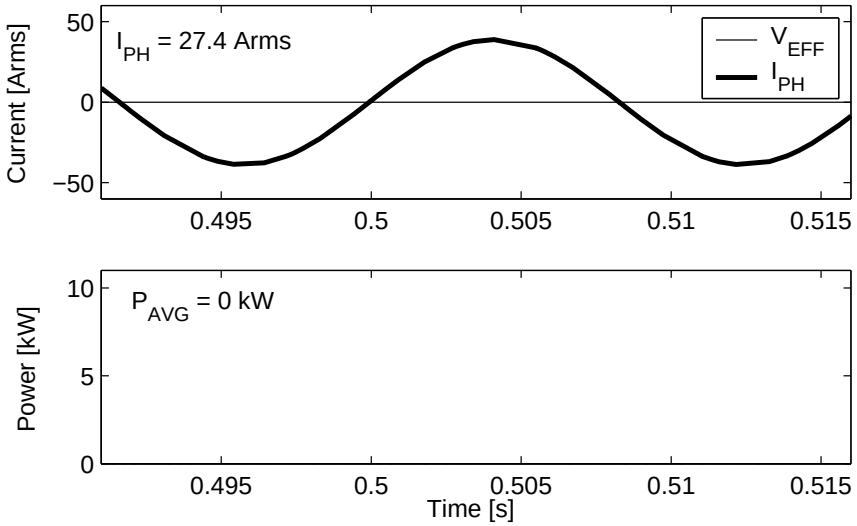

Figure 4.13: *Short-circuit operation at point A ($\delta = 180°$, $\epsilon = 0°$)*

switched-reluctance machines and brushless DC machines at high speed.

The maximum power obtainable without exceeding rated current is 5.9 kW, which can be found at point F (see Fig. 4.16). Note that in spite of the varying effective voltage used to boost the current amplitude, the shape of the positive half-cycle of the waveform is close to sinusoidal, indicating that the energy is still concentrated in the fundamental.

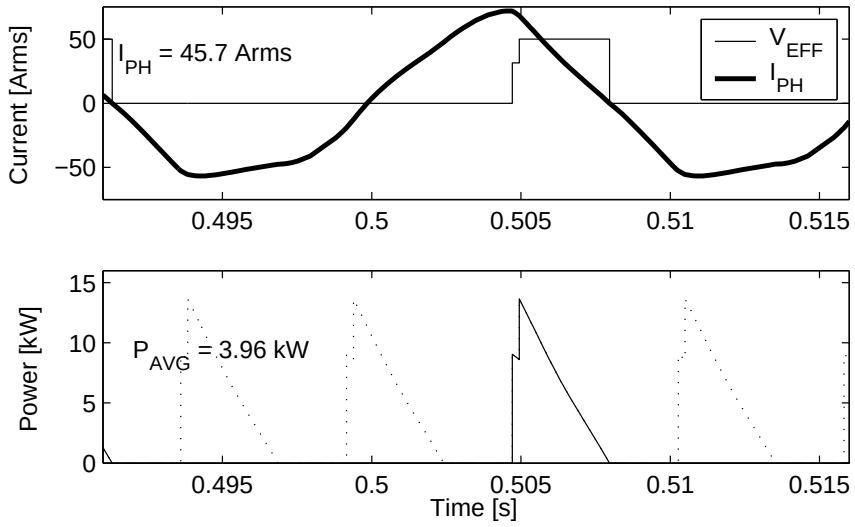

Figure 4.14: *Maximum phase current obtained at point D ($\delta = 105°$, $\epsilon = 5°$)*

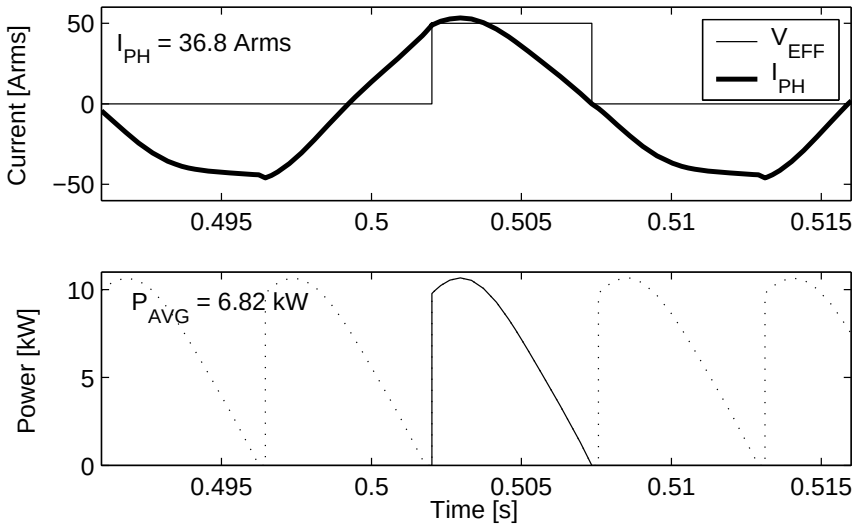

Figure 4.15: *Maximum power obtained at point E ($\delta = 60°$, $\epsilon = 0°$)*

4.3.3 Optimal Operating Regions

Figure 4.18 shows a scatter plot of the simulation results illustrating the relationship between output power and rms machine phase current. For reference, the calculated allowable power versus current loci are shown for both a conventional SMR and an inverter (from Fig. 4.7). This figure clearly shows that the modulation scheme allows much more flexibility in the choice of operating points than the conventional SMR control scheme and

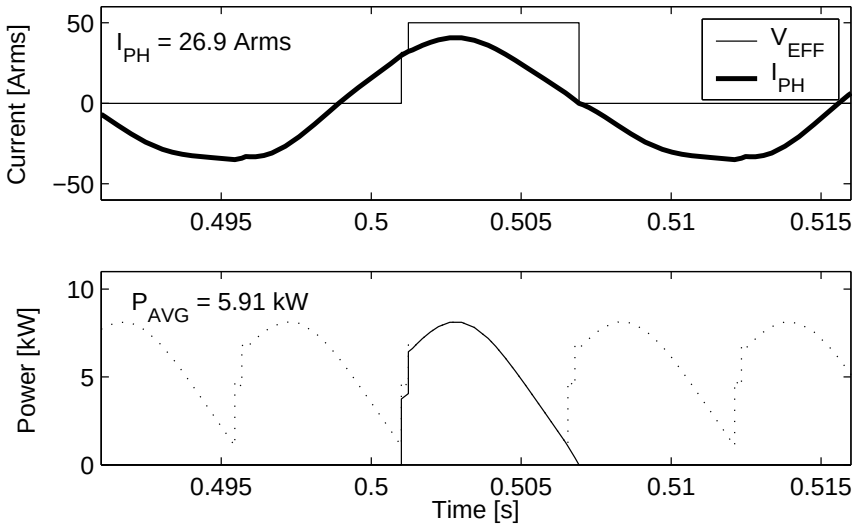

Figure 4.16: *Maximum power obtained with rated current at point F ($\delta = 45°$, $\epsilon = 5°$)*

permits higher output powers to be achieved. The modulation scheme provides better performance than a load-matching SMR but not as good performance as an inverter, with the output power tapering off at higher currents.

It can also be seen that for a particular value of current, there is an operating point which offers the highest output power. This locus of maximum output power for a given phase current is marked as a bold dashed line on Figures 4.10 and 4.11 and represents the optimal operating points, starting from the load-matching condition at point C and ending at the maximum power point at E. For instance, Fig. 4.18 indicates that even without increasing the phase current from the load-matching condition at point C, more than a kilowatt of extra power can be obtained by operating at point G.

For each of the simulated operating points in the delta-epsilon plane, the equivalent values of I_d and I_q can be calculated from the simulation. Figure 4.17 shows a scatter plot of the operating points achieved using the modulation scheme represented in the $d-q$ current plane. For reference the inverter and SMR trajectories calculated earlier in Fig. 4.6 are shown. The scatter plot shows a "cloud" of the feasible operating points which are anchored by three points on the SMR operating trajectory : short-circuit (A), open-circuit (B) and optimal load matching (C). The feasible operating points form an elliptical locus not unlike the voltage ellipse but significantly smaller. Despite this apparently significant difference in $d-q$ trajectories, the maximum output power for a given value of current is similar between the inverter and the new SMR modulation scheme, at least up to rated

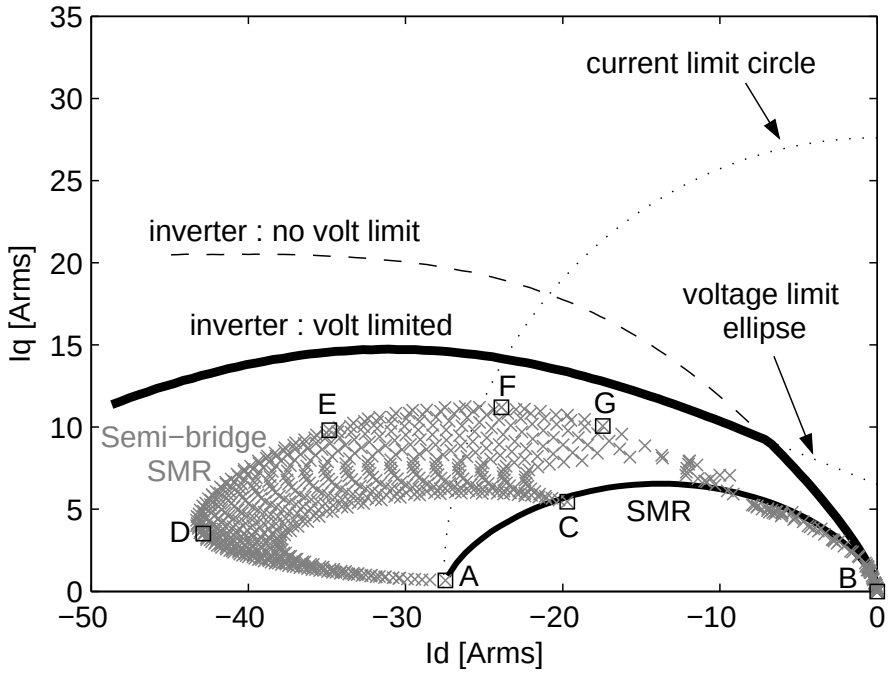

Figure 4.17: *Scatter plot of calculated feasible d-q currents available using the proposed SMR modulation scheme at 1,800 rpm, with key operating points indicated. Inverter and SMR operating trajectories are shown for reference.*

current.

4.4 Experimental Setup

Experimental results were obtained using the dynamometer test rig set up as shown in Fig. 4.19. The output of the interior PM alternator was fed through the semi-bridge SMR into a 200 V DC voltage source load simulator consisting of a DC power supply, protective diode and a resistive load bank. This arrangement maintains a constant DC link voltage despite variations in the output current of the SMR, up to a maximum current equal to the DC link voltage divided by the load resistance.

The modulation scheme was implemented on a *Microchip dsPIC30F10* 16-bit microcontroller. Hall-effect current sensors present on each phase of the SMR provided phase current signals to the modulation controller and the appropriate switching signals were determined based on the modulation parameters. These were 5 kHz pulse-width-modulated (PWM) signals which in turn controlled the lower phase-leg switches of the SMR.

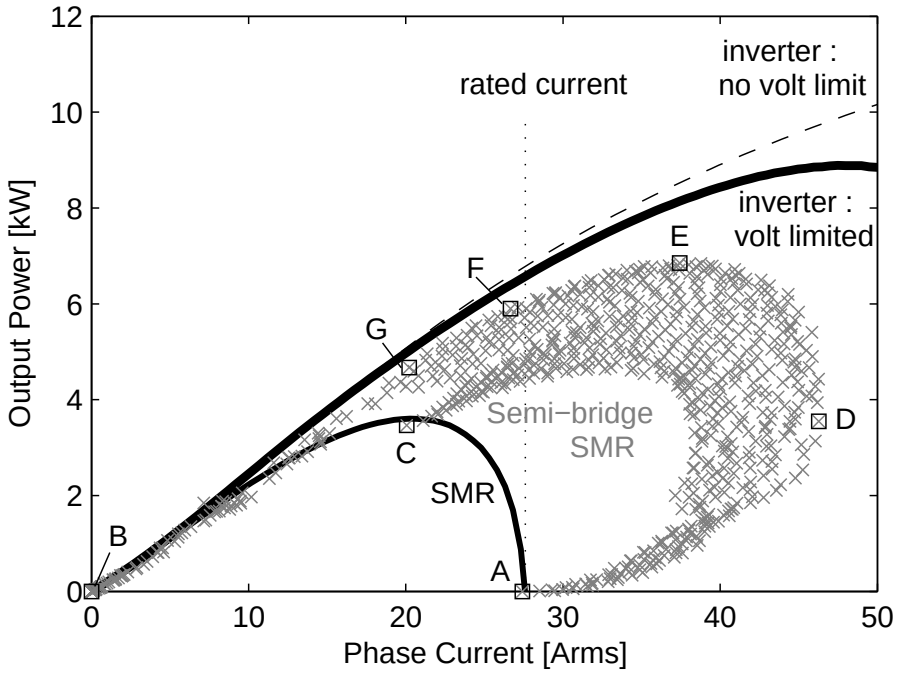

Figure 4.18: *Scatter plot of calculated output power versus phase current at 1,800 rpm with key operating points indicated. The calculated performance with a SMR and a voltage-limited inverter is shown for reference.*

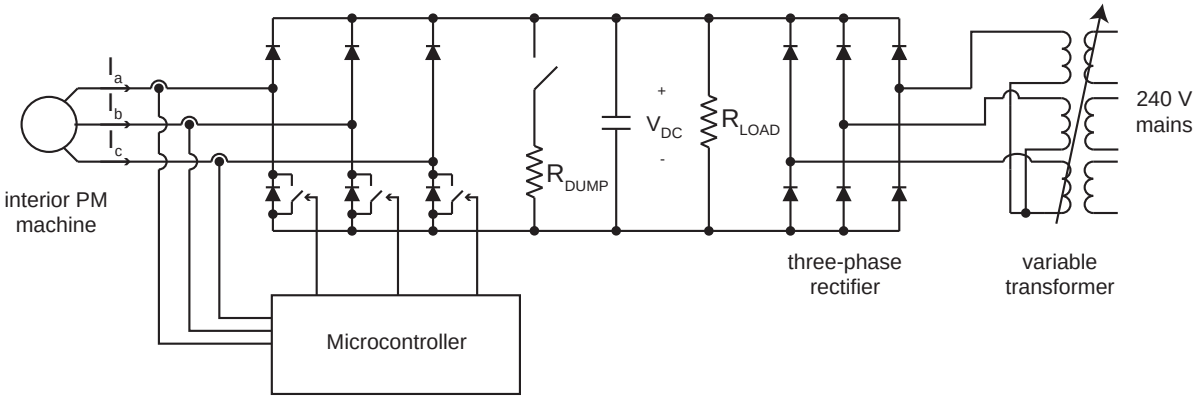

Figure 4.19: *Experimental configuration for low-speed power improvement testing*

In the experimental tests, the current sensors were only used for detecting the zero crossings of the phase currents. This timing information can also be obtained using inexpensive phase-to-ground voltage sensors, thus eliminating the need for current sensors [15] and it is expected that the implementation of the proposed modulation scheme in this

way should result in only a small incremental cost over the conventional load matching control.

The outputs from the current sensors were passed through op-amp Schmitt triggers in order to obtain suitable digital signals. The edge transition of the waveform from a low to a high level was used to trigger a micro-controller interrupt which executed the code for the modulation scheme. The modulation controller was programmed to offer real-time menu-based adjustment of the modulation parameters δ and ϵ via a digital opto-interrupter control knob and buttons. The values of the modulation parameters were displayed on a Liquid Crystal Display (LCD) module.

Appropriately placed meters were used to record the machine phase currents and line voltages, as well as the current sensor outputs and the DC output current, I_{OUT} delivered to the load. The gate driver signal to one of the phase-leg switches was low-pass filtered and inverted to provide an approximate representation of the effective voltage waveform V_{EFF}.

During tests, when the alternator was brought up from standstill to 1,800 rpm, the modulation controller was kept at the conventional load-matching setting (point C in Fig. 4.10). It was initially planned to incrementally adjust the modulation parameter values via the control interface until the desired operating point was obtained. Although it was found that the modulation controller parameters could be dynamically adjusted, one of the issues encountered was that when the operating point was moved too far from the load-matching point, the dynamometer rig produced significant torque vibrations and oscillations in speed. Similar behaviour was also observed when an operating point was attempted after bringing the alternator up to 1,800 rpm in short-circuit operation.

The modulation controller was then reprogrammed to allow for an instantaneous switch between load-matching operation and the phase advance modulation scheme. It was found that switching directly from load-matching to the desired operating point caused no noticable problems with vibration. Once the operating point was achieved, the parameter values could be adjusted to some degree around that point without causing oscillations.

As the operating point shifts within the parameter space the alternator reaction torque changes. The poor mechanical stiffness of the dynamometer rig allowed the operating speed to fluctuate slightly with such changes. This, coupled with the fact that the modulation controller bases its timing off the zero-crossings of the phase current waveform, is one possible cause of the observed oscillations.

4.5 Experimental Results

The DC output power and the phase a current and effective voltage waveforms were recorded at several operating points. As a reference point, Fig. 4.20 shows these waveforms during conventional SMR load-matching operation (point C), where a constant effective voltage of 126 V is applied. Note that the measured phase current of 17.6 A and output power of 2.84 kW are lower than the model calculated values of 20 A and 3.5 kW respectively. This represents a 20% difference between predicted and measured output power, which is consistent with earlier measurements for the same operating point using a single-switch SMR (see Section 3.5.3).

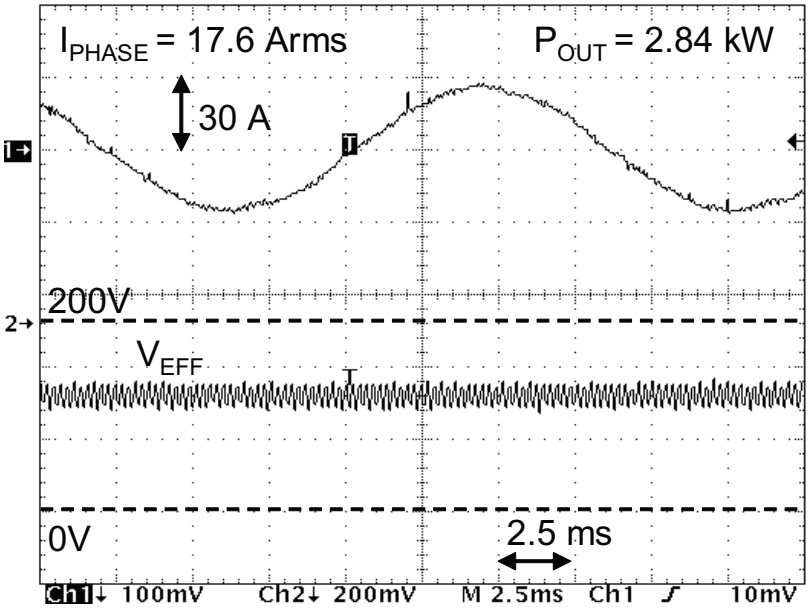

Figure 4.20: *Measured phase current (upper trace) and effective voltage (filtered and inverted gate drive signal) (lower trace) for 1,800 rpm generation into a 200 V load while operating in load-matching at point C ($\delta = 0°$, $\epsilon = 180°$)*

Figure 4.21 shows the waveforms while operating at the calculated maximum output power within rated current operating point (point F). An unfiltered effective voltage waveform is shown in this case to allow the modulation interval transitions to be seen more clearly. In comparison with the corresponding predicted waveforms of Fig. 4.16, it can be seen that when 200 V is applied during the ϕ period near the end of the positive current half-cycle, the measured current falls to zero more rapidly than the simulation predicts, resulting in a zero-current plateau at the end of the positive half-cycle. The phase current waveform thus deviates significantly from the calculated shape and has

a reduced rms value of 21.8 A as opposed the rated current of 27 A predicted at this operating point.

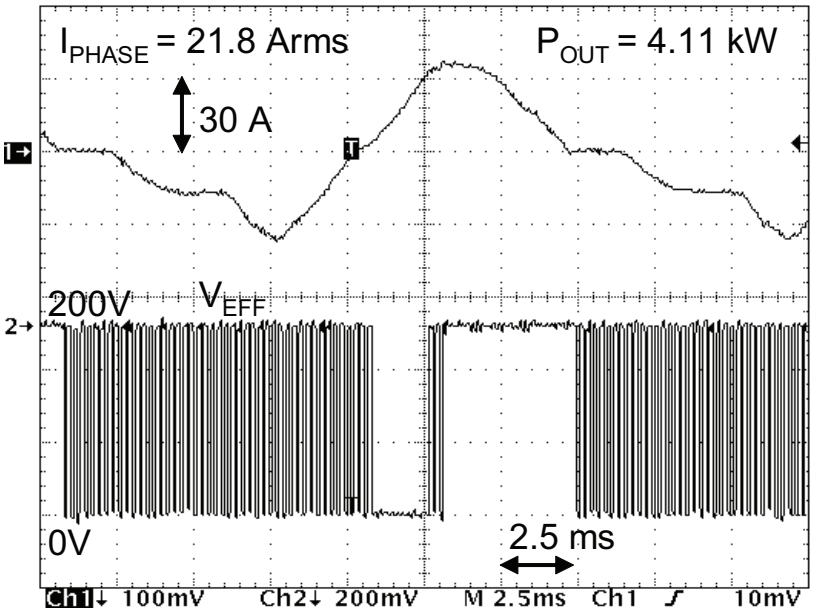

Figure 4.21: *Measured phase current (upper trace) and effective voltage (inverted gate drive signal) (lower trace) for 1,800 rpm generation into a 200 V load while operating at point F ($\delta = 45°$, $\epsilon = 5°$)*

Although the reasons for the discrepancy between measurements and predictions remains unknown, it was decided to adjusted the modulation scheme in order to achieve a more sinusoidal current waveform at the maximum-power operating point. To reduce the falling rate of curent during the ϕ phase, the effective voltage level V_δ applied was reduced from 200 V and symmetrically, the voltage level V_ϕ applied during the δ interval was also increased from 0 V. Several voltage levels were investigated and values of $V_\delta = 40$ V and $V_\phi = 160$ V were found to produce more sinusoidal currents, less torque vibration and higher output power. These values were used for all subsequent testing.

Figure 4.22 shows the measured performance with the new values of effective voltage, for the same operating point (point F). The current waveform now shows a good match with the predicted shape and rms value shown in Fig. 4.16, and the output power obtained is 4.73 kW. This is 20% lower than the predicted 5.9 kW, thus showing a reduced output power consistent with that found in the conventional load-matching case. The result nevertheless represents a substantial 66% increase in idle-speed power over the measured SMR case without exceeding the machine's rated current. This also means that the

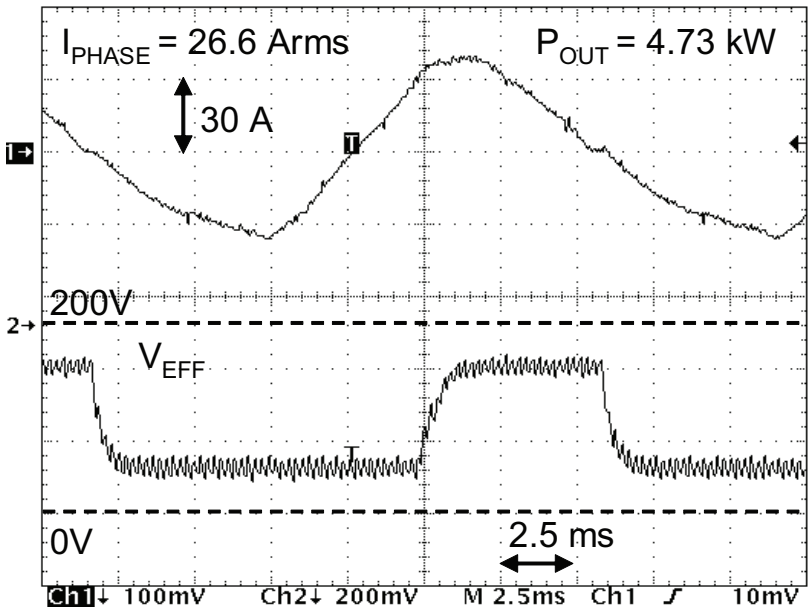

Figure 4.22: *Operation at point F, as in Fig. 4.21, except with voltage levels of V_δ = 40 V and V_ϕ = 160 V*

alternator operating with a SMR can meet the high power alternator specification of 4 kW at idle speed.

4.6 Summary of Findings

The findings of this chapter can be summarised as follows:

- Under conventional load-matching control, SMRs are limited to unity power-factor operation;
- The ability of inverters to control their input power-factor allows them at low speeds to extract about twice the output power from PM generators compared with conventional SMR control;
- The proposed modulation scheme in which the effective voltage applied to the alternator is changed in a step-wise fashion allows the SMR to generate a leading power factor and thus obtain better performance at low speeds than with SMR load-matching;

- Careful selection of the modulation control parameters is required to optimize the output power performance without exceeding rated current;
- Simulation results predicted that the calculated output power with a SMR at the alternator idle speed of 1,800 rpm can be increased from 3.5 kW with conventional SMR control, to 5.7 kW with the proposed control scheme, in comparison to the calculated value of 6.5 kW with an inverter; and
- Experimental results showed a measured output power increase from 2.84 kW with conventional SMR control to 4.73 kW with the proposed control scheme, which meets the 4 kW high power alternator specification

This section has demonstrated that the proposed modulation scheme can produce substantial low-speed output power improvements with the interior PM alternator studied. Future work may include a more extensive examination of experimental results at various operating points and further investigation to better understand the discrepancies between the calculated and measured current waveforms.

Chapter 5

Conclusions

5.1 Background

The next generation of consumer vehicles is slated to include new features to enhance performance, safety and comfort. Some examples of these features include active electromagnetic suspension to smooth out bumps and jolts, or electromechanical engine valve timing to run the engine efficiently at all speeds. These emerging features, together with the electrification of traditionally mechanically-driven accessories, come at the cost of greater electrical power consumption, so it must be ensured that the alternator acting as the power supply of a car is also prepared for the next generation.

The electrical power demand in cars has risen steadily from around 1 kW in 1985 to almost 2.5 kW in 2005 and continues to grow [6, 8]. The conventional Lundell alternator presently used in vehicles typically achieves an output power of 1 to 2 kW and would be hard-pressed to satisfy future power requirements, so there is clear motivation for the development of higher power alternators is clear. Towards this effort, the MIT/Industry Consortium on Advanced Automotive Electrical/Electronic Components and Systems [4] has provided several recommendations. Briefly, a suitable high power alternator should provide:

- More power - output power ranging from 4 kW at engine idle speed (600 rpm) to 6 kW at top speed (6,000 rpm), corresponding approximately to a constant power speed range of 10:1

- Better efficiency - requirement of 75% efficiency at 75% load at 1,500 rpm

- Higher and steadier output voltage - maintain strict voltage limits around a 42 V output voltage as specified by the 42V Powernet specification

Ideally, an alternator should also be inexpensive, robust and require minimal maintenance.

Most significant of the Consortium's recommendations is the move from the present 14 V electrical rail to a 42 V system. The higher system voltage allows the use of a lower current to deliver the necessary power to car loads, resulting in a nine-fold reduction in copper losses alone. This improved efficiency is especially important at higher power levels. The higher system voltage also necessitates stricter voltage regulation to ensure safety and this has been formalised in the SAE/MIT 42V Powernet standard [6].

Practical high power alternator solutions are currently being pursued, with efforts involving electrical machines of various types, e.g. induction machines, permanent magnet (PM) machines and reluctance machines. The greatest challenge in many cases has been to maintain the required output power across the wide operating speed range. A second key concern is the power electronics used to rectify and regulate the output power, as the cost of power electronics is one of the most significant factors in determining the cost of the alternator system as a whole.

5.2 Original Contributions

This thesis has investigated the power generation and control characteristics of a concept-demonstrator interior PM alternator intended to satisfy the recommendations for a high power alternator. The alternator was based on a 6 kW interior PM machine specifically designed for optimal field-weakening performance and therefore a very wide CPSR. The machine also has a high back-EMF and high inductance, allowing it to act as a controllable current source when operating in conjunction with a SMR.

In this interior PM machine application, the SMR was used to provide voltage rectification and regulation of voltage transients, to perform load-matching to maximise power transfer to alternator loads and to increase the output power obtained at low speeds. The SMR is a much cheaper alternative to an inverter while still allowing more flexibility of control and greater output power than the bridge rectifier used in conventional Lundell alternators.

The original contributions of this work in investigating the generation and control characteristics of the interior PM alternator and SMR are summarised below:

- Introduction of the VI locus as a tool in the steady-state modelling of electrical machines.
- Development of steady-state and dynamic models to analyse the performance of the interior PM machine operating in UCG, capable of predicting the effects of saliency, magnetic saturation and stator resistance on generation and in particular hysteresis in the output current. Experimental validation of the model predictions.
- Experimental demonstration of hysteresis in interior PM machines, which has not previously been demonstrated, in accordance with model predictions.
- Investigation and modelling of SMR-based control of the interior PM machine output. Experimental demonstration of alternator output power maximisation through load-matching and closed-loop voltage regulation and transient suppression using the SMR.
- Dynamic modelling of a phase-advance modulation scheme to improve the output power of the interior PM alternator at idle speed. Implementation of the phase-advance modulation scheme on a microcontroller, obtaining a measured increase in idle-speed output power of 67%.

These contributions and other findings are further elaborated in the following subsections.

5.3 Interior PM Machine Generation Characteristics

In order to utilise the specially-designed interior PM machine [16] as an alternator, its operating characteristics were theoretically and experimentally investigated. In particular, the case of interior PM generation into a DC voltage source load, also known as UCG was studied as this is analogous to a car alternator charging a battery. The effects of various parameters such as stator resistance, saliency and magnetic saturation on its generation characteristics were examined, as well as the interesting phenomenon of hysteresis occurring in the stator current versus speed characteristic.

Voltage-Current Loci

- The concept of the VI locus of an interior PM machine was introduced as an analytical tool, which to the author's knowledge has not previously been applied

to interior PM machines. VI loci are a visualisation of the relationship between the steady-state output voltage and stator current of a PM machine while generating into a three-phase resistive load. They have been used throughout this thesis to illustrate the generating behaviour of the interior PM machine under various conditions.

Effect of Machine Parameters on Generation

- A steady-state *d-q* model of the interior PM machine was used to produce calculated VI loci in order to investigate the effects of various parameters such as saliency, stator resistance and magnetic saturation on the output current of two interior PM machines. These predictions were validated against experimental results including measurements of hysteresis, which have not previously been demonstrated.
- Voltage overshoot and hence hysteresis only occurs for machines with a saliency ratio of greater than two. Neglecting non-ideal effects, the size of the voltage overshoot is proportional to the machine saliency and independent of speed.
- The presence of magnetic saturation and stator resistance both act to reduce voltage overshoot. Additionally, the effect of resistance is more pronounced at low speeds where the machine reactances are comparatively small and the resistance therefore dominates the machine impedance.

Equivalent Circuit Models

- The validity of three equivalent circuit models of UCG were evaluated by comparing calculated curves against experimental results obtained using each of the configurations. The VI loci experimentally measured from a rectifier and resistive load accurately predicted the stator current versus speed characteristic measured with a rectifier and DC voltage source load, therefore the modelling of a DC voltage source load as a resistive load can be considered valid.
- The modelling of a rectifier and resistive load by a three-phase resistive load was found to be not entirely valid, producing an overestimation of voltage overshoot in the VI loci. It follows that this inaccuracy likewise affects the predictions for a rectifier and voltage source load (UCG). It is possible that the action of the rectifier causes currents in the portion of the locus which is typically close to the threshold of generation to become highly discontinuous,

thereby violating the assumption of sinusoidal current waveforms upon which the steady-state model is based.

- The dynamic model used was shown to accurately predict the shape of the current and voltage waveforms of the interior PM machine during UCG, even under highly discontinuous currents. This causes it to be more accurate than the steady-state model in predicting the waveforms near the threshold of generation and therefore the amount of hysteresis that may be observed in a machine.

Stator Current Hysteresis

- VI loci were used to explain the phenomenon of hysteresis in the UCG stator current versus speed characteristic. Hysteresis was shown to arise from 'voltage overshoot', which is a characteristic observable in the VI locus of a machine whereby the machine is capable of producing an output voltage under load which is greater than the open-circuit voltage.
- Stator current hysteresis has not had an impact on the generation performance of the interior PM machine used in this study because the desired operating DC link voltage was too low for hysteresis to manifest. The methods used in this study can be applied to predict the presence and extent of hysteresis in other cases where it may be an issue in the control of an interior PM alternator.

5.4 Switched-Mode Rectifier Control

Whereas the output of a conventional Lundell alternator is controlled by adjusting the field current, the output of the interior PM alternator is controlled by the SMR. The SMR provides the functions of voltage regulation and transient suppression and is thus the means by which the alternator can satisfy the voltage requirements outlined in the 42V Powernet specification.

Both the steady-state and dynamic characteristics of the alternator and SMR system were theoretically and experimentally investigated, first as an open-loop system and later as a closed-loop system after a suitable closed-loop controller had been designed and implemented.

In all tests involving the SMR, the interior PM alternator was fitted with a 135 V stator in order to accommodate the available SMR unit rated for 200 V, 50 A. The DC

link voltage was set at 200 V and thus for a desired output power of 6 kW, the alternator DC output current was 35 A. To achieve a true 42 V system in accordance with the 42V Powernet specification, the alternator would need to be fitted with a lower voltage stator, however the SMR would then need to be rated for at least 150 A. The results obtained in these tests can nevertheless be considered indicative of the alternator's performance.

Alternator SMR Duty-Cycle Response

- Control of the SMR was achieved by adjusting the duty-cycle of PWM signals fed to the gates of the SMR switches. Varying the duty-cycle has different effects depending on the operating speed of the alternator:
- At low speeds where the open-circuit back-EMF of the alternator is insufficient to overcome the DC link voltage, the SMR acts similarly to a boost converter - instead of being exposed to the full DC link voltage V_{DC}, the alternator sees a reduced effective voltage $V_{EFF} = (1 - d)V_{DC}$, determined by the SMR duty-cycle d. For a fixed DC link voltage such as a car battery, this lowers the minimum operating speed at which the alternator starts to generate current. The appropriate adjustment of the duty-cycle to match the alternator to the load in this manner resulted in a smooth increase in output power from standstill up to approximately 3,000 rpm, above which no boosting action is necessary (see Fig. 3.21).
- At high speeds, changing the effective voltage has little effect on the alternator output current and the alternator provides a nearly constant current I_{IN} to the SMR. Varying the duty-cycle controls the portion of current $I_{OUT} = (1-d)I_{IN}$ which is delivered to the load. This is a key point in the control of the interior PM alternator and was supported by the relatively constant predicted input current vs. duty-cycle (I_{IN} vs. d) characteristic. These relationships were experimentally verified and it was found that the non-linear region around the threshold of generation appeared at higher than predicted values of duty-cycle and thus the current versus duty-cycle relationship was less linear than expected (see Fig. 3.17). This resulted in the measured alternator currents being lower than predicted by a few amps. These discrepancies can be attributed to the previously mentioned inaccuracy of the steady-state model when handling non-sinusoidal waveforms.

Power and Efficiency

- The power requirements for a high power alternator correspond to 4 kW at engine idle speed (1,800 rpm) and 6 kW at top speed (18,000 rpm). Since the dynamometer rig used to take experimental measurements was limited to 6,000 rpm, it was not possible to measure the top-speed result, however, the output power obtained at 6,000 rpm was 6.6 kW. Given the design of the interior PM alternator for optimum field-weakening performance, it is reasonable to expect that the high-speed requirement is achievable (see Fig. 3.21).
- The predicted alternator output power at idle speed was 3.5 kW, which does not satisfy the idle-speed power requirement of 4 kW. The actual measured power was 18% lower, at 2.84 kW. This is also reflected in the lower than expected output current of 14.7 A as compared with a predicted 17.5 A.
- The efficiency requirement from the 42V specification was 75% efficiency at 75% load at an engine speed of 1,500 rpm. This corresponds to a load of 4 kW at an alternator speed of 4,500 rpm. The efficiency of the interior PM alternator at this point is 71%.

Closed-Loop Control

- The transient current response of the alternator and SMR system was experimentally determined by injecting sinusoidally-varying SMR control signals and the resulting response was modelled by a second-order transfer function. A simple closed-loop controller with proportional gain was designed and implemented based on the modelled system function.
- The closed-loop controller was successful in regulating the output voltage to 200 V DC while the alternator was operating at 1,500 rpm. Measurements showed a 1% decrease in average output voltage for a 25% increase in load current, i.e. a ± 2% variation in average output voltage over the entire load range. Some steady-state output voltage oscillations were present under higher current loads. These oscillations were limited to within the 190 V to 210 V range, i.e ± 10% output voltage. The nominal operating voltage from the 42V Powernet specification is 42 V, with an allowable steady-state variation from 30 V to 50 V. This is roughly equivalent to a range of ± 19% nominal voltage, which the controller easily satisfies.
- The ability of the controller and SMR to suppress transient overvoltages was successfully demonstrated through load dump tests. The maximum overvoltage

produced by the closed-loop system in response to a load current step of 8.8 A (representing an 880 W load dump) was 10 V. The load dump transient reached a peak value of 110% nominal output voltage and settled to steady-state value within 20 ms. As a comparison, the 42V specification of 58 V is equivalent to 138% nominal voltage.

Output Power Improvement

- The output power achieved by the interior PM alternator operating with the SMR at idle speed (1,800 rpm) was 2.8 kW, which does not satisfy the high power alternator requirement of 4 kW. In order to address this issue of insufficient idle-speed power, a SMR modulation scheme employed by Rivas, Perreault and Keim to improve output power in a Lundell alternator was examined [15]. This modulation scheme has previously been shown to improve idle-speed power output by up to 15%.
- To better understand the limitations of the SMR, the operating trajectories of the alternator under both SMR load-matching and inverter operation were examined using analytical models. The ability of inverters to generate a leading input power-factor allows them to extract twice the output power at low speeds as compared with SMR load-matching. By applying a varying effective DC link voltage to each phase over the electrical period of the alternator, the proposed SMR modulation scheme allows the current waveform to be shaped. This can be used to generate a certain degree of leading phase shift in the fundamental of the modulated waveform.
- A Simulink model was constructed to predict the performance of the scheme as applied to the interior PM alternator. Simulations showed that at idle speed and rated current it would be able to offer performance lying between that of SMR load-matching and inverter operation, providing an approximately 70% increase in output power over SMR load-matching performance.
- The modulation scheme was implemented on a dsPIC microcontroller. The controller was programmed to allow the modulation parameters to be adjusted in real time during alternator operation. Experimental tests conducted over a range of modulation parameter values showed a 67% increase in idle-speed output power from 2.84 kW with SMR load-matching to 4.73 kW with the

SMR modulation scheme, thereby satisfying the idle-speed power requirement of 4 kW.

5.5 Summary

The aim of this study was to examine the operation of an interior PM machine with a switched-mode rectifier as a high power alternator.

The implementation of basic closed-loop voltage regulation as well as a SMR modulation technique to improve low-speed output power have demonstrated that the concept demonstrator interior PM alternator is capable of satisfying the voltage and low-speed power requirements of the SAE/MIT 42V specification using inexpensive power electronics and simple control.

Additionally, in examining the interior PM machine generation characteristics, steady-state and dynamic models have been developed to investigate the effect of various parameters such as saliency, stator resistance, magnetic saturation, DC link voltage and operating speed on the generating performance of the alternator. These provide a framework for understanding and predicting alternator performance.

The performance of the interior PM alternator against the high power alternator specifications are summarised as follows:

- The alternator achieved an output power of 4.73 kW at 1,800 rpm and 6.8 kW at 6,000 rpm which satisfies, over the tested speed range, the specified 4 kW at 1,800 rpm and 6 kW at 18,000 rpm (see Fig. 5.1)
- The efficiency measured at 1,500 rpm under 75% load was 71%, which does not satisfy the specified efficiency of 75%
- The measured steady-state output voltage variation was ± 10% nominal voltage, satisfying the specification of ± 19% nominal voltage
- The maximum transient voltage peak measured under load dump conditions was 110% nominal voltage, satisfying the specification of 138% nominal voltage

The wide constant-power speed range of the interior PM alternator in this study also makes it suitable for renewable energy applications. The SMR provides a useful degree of control in order to dynamically optimise the power transfer to a battery, particularly in wind turbines where the rotational speed of the alternator due to the wind may vary widely.

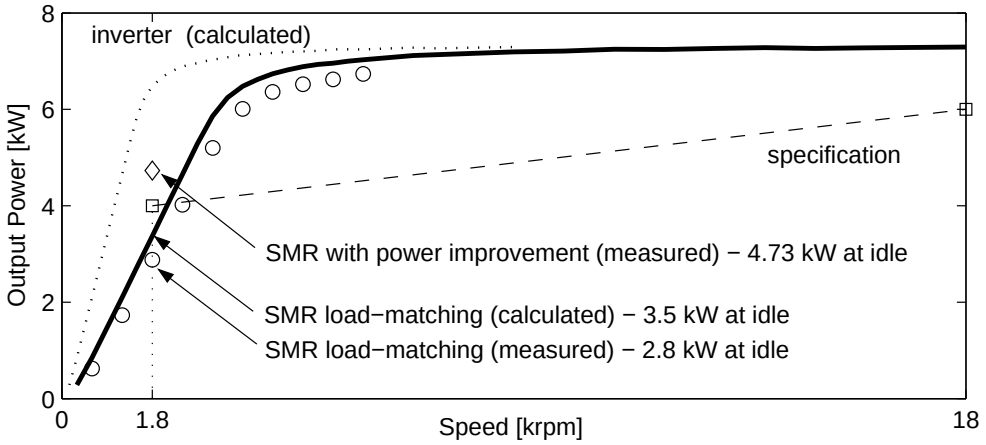

Figure 5.1: *Output power versus speed characteristics for the interior PM alternator compared against high power alternator power specifications*

5.5.1 Further Work

Although this project has investigated the operation of a interior PM alternator and demonstrated that it is capable of satisfying some of the requirements of a high power automotive alternator, there is still much scope for work and several areas could benefit from further attention:

- Experimental tests at higher alternator speeds from 6,000 rpm to 18,000 rpm have not been conducted due to the limitations of the dynamometer rig. Although it can be expected that the good field-weakening performance of the interior PM machine should allow it to maintain output power throughout the speed range, this should be experimentally verified. Due to the presence of magnet cavities, the structural strength of the interior PM rotor may need to be assessed for high speed tests.

- The accuracy of the steady-state interior PM machine model appears to be affected by the presence of a rectifier. This inaccuracy has been observed as an overestimation of voltage overshoot in the predicted steady-state VI loci. This may be due to the presence of non-sinusoidal current and voltage waveforms caused by a rectifier. Whilst the steady-state model is limited by its assumption of sinusoidal waveforms, preliminary dynamic model simulations without this limitation have also predicted similar results.

- The inconsistency found between the dynamic response observed in the duty-cycle step response of the alternator and the Bode plot measurements suggest that the

accuracy of the modelled transfer function may need to be improved. Inaccurate modelling of the transfer function may be the cause of the steady-state oscillations observed in the closed-loop system. Other possible causes are non-linearity in the output current response, mechanical oscillations in the dynamometer rig, or digital control loop limitations. It is possible that the greater mechanical stiffness of an automotive engine as compared with the dynamometer rig may alleviate this problem.

- A more sophisticated controller may provide better performance with respect to reducing steady-state oscillations. Designs involving integral and differential gain were considered, however no significant improvement was predicted by simulations. Other options such as a feed-forward mechanism may also be applied, however further designs were not implemented as it was decided that improving the idle-speed output power was more important in meeting alternator specifications.

- The most severe load dump test conducted involved a dump of 800 W. Although the controller responded quickly in this case to clamp the voltage to 110% nominal voltage, more severe load dump tests should be carried out. These were not attempted in this study due to concerns with the mechanical robustness of the dynamometer rig under such stresses.

- The controller could be modified to incorporate both closed-loop voltage regulation and the idle-speed power improvement modulation scheme. The location of optimum operating points in the modulation parameter space at speeds other than idle has not been investigated and this knowledge would be essential for such a variable-speed controller. The modulation scheme also offers the possibility of obtaining comparable output power to conventional load-matching but with a reduced stator current and therefore losses. This adds extra power management flexibility to the controller.

- The iron losses in the interior PM alternator rise significantly with speed. This is likely due to the high frequency flux density harmonics under field-weakening operation. Modification of the rotor design to reduce this effect could improve the efficiency of the alternator and aid in achieving the efficiency specification [41].

Bibliography

[1] A. Emadi, *Handbook of Automotive Power Electronics and Drives*. CRC Press, 2005.

[2] J. Miller, "Multiple Voltage Electrical Power distribution System for Automotive Applications," in *31st Intersociety Energy Conversion Engineering Conference, Washington, D.C*, August 1996.

[3] Forum Bordnetz, "Year 2005 generic luxury vehicle," 2000, homepage bordnetzforum-42V.de.

[4] E. Lovelace, "Optimization of a Magnetically Saturable Interior Permanent-Magnet Synchronous Machine Drive," Ph.D. dissertation, Massachusetts Institute of Technology, June 2000.

[5] J. Kassakian and D. Perreault, ""The Future of Electronics in Automobiles"," in *Power Semiconductor Devices and ICs, Proceedings of the 13th International Symposium on*, 2001, pp. 15–19.

[6] P. Nicastri and H. Huang, "42V PowerNet: Providing the Vehicle Electrical Power for the 21st Century," *SAE Transactions*, vol. 109, no. 7, pp. 447–453, 2000.

[7] G. Hassan, D. Perreault, and T. Keim, "Design of dual-output alternators with switched-mode rectification," *IEEE Transactions on Industry Applications*, vol. 20, no. 1, pp. 164–172, 2005.

[8] J. Kassakian, "Automotive electrical systems-the power electronics market of the future," in *Proceedings of the IEEE Applied Power Electronics Conference*, vol. 1, Feb. 2000, pp. 3–9.

[9] D. Perreault and V. Caliskan, "Automotive Power Generation and Control," *IEEE Transactions on Power Electronics*, vol. 19, no. 3, pp. 618–630, 2004.

[10] M. Naidu and J. Walters, "A 4-kW 42-V Induction-Machine-Based Automotive Power Generation System With a Diode Bridge Rectifier and a PWM Inverter," *IEEE Transactions on Industry Applications*, vol. 39, no. 5, pp. 1287–1293, 2003.

[11] R. Henry, B. Lequesne, J. Ronning, and Y. Xue, "Belt-Driven Starter-Generator for Future 42-Volt Systems," Technical Paper, Society of Automotive Engineers, March 2001.

[12] B. Lequesne, R. Henry, Y. Xue, and J. Ronning, "Design and Testing of a Belt-Driven Induction Starter-Generator," *IEEE Transactions on Industry Applications*, vol. 38, no. 6, pp. 1525–1533, 2002.

[13] J. Miller, A. Gale, P. McCleer, F. Leonardi, and J. Lang, "Starter-Alternator for Hybrid Electric Vehicle: Comparison of Induction and Variable Reluctance Machines and Drives," in *Proceedings of the IEEE Industry Applications Society Annual Meeting*, 1998, pp. 513–523.

[14] R. Schiferl and T. Lipo, "Power Capability of Salient Pole Permanent Magnet Synchronous Motor in Variable Speed Drive Applications," *IEEE Transactions on Industry Applications*, vol. IA-23, pp. 115–123, 1990.

[15] J. Rivas, D. Perreault, and T. Keim, "Performance Improvement of Alternators with Switched-Mode Rectifiers," *IEEE Transactions on Energy Conversion*, vol. 19, no. 3, pp. 561–568, 2004.

[16] W. Soong and N. Ertugrul, "Inverterless High Power Interior Permanent Magnet Automotive Alternator," *IEEE Transactions on Industry Applications*, vol. 19, no. 4, pp. 1083–1091, 2004.

[17] M. Allen, "Whatever Happened to the 42-Volt Car?" http://www.popularmechanics.com/cars/news/4226979, 2009, [Online; accessed 15-July-2011].

[18] A. Emadi, Y. J. Lee, and K. Rajashekara, "Power electronics and motor drives in electric, hybrid electric, and plug-in hybrid electric vehicles," *IEEE Transactions on Industrial Electronics*, vol. 55, no. 6, pp. 2237 –2245, June 2008.

[19] S. Deffree, "Gearing up to 42V," *Electronic News*, Nov. 2002.

[20] G. Wagner and S. Irving, "Gear up for the shift to 42V systems," *EETimes Asia*, Apr. 2007.

[21] M. Shrud, A. Bousbaine, A. Elazrag, and N. Benamrouche, "Analysis and simulation of a 42v power system for automotive applications," in *Universities Power Engineering Conference (UPEC), 2009 Proceedings of the 44th International*, Sept. 2009, pp. 1 –5.

[22] D. Stoia and M. Cernat, "Design of a 42 v automotive alternator with integrated switched-mode rectifier," in *Advanced Electromechanical Motion Systems Electric Drives Joint Symposium, 2009. ELECTROMOTION 2009. 8th International Symposium on*, July 2009, pp. 1 –8.

[23] C. Mudannayake and M. Rahman, "Control design of an induction machine based integrated starter alternator for 42v powernet," in *Industry Applications Conference, 2006. 41st IAS Annual Meeting. Conference Record of the 2006 IEEE*, vol. 3, Oct. 2006, pp. 1585 –1592.

[24] Z. Xueyi, Z. Qingliang, and S. Liwei, "Study on controlled rectification constant-voltage of the 42v rare-earth permanent-magnet generator on vehicles," in *Computer, Mechatronics, Control and Electronic Engineering (CMCE), 2010 International Conference on*, vol. 4, Aug. 2010, pp. 24 –27.

[25] D. Xiao, K. You, and M. Rahman, "Implementation of a matrix-z-source converter for isa 42v system using indirect space vector modulation," in *Electrical Machines and Systems (ICEMS), 2011 International Conference on*, Aug. 2011, pp. 1 –6.

[26] S. C. Tang, D. Otten, T. Keim, and D. Perreault, "Design and evaluation of a 42-v automotive alternator with integrated switched-mode rectifier," *IEEE Transactions on Energy Conversion*, vol. 25, no. 4, pp. 983 –992, Dec. 2010.

[27] F. Carrichi, F. Crescimbini, E. Santini, and L. Solero, "High-Efficiency Low-Volume, Starter/Alternator for Automotive Applications," in *Proceedings of the IEEE Industry Applications Society Annual Meeting*, vol. 1, 2000, pp. 215–222.

[28] F. Liang, J. Miller, and S. Zarei, "A Control Scheme to Maximize Output Power of a Synchronous Alternator in a Vehicle Electrical Power Generation System," in *Proceedings of the IEEE Industry Applications Society Annual Meeting*, vol. 2, 1996, pp. 830–835.

[29] E. Lovelace, T. Jahns, and J. Lang, "Impact of saturation and inverter cost on interior pm synchronous machine drive optimization," *IEEE Transactions on Industry Applications*, vol. 36, no. 3, pp. 723–729, 2000.

[30] M. Naidu, R. Henry, and N. Boules, "A 3.4 kW, 42 V High Efficiency Automotive Power Generation System," Technical Paper, Society of Automotive Engineers.

[31] D. Whaley, G. Ertasgin, W. Soong, N. Ertugrul, J. Darbyshire, H. Dehbonei, and C. Nayar, "Investigation of a low-cost grid-connected inverter for small-scale wind turbines based on a constant-current source PM generator," *32nd Annual Conference on Industrial Electronics*, pp. 4297–4302, 2006.

[32] M. Pathmanathan, W. Soong, and N. Ertugrul, "Output power capability of surface PM generators with switched-mode rectifiers," *Proceedings of the IEEE International Conference on Sustainable Energy Technologies*, pp. 1–6, 2010.

[33] M. Pathmanathan and W.L. Soong and N. Ertugrul, "Investigation of phase advance modulation with surface permanent magnet generators," in *Power Engineering Conference, 2009. AUPEC 2009. Australasian Universities*, Sept. 2009, pp. 1 –6.

[34] M. Pathmanathan, W. Soong, and N. Ertugrul, "Maximum torque per ampere control of phase advance modulation of a spm wind generator," in *Energy Conversion Congress and Exposition (ECCE), 2011 IEEE*, Sept. 2011, pp. 1676 –1683.

[35] A. Adnanes, "Power Feed-Back During Controller Failure in Inverter Fed Permanent Magnet Synchronous Motor Drives with Flux-Weakening," in *Proceedings of the IEEE Power Electronics Specialists*, 1992, pp. 958–963.

[36] V. Caliskan, D. Perreault, T. Jahns, and J. Kassakian, "Analysis of Three-Phase Rectifiers with Constant-Voltage Loads," *IEEE Transactions on Circuits and Systems—Part I: Fundamental Theory and Applications*, vol. 50, no. 9, pp. 1220–1225, 2003.

[37] T. Jahns and V. Caliskan, "Uncontrolled Generator Operation of Interior PM Synchronous Machines Following High-Speed Inverter Shutdown," *IEEE Transactions on Industry Applications*, vol. 35, no. 6, pp. 1347–1357, 1999.

[38] B. Welchko, T. Jahns, W. Soong, and J. Nagashima, "IPM Synchronous Machine Drive Response to Symmetrical and Asymmetrical Short Circuit Faults," *IEEE Transactions on Energy Conversion*, vol. 18, no. 2, pp. 291–298, 2003.

[39] W. Soong and N. Ertugrul, "Field-Weakening Performance of Interior Permanent Magnet Motors," *IEEE Transactions on Industry Applications*, vol. 38, no. 5, pp. 1251–1258, 2002.

[40] J. Kikuchi, M. Manjrekar, and T. Lipo, "Performance Improvement of Half Controlled Three Phase PWM Boost Rectifier," in *Proceedings of the IEEE Power Electronics Specialists*, 1999, pp. 319–324.

[41] V. Zivotic-Kukolj, W. Soong, and N. Ertugrul, "Investigation of Iron Losses in a High Flux Interior PM Automotive Alternator," in *Proceedings of Australasian Universities Power Engineering Conference (AUPEC)*, vol. 3, 2004.

Appendix A

Publications

1. C. Liaw, W. Soong, B. Welchko and N. Ertugrul, "Uncontrolled Generation in Interior Permanent Magnet Machines," *IEEE Transactions on Industry Applications*, vol. 41, no. 4, pp. 945–954, 2005.

2. C. Liaw, D. Whaley, W. Soong and N. Ertugrul, "Investigation of Inverterless Control of Interior Permanent Magnet Alternators," *IEEE Transactions on Industry Applications*, vol. 42, no. 2, pp. 536–544, 2006.

3. C. Liaw, W. Soong and N. Ertugrul, "Closed-Loop Control and Performance of an Inverterless Interior PM Automotive Alternator," in *Proceedings of the International Conference on Power Electronics and Drive Systems*, vol. 1, pp. 343–348, 2005.

4. C. Liaw, W. Soong and N. Ertugrul, "Low-Speed Output Power Improvement of an Interior PM Automotive Alternator," in *Proceedings of the IEEE Industry Applications Society Annual Meeting*, vol. 1, pp. 27–34, 2006.

C. Liaw, W. Soong, B. Welchko and N. Ertugrul (2005) Uncontrolled Generation in Interior Permanent Magnet Machines.
IEEE Transactions on Industry Applications, v. 41, (4), pp. 945-954, July/August 2005

C. Liaw, D. Whaley, W. Soong and N. Ertugrul (2006) Investigation of Inverterless Control of Interior Permanent Magnet Alternators.
IEEE Transactions on Industry Applications, v. 42, (2), pp. 536-544, March/April 2006

C. Liaw, W. Soong and N. Ertugrul (2005) Closed-Loop Control and Performance of an Inverterless Interior PM Automotive Alternator.
Proceedings of the International Conference on Power Electronics and Drive Systems, 2005. PEDS 2005, v. 1, pp. 343-348

C. Liaw, W. Soong and N. Ertugrul (2006) Low-Speed Output Power Improvement of an Interior PM Automotive Alternator.
Proceedings of the IEEE Industry Applications Society Annual Meeting, 41st IAS Annual Meeting, v. 1, pp. 27-34, October 2006

Appendix B

Programs

This appendix contains code listings of the main programs used in the course of this work both to produce theoretical simulations of the interior PM alternator and to control the alternator power electronics.

B.1 Matlab and Simulink Code

Listing B.1: *Steady-state model calculation of interior PM machine voltage-current loci*

```
% Generate normalised VI loci vs speed/resistance/saliency/saturation
% (using saturation model described by Jahns)
clear

v_rated = 69.3;
i_rated = 2.83;
r_rated = v_rated/i_rated;

% Stator Parameters
Rph = 0;    %2.94;                  % phase resistance for 1500 rpm case
Eo= 69.3/sqrt(3);              % machine open-circuit back-emf, Vrms per phase at Wrpm_Eo
% from Rotor 3 Test 3 data
poles = 2;                      % number of pole pairs
phases =3 ;                     % number of phases

% 2.2kW Rotor 4b with NdFeB solid magnets
Wrpm_Eo = 1500 ;                % speed in rpm at which Eo is defined
W_Eo = Wrpm_Eo ./ 60 .* 2 .* pi .* poles;
Psi = Eo ./ W_Eo;               % calculate flux linkage (Vrms/rad/s)

% define values of Ld and Lq
L_dn = 0.045;                   % d-axis phase inductance
L_qno = 0.345;                     % q-axis phase inductance unsaturated
L_qn = 0.345;                    % q-axis phase inductance starting value


for Rph = 6.0 %[0:0.2:0.8 1.2 1.8 3.0].*r_rated %[0:0.1:8.0],

% Normalised R calculations
Wtest = 1500;
w= 2*pi*(Wtest/60)*poles;
R_n = Rph/(w*L_dn)
```

```
Rph_unity = 1*(w*L_dn)

    for Xi = 6% [1 2 4 6 8];% 32 64 128 25 512 1024 2048 ],
        L_qno = L_dn*Xi;
        L_qn = L_qno;
        for beta_n = 0 %[0 1 2 3 6 16]%40 80 100 200],
            for Wtest= [1:5]*1500./5, %[110 225 450 700 1000 1500]
                %%%%%%%%%%%%%%%%%%%%%%%%%%%%%%%%%%%%%%%%%%%%%%%%%%%%%%%%%%%%%%%%%%%%%%%%%%%%%%%%
                w= 2*pi*(Wtest/60)*poles;       % calculate maximum electrical frequency
                % R= logspace(0,3,300);         % generate array of resistances
                R= logspace(-1,4,300);          % generate array of resistances
                w_rpm= w .*60 ./ (2*pi) ./poles;

                for count =1:10
                    theta= atan((R+Rph) ./(w .* L_qn));   % find angle between current and d-axis
                    Z= (R+Rph) .* sin(theta) + w .* L_dn .* cos(theta);     % calculate load Z
                    Isalient = Psi .* w ./ Z;     % calculate phase current

                    % calculate Id and Iq
                    I_qn= Isalient .* sin(theta);
                    I_dn= Isalient .* cos(theta);

                    % find new value of Lq based on Iq
                    Lq_new= L_dn + ( (L_qno - L_dn) ./ sqrt(1 + (beta_n .* I_qn).^2 ) );
                    error= max(Lq_new-L_qn);
                    L_qn= Lq_new;
                end

                Tsalient_18= poles .* phases .* (Psi .* I_qn + (L_qn-L_dn).*I_dn.*I_qn);
                Pmsalient_18= Tsalient_18 .* w / poles;
                Vsalient_18= Isalient .* R;
                Psalient_18= phases .* Vsalient_18 .* Isalient;
                Isalient_18= Isalient;

                % Plot out results (normalised voltage and current)
                figure(1)
                plot(sqrt(3).*Vsalient_18./v_rated, abs(Isalient_18)./i_rated,'k-');
                hold on;

                % plot max voltage points
                [y,i] = max(Vsalient_18);
                plot(sqrt(3)*y./v_rated, Isalient_18(i)./i_rated,'ro');

                %                  % plot saliency values
                %                  [y,i] = max(Vsalient_18);
                %                  text(y./0.1986 + 0.02, Isalient_18(i), num2str(Xi));

            end
        end
    end
end

hold off;

ylabel('Stator␣Current␣[pu]')
xlabel('Line␣Voltage␣[pu]')
axis([0 1.4 0 1.1]);
set(1, 'position', [524   324   860   400]);

% thesisfig(1);
```

Simulink model used to calculate interior PM machine waveforms under uncontrolled generation

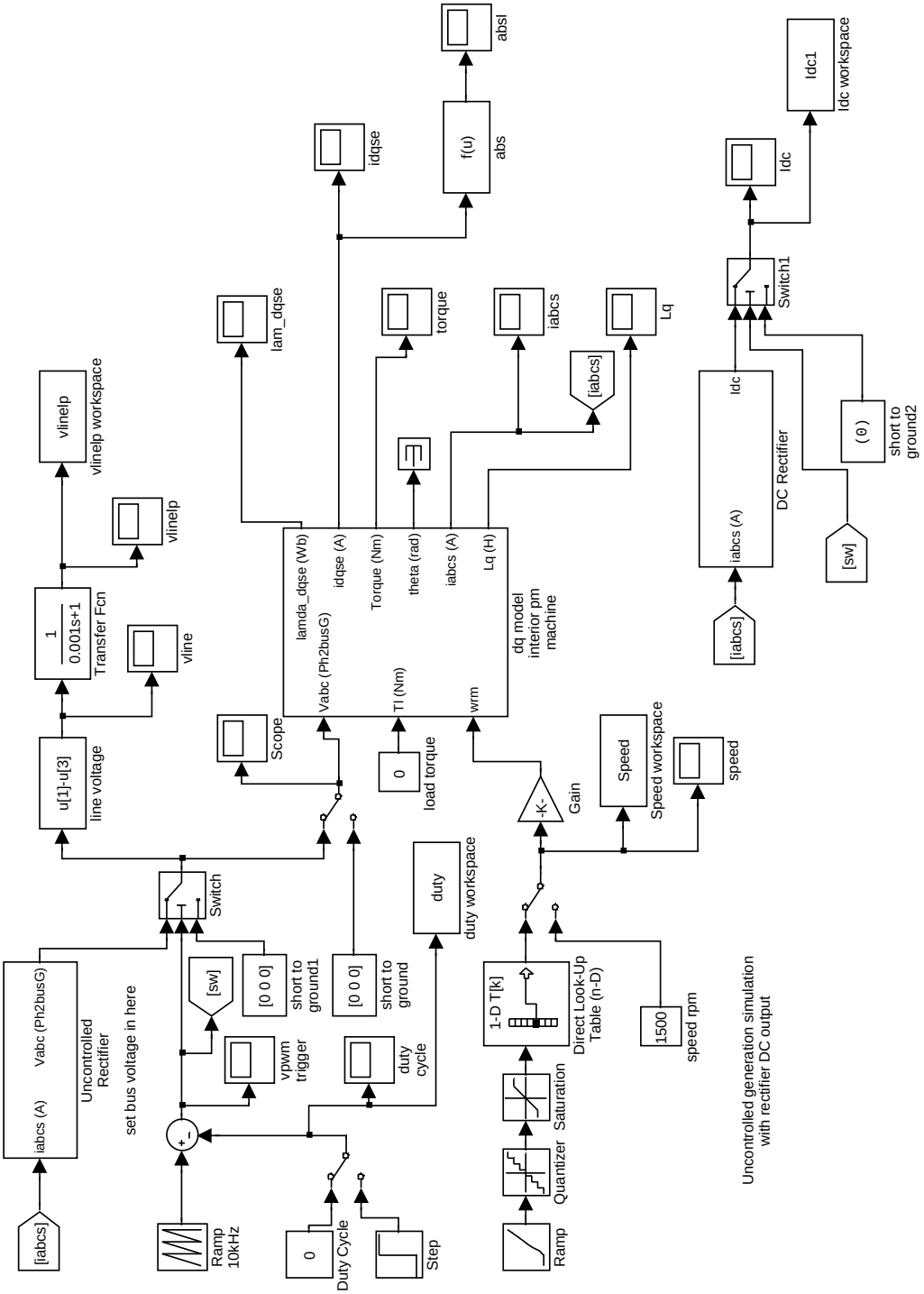

Simulink model used to calculate dynamic response of interior PM machine under closed-loop inverterless load-matching operation

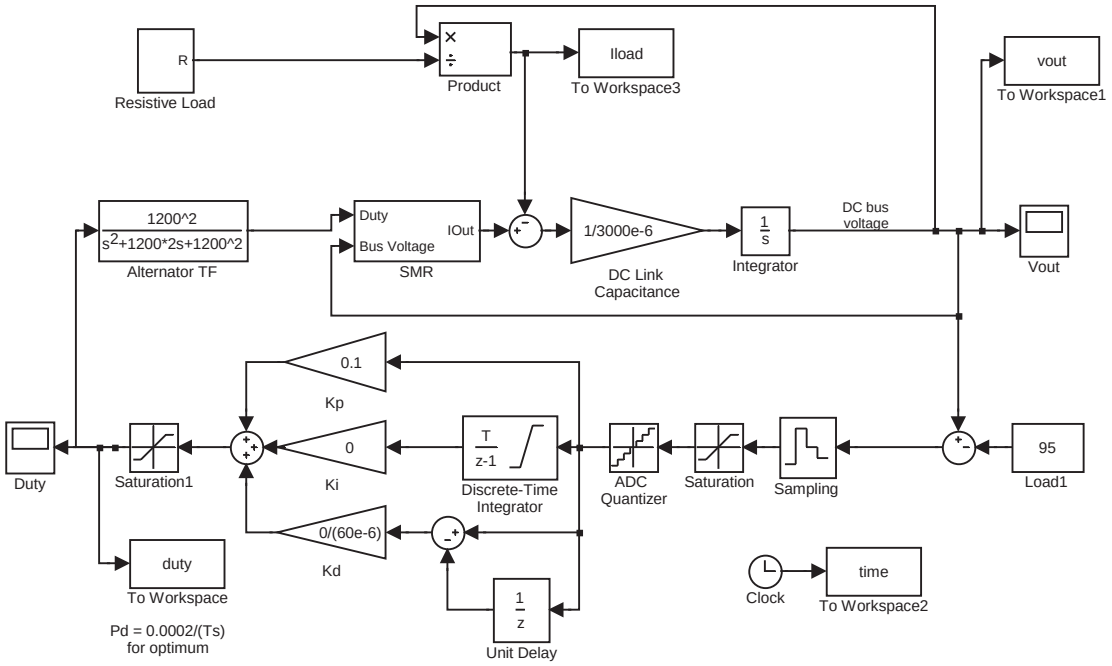

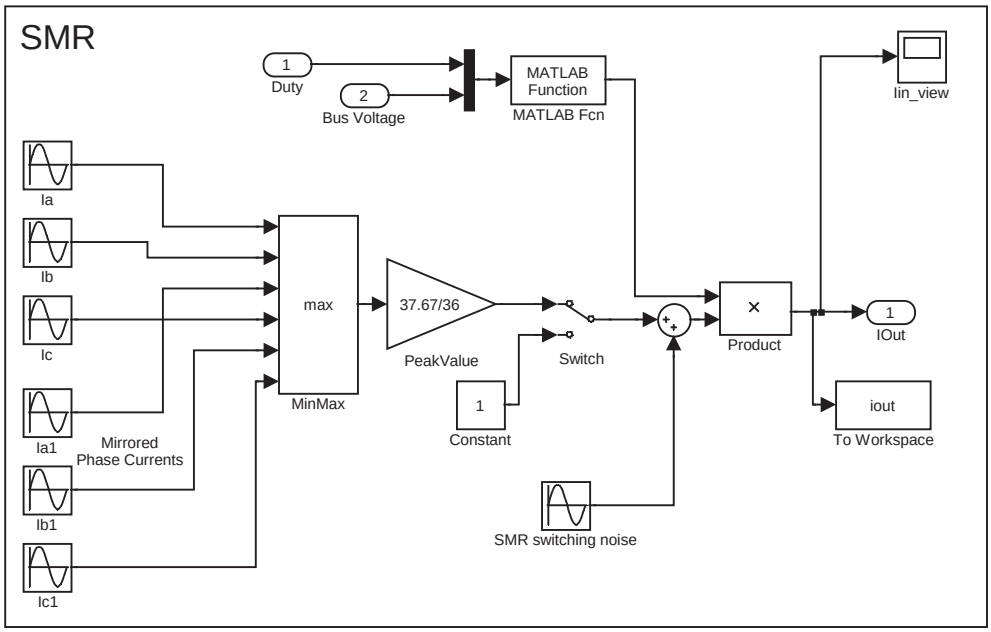

Simulink model used to calculate interior PM machine waveforms under phase-advance SMR modulation for idle-speed power improvement (main block)

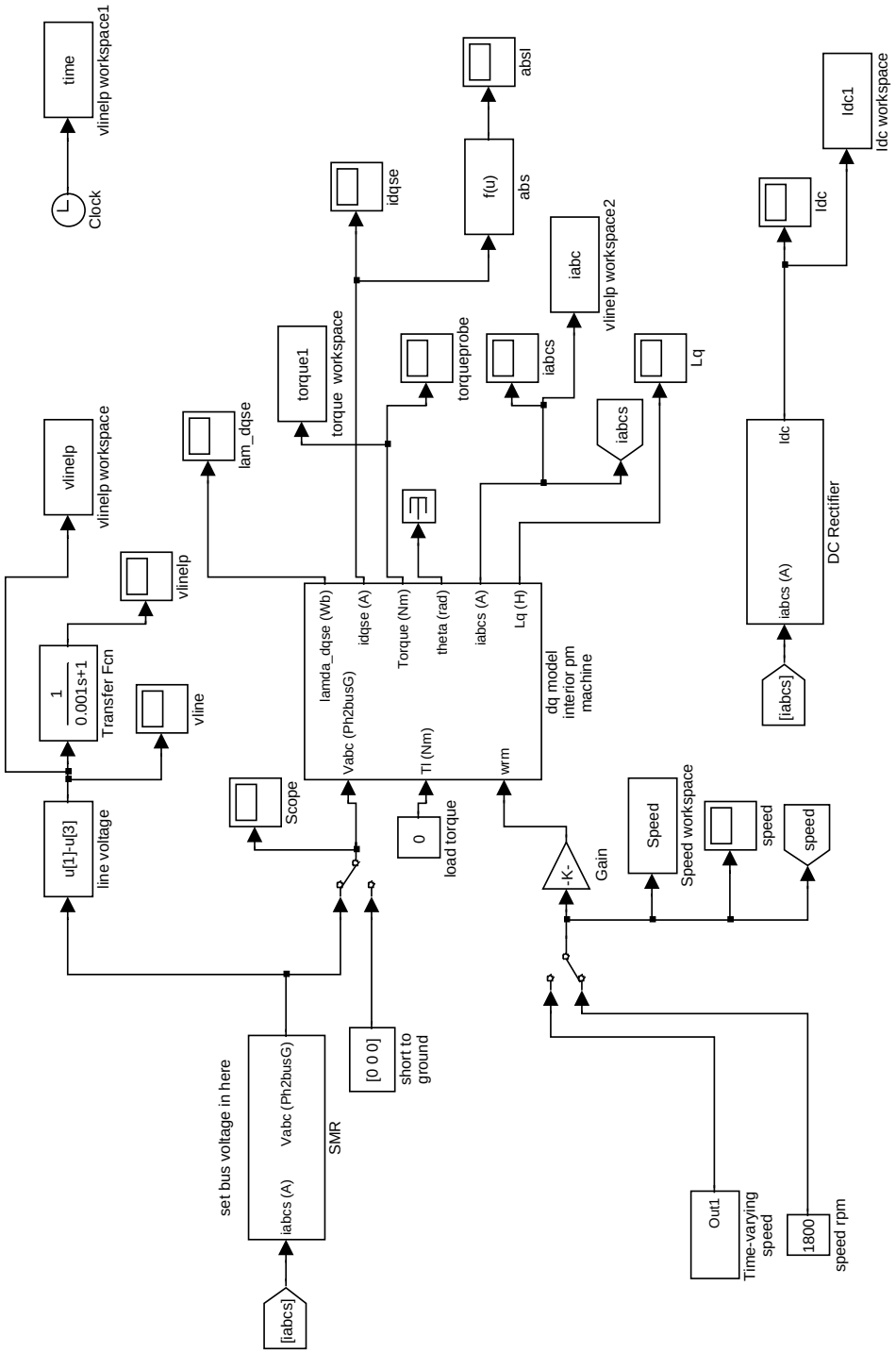

Simulink model used to calculate interior PM machine waveforms under phase-advance SMR modulation for idle-speed power improvement (SMR block)

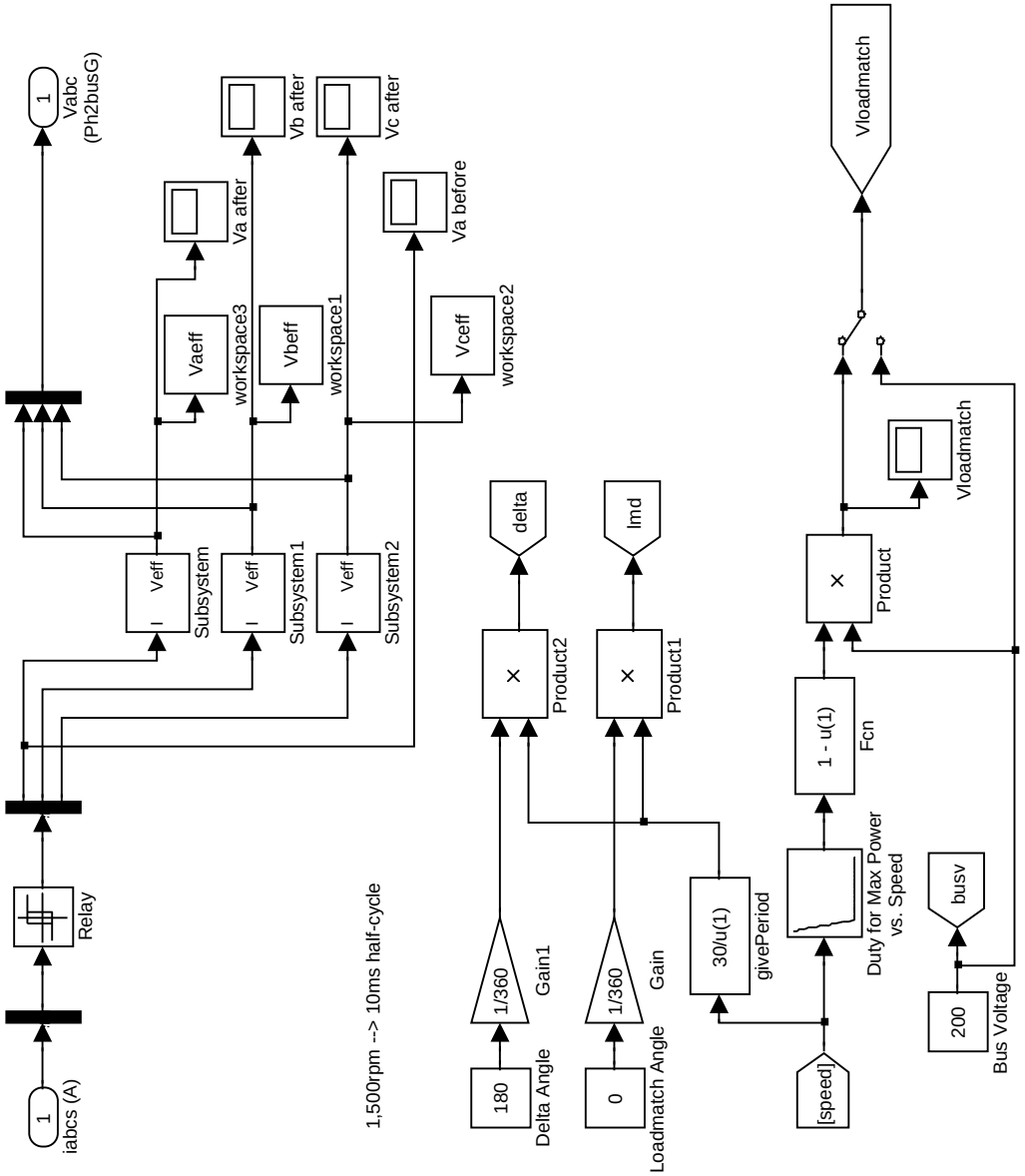

B.2 Microcontroller Code

B.2.1 Closed-Loop Control

Closed-loop control of the interior PM alternator was implemented on the Mitsubishi MSA0654 development board. This microcontroller had a 10-bit analog-to-digital converter (A/D) module which supported conversions from 8 input pins in a 'sweep' mode where the voltages on the pins are read in quick succession. All A/D pins were used to monitor the DC link voltage of the alternator and the multiple readings were averaged. As no dedicated PWM modules were available, the PWM signal used to control the switched-mode rectifier was generated using timers.

Not included is a version of the code which includes additional functions used during development and testing. For instance, a few variations on A/D sweep configurations were tested to determine the effect on the quality of the reading - with or without sample and hold, or with averaging of all eight pin readings as opposed to discarding the maximum and minimum readings.

The digital-to-analog (D/A) module of the microcontroller was primarily used to output a 0-4.9 V voltage proportional to the 0-100% duty-cycle command produced by the control loop. The D/A module was also used to output several other signals for testing purposes - a sharp pulse to signal the end of each control loop period, a constant 2.5 V and a 'noise measure' voltage which is the sum of inter-reading variations over a fixed interval, for use as a rough real-time measure of the variability of the DC link voltage reading.

Despite suitable low-pass filtering and averaging of the A/D readings, difficulties were encountered in minimising the effect of noise on the DC link voltage reading, particularly due to the interference caused by large currents being switched at high frequencies. The testing functions aided in adjusting the experimental equipment to reduce interference.

Listing B.2: *Closed-loop controller code*

```
/*******************************************************/
/*      SAMPLE PROGRAM 1 FOR MSA0654-MEAUST BOARD      */
/*      FILENAME: Invert2.c                            */
/*      WRITTEN BY: C.Z. Liaw, D.M. Whaley  12/11/2004 */
/*      DESCRIPTION:                                   */
/*                                                     */
/*      *** NOTE: there is a 14mV offset with the      */
/*      PWM signal (output pin)                        */
/*                                                     */
/*******************************************************/

#include "sfr62.h"
#include "leddata.h"

void main(void);
void initimerA0(void);
void initport(void);
void ADCint(void);
void timerA2int(void);
void initADC(void);
void initDAC(void);

#pragma INTERRUPT INT0int
#pragma INTERRUPT INT1int
#pragma INTERRUPT timerA2int
#pragma INTERRUPT ADCint

unsigned char counter = 0;
unsigned int sw_freq = 4;               // set switching frequency (in kHz)
unsigned int sw_cycles;

unsigned int busv10bit = 0;
unsigned int busv8bit = 0;
unsigned int counter10bit = 0;
unsigned int v_out = 0;
unsigned char da0_out = 0;
unsigned char da1_out = 0;
unsigned int duty_out = 0;

void main(void)
{
        unsigned int newtimervalue = 0;
        unsigned int oldtimervalue = 0;
        unsigned int currentreading = 0;

        sw_cycles = 16000 / sw_freq;    // sets timer using f00

        // Init timers and interrupts
        initimerA0();
        initport();
        int0ic = 0x02;  // set int0 to level 2
        int1ic = 0x01;  // set int1 to level 1

        // Init ADC and DAC
        initADC();
        initDAC();

        // Setup numeric LED display and PWM equiv. voltage output
        ta2mr = 0x80;   // set up timerA0 for
        ta2 = 0x1388;   // for 100Hz LED refresh rate
        ta2ic =0x03;    // set interrupt level for update
        adic = 0x04;    // set interrupt for AD converter
        tabsr |= 0x04;  // starts timerA2 counting

        // Main loop

        while(1)  {

                asm("fset_I");          // enable interrupts
```

```
                adst = 1;               // start AD conversion
                while (adst == 1);      // wait till AD conversion is completed

                busv8bit = busv10bit;
                busv8bit >>= 2; // Convert 10bit reading to 8bit reading
                da1_out = busv8bit;
                da1 = da1_out;

                // Limit busv to 40V - 60V range
                // corresponding to 82 - 122

                if (busv10bit < 82)
                {
                        busv10bit = 82;
                }
                if (busv10bit > 122)
                {
                        busv10bit = 122;
                }

                // Calculate new timerA1 value
                // 100 is sw_cycles/(204-164), valid only for 4kHz PWM period

                oldtimervalue = newtimervalue;
                currentreading = (busv10bit - 82)*100;

                // 8x averaging
//              newtimervalue = ((oldtimervalue*7) + currentreading)/8;
                newtimervalue = currentreading;

                if (newtimervalue > sw_cycles)
                {
                        newtimervalue = sw_cycles;
                }

                // Limit minimum duty cycle to 80%, for stability during speedup
/*
                if (newtimervalue < 3200)
                {
                        newtimervalue = 3200;
                }
*/
                // Load new value into timerA1 register
                ta1 = newtimervalue;

                // Output equivalent PWM voltage: 0-100% as 0-250 = 0-4.902V

                v_out = newtimervalue/16;
                da0_out = v_out;
                da0 = da0_out;

// Main-loop timing pulse
/*
                da0 = 255;
                da0 = 0;
*/

                // Generate new counter value for LED display
                // This gives 0-100% as 0-100:

                counter10bit = newtimervalue/40;
                counter = counter10bit;
        }
}

//////////////////////////////////////////
// TimerA0 resets once every duty cycle period

void initimerA0(void)
{
        ta0mr = 0x00;           // set timer A0 for f1 use
```

```
        ta0 = sw_cycles;        // set reload register for 16,000 cycles => 1ms
        ta1mr = 0x16;           // set timer A1 for f1 use and one-shot timer mode, outputs pulse on TA1OUT
        trgsr = 0x02;           // timer A1 event/trigger select bit - TA0 overflow selected
        tabsr |= 0x01;

        ta1 = 0;        // set timer A1 register for 0 cycles => 0.0ms ie 0% duty
        tabsr |= 0x02;  // timerA1 starts counting
}

//////////////////////////////////////////
// Initialise output ports

void initport(void)
{
        pd0 = 0xFF;     // output mode
        pd1 = 0xFF;     // output mode
        pu00 = 0;       // no pull up for P0_0 to P0_3
        pu01 = 0;       // no pull up for P0_4 to P0_7
        pu02 = 0;       // no pull up for P1_0 to P1_3
        p0 = 0x00;      // initial data to Port 0
        p1 = 0xFF;      // initial data to Port 1

}



//////////////////////////////////////////////////////////////////
// Interrupt for updating LED Display and PWM equiv. voltage output

void timerA2int(void)
{
        static unsigned char led_number = 0;
        unsigned char offset;

        asm("fset I");                  // enable interrupts

        if (led_number == 0)
        {
                led_number = 1;
                p0 = 0xFF;
                p1 = 0xFD;                      // disable LED 1 and enable LED2

                if (counter == 100)
                {                               // displays '1H' for 100% duty cycle
                        p0 = 0x89;              // displays 'H' on LED 2
                }                               // displays '1' on LED 1
                else
                {
                        offset = counter % 10;
                        p0 = leddigit[offset];  // display remainder (1's figure) on LED 2
                }
        }
        else
        {
                led_number = 0;
                p0 = 0xFF;
                p1 = 0xFE;                      // disable LED 2 and enable LED1

                if (counter == 100)
                {                               // displays '1H' for 100% duty cycle
                        p0 = leddigit[1];       // displays '1' on LED 1
                }                               // displays 'H' on LED 2
                else
                {
                        offset = counter / 10;
                        p0 = leddigit[offset];  // display quotient (10's figure) on LED 1
                }
        }

}
```

```
////////////////////////////////////////////////
// ADC interrupt function

void ADCint(void)
{
        static unsigned int busvacc = 0;        // Initialise BusV accumulator
        static unsigned int max = 0;            // Initialise Max/Min
        static unsigned int min = 1023;

        asm("fset I");          // enable interrupts

        busv10bit = 0;

        busvacc = ad0h; // Read AD0
        busvacc <<= 8;
        busvacc += ad0l;
        if (busvacc > max) {
                max = busvacc;
        }
        if (busvacc < min) {
                min = busvacc;
        }
        busv10bit += busvacc;

        busvacc = 0;
        busvacc = ad1h; // Read AD1
        busvacc <<= 8;
        busvacc += ad1l;
        if (busvacc > max) {
                max = busvacc;
        }
        if (busvacc < min) {
                min = busvacc;
        }
        busv10bit += busvacc;

        busvacc = 0;
        busvacc = ad2h; // Read AD2
        busvacc <<= 8;
        busvacc += ad2l;
        if (busvacc > max) {
                max = busvacc;
        }
        if (busvacc < min) {
                min = busvacc;
        }
        busv10bit += busvacc;

        busvacc = 0;
        busvacc = ad3h; // Read AD3
        busvacc <<= 8;
        busvacc += ad3l;
        if (busvacc > max) {
                max = busvacc;
        }
        if (busvacc < min) {
                min = busvacc;
        }
        busv10bit += busvacc;

        busvacc = 0;
        busvacc = ad4h; // Read AD4
        busvacc <<= 8;
        busvacc += ad4l;
        if (busvacc > max) {
                max = busvacc;
        }
        if (busvacc < min) {
                min = busvacc;
        }
        busv10bit += busvacc;
```

```
        busvacc = 0;
        busvacc = ad5h; // Read AD5
        busvacc <<= 8;
        busvacc += ad5l;
        if (busvacc > max) {
                max = busvacc;
        }
        if (busvacc < min) {
                min = busvacc;
        }
        busv10bit += busvacc;

        busvacc = 0;
        busvacc = ad6h; // Read AD6
        busvacc <<= 8;
        busvacc += ad6l;
        if (busvacc > max) {
                max = busvacc;
        }
        if (busvacc < min) {
                min = busvacc;
        }
        busv10bit += busvacc;

        busvacc = 0;
        busvacc = ad7h; // Read AD7
        busvacc <<= 8;
        busvacc += ad7l;
        if (busvacc > max) {
                max = busvacc;
        }
        if (busvacc < min) {
                min = busvacc;
        }
        busv10bit += busvacc;

        busv10bit -= min;       // Discard minimum and maximum readings
        busv10bit -= max;
        busv10bit = busv10bit/6;
}

////////////////////////////////////////////////
// Initialise ADC on pin AN2

void initADC(void)
{
    adcon2 = 0x01;      // ---- ---X
                        //         +- 0: without sample and hold
                        //            1: with sample and hold


    adcon0 = 0x02;      // X000 0010  AN2 selected
                        // |||| +---- must be fixed to 1 in repeat mode
                        // |||+------ must be fixed to 0 in repeat mode
                        // ||+------- trigger select bit
                        // ||         0: software trigger
                        // ||         1: external trigger (ADtrg, P10.0)
                        // |+-------- 0: A-D conversion disabled
                                //  |          1: A-D conversion enabled
                        // +--------- frequency select bit 0:
                        //            0: fad/4 is selected
                        //            1: fad/2 is selected
                        //            please look at bit 4 of ADCON1
                        //            (ADCON1.4) also)


     adcon1 = 0x38;         // 0011 10XX
                            // |||| |+--- must be fixed to 0 in one shot mode
                            // |||| +---- 0: 8-bit mode
                            // ||||       1: 10-bit mode
```

```
                        // |||+------ frequency select bit 1
                        // |||        0: fad/2 or fad/4 is selected
                        // |||           please look at bit 7 of ADCON0
                        // |||        1: fad is selected
                        // ||+------- 1: Vref connected (must be fixed to
                        // ||           1 if A-D conversion is used)
                        // |+-------- ext. op amp connection mode bits
                        // +--------- ext. op amp connection mode bits
                        //            00: ANEX0 and ANEX1 are not used
                        //            01: ANEX0 input is A-D converted
                        //            10: ANEX1 input is A-D converted
                        //            11: external op amp connection mode


}

////////////////////////////////////////////////
// Initialise DAC on DA0 and DA1

void initDAC(void)
{
        dacon = 0x03;    // enables DA0 and DA1
}
```

B.2.2 Low-Speed Power Improvement

The modulation scheme for improving alternator output power at low speed was implemented on a Microchip dsPIC30F10 microcontroller.

Listing B.3: *main_rtc.c - main loop*

```
#include "h\p30f2010.h"
#include "h\LCD_Display.h"
#include "h\common.h"

#define Pled PORTBbits.RB0
#define alpha 0xE0
#define epsilon 0xE3

/* Variables */
volatile unsigned int lcd_update;
volatile unsigned int status_knob;
volatile unsigned int status_menu;
volatile unsigned int status_item;
volatile unsigned int param_test;
volatile unsigned int param_alpha;
volatile unsigned int param_epsilon;
volatile unsigned int alpha_limit;
volatile unsigned int epsilon_limit;

int main ( void ) {

        /* Initialize variables */
        lcd_update = 0;
//      param_test = 50;
        param_alpha = 30;
        param_epsilon = 30;
        epsilon_limit = 180 - param_alpha;
        alpha_limit = 180 - param_epsilon;

        TRISBbits.TRISB0 = 0;   // Set RB0 as output

        /* Initialise PWM and CN pins */
        PWM_Init();
        CN_Init();

        /* Initialise SPI and LCD Display */
        Display_Setup();

        // Display menu
        menu_Idle();
        params_update();
        controls_Init();

        while (1) {

/*
                Pled = 1;               // Blink on
                ms_delay(2);
        Pled = 0;               // Blink off
                ms_delay(2);
*/

                if ( lcd_update ) {
                        params_update();
        }

        }

        return 0;
}
```

Listing B.4: *menu_Idle.c - main user interface menu*

```
#include "h\p30f2010.h"
#include "h\LCD_Display.h"
#include "h\common.h"

#define Pled PORTBbits.RB0
#define alpha 0xE0
#define epsilon 0xE3

void menu_Idle(void);

void menu_Idle(void){
        status_menu = 0;
        status_item = 0;

        Display_String("IDLE_IMPROV_v0.1");
        Display_CharPos(1,1);
        Display_Byte(alpha);
        Display_Byte(':');
        hexdec(param_alpha);
        Display_CharPos(1,3);
        Display_Byte(hunds + 0x30);
        Display_Byte(tens + 0x30);
        Display_Byte(ones + 0x30);

        Display_CharPos(1,8);
        Display_Byte(epsilon);
        Display_Byte(':');
        hexdec(param_epsilon);
        Display_CharPos(1,10);
        Display_Byte(hunds + 0x30);
        Display_Byte(tens + 0x30);
        Display_Byte(ones + 0x30);


//      Display_CharPos(1,14);
//      Display_String("OK");
}
```

Listing B.5: *LCD_Display.c - code to handle LCD display functions*

```
#include "h\p30f2010.h"
#include "h\LCD_Display.h"

// Define LCD Control Lines
#define E_line PORTBbits.RB4
#define RS_line PORTBbits.RB5
// Note: Some odd behaviour using RB1. Possibly due to SPI init
// To be Added: Use SPI1 Interrupt to set command signals?

/*-------------------------------------------------------------------
  Function Name: Display_Setup
  Description:   Initialize SPI port to communicate with LCD
  Inputs:        None
  Returns:       None
-------------------------------------------------------------------*/
void Display_Setup( void )
{
        unsigned int dummy;

        TRISBbits.TRISB4 = 0;                   // Set E_line as digital output
        ADPCFGbits.PCFG4 = 1;
        TRISBbits.TRISB5 = 0;                   // Set RS_line as digital output
        ADPCFGbits.PCFG5 = 1;

        IFS0bits.SPI1IF = 0;                    // Clear SPI Interrupt Flag
        IPC2bits.SPI1IP = 4;                    // Set Interrupt Priority Level
        IEC0bits.SPI1IE = 0;                    // Disable SPI Interrupt
```

```
        SPI1CON = 0x013c; //0x013f;       // Master mode, SCK = Fcy/64 = 230kHz, Input data sampled at
                                          // middle of output time, Data clocked out on rising edge, Clk idle is lo

        SPI1STAT = 0x8000;                // Enable SPI port

        // Startup Rigmarole
        ms_delay(15);
        Display_Command(0x030);
        ms_delay(5);
        Display_Command(0x030);
        us_delay(160);
        Display_Command(0x030);
        us_delay(160);

        Display_Command(0x038);                 // Set 8-bit mode, two lines, 5x7 font
        Display_Command(0x010);                 // Turn off Display
        Display_Command(0x001);                 // Clear Display
//      Display_Command(0x06);                  // Set Cursor to auto-increment
//      Display_Command(0x0F);                  // Enable Cursor, w./ blinking

//      Display_Command(0x1C);                  // 8-bit mode, two lines, 5x7 font
        Display_Command(0x0C);                  // Turn on display and disable cursor
        Display_Command(0x06);                  // Set Cursor to auto-increment

}


/*-----------------------------------------------------------------------
  Function Name: Display_Byte
  Description:   Send a character to the LCD
  Inputs:        Byte to Display on dsPICDEM 1.1 Board LCD
  Returns:       None
-----------------------------------------------------------------------*/
void Display_Byte( unsigned char ByteToDisplay )
{
        unsigned int dummy;

        SPI1STATbits.SPIROV = 0;             // Clear overflow flag
        dummy = SPI1BUF;                     // Read buffer to avoid overflow

    SPI1BUF = ByteToDisplay;             // Write the data to the output buffer
    while (SPI1STATbits.SPITBF == 1);    // Wait for transmission to complete
        RS_line = 1;
        us_delay(1); //

        // Strobe E Line
        E_line = 1;
        us_delay(160); //
        E_line = 0;
        RS_line = 0;
}

/*-----------------------------------------------------------------------
  Function Name: Display_Command
  Description:   Send a command to the LCD
  Inputs:        Command to the LCD
  Returns:       None
-----------------------------------------------------------------------*/
void Display_Command( unsigned int Command )
{
        unsigned int dummy;

        SPI1STATbits.SPIROV = 0;             // Clear overflow flag
        dummy = SPI1BUF;                     // Read buffer to avoid overflow

    SPI1BUF = Command;              // Write the data to the output buffer
    while (SPI1STATbits.SPITBF == 1);    // Wait for transmission to complete
        RS_line = 0;
        us_delay(1);
```

```
        // Strobe E Line
        E_line = 1;
        us_delay(160);
        E_line = 0;
}

/*-------------------------------------------------------------------------
  Function Name: Display_Debug
  Description:   Sets all lines connected to the LCD to HIGH, for testing
  Inputs:        None
  Returns:       None
-------------------------------------------------------------------------*/

void Display_Debug(void)
{
        unsigned int dummy;

        SPI1STATbits.SPIROV = 0;              // Clear overflow flag
        dummy = SPI1BUF;                      // Read buffer to avoid overflow

    SPI1BUF = 0xFF;              // Write the data to the output buffer
    while (SPI1STATbits.SPITBF == 1);    // Wait for transmission to complete

        // Hold Control Lines High
        E_line = 1;
        RS_line = 1;

}

/*-------------------------------------------------------------------------
  Function Name: Display_String
  Description:   Send a string of characters to the LCD
  Inputs:        ..
  Returns:       None
-------------------------------------------------------------------------*/
void Display_String( unsigned char *Data )
{
   while(*Data)
   {
      //Display_Byte(0xa8);
      Display_Byte(*Data++);
   }
}

/*-------------------------------------------------------------------------
  Function Name: Display_CharPos
  Description:   Moves LCD cursor to specified position
  Inputs:        column and row number
  Returns:       None
  Notes:                 First row is row 0, first col is col 0
-------------------------------------------------------------------------*/

void Display_CharPos(int row, int col) {
        unsigned int command;
        command = 128 + row*64 + col;
        Display_Command(command);
}
```

Listing B.6: *pwm.c - code to handle PWM modules*

```
#include "h\p30f2010.h"
#include "h\common.h"

void PWM_Init(void);

void PWM_Init(void) {

        TRISEbits.TRISE1 = 0;    //Set PWM1-3H pins as outputs
        TRISEbits.TRISE3 = 0;
        TRISEbits.TRISE5 = 0;
```

```
        PTMR = 0;                               // Clear PWM Timer
        PTCON = 0x0004;                 // Set Timer prescale to 4
        PTPER = 127;                    // fPWM = 15.75kHz

        PWMCON1 = 0x0FF0;               // Enable high outputs in indep. mode
                                                // and disable low outputs
        PWMCON2 = 0;

        PDC1 = 64;                              // Set LM duty cycle
        PDC2 = 64;
        PDC3 = 64;

        SEVTCMP = 0;                    // Disable special events
        OVDCON = 0x00FF;                // Set all PWM outputs high
        PTCONbits.PTEN = 1;             // Enable PWM Timer


        // Calculate timer period values for alpha and epsilon
        period_alpha = param_alpha * kperiod;
        period_epsilon = param_epsilon * kperiod;
}
```

Listing B.7: *CNpins.c - code to handle CN pins for detecting phase current zero crossings*

```
#include "h\p30f2010.h"
#include "h\common.h"

// Define Phase Current Sign inputs
#define Ia PORTBbits.RB1 // CN3
#define Ib PORTBbits.RB2 // CN4
#define Ic PORTBbits.RB3 // CN5

void CN_Init(void);
void _ISR _CNInterrupt( void ); // CN handler

volatile unsigned int Ia_prev;
volatile unsigned int Ib_prev;
volatile unsigned int Ic_prev;
volatile unsigned long period_alpha;
volatile unsigned long period_epsilon;

void CN_Init(void) {

        // Clear previous values of phase current
        Ia_prev = 0;
        Ib_prev = 0;
        Ic_prev = 0;

        TRISBbits.TRISB1 = 1;                   // Set Ia as digital input
        ADPCFGbits.PCFG1 = 1;
        TRISBbits.TRISB2 = 1;                   // Set Ib as digital input
        ADPCFGbits.PCFG2 = 1;
        TRISBbits.TRISB3 = 1;                   // Set Ic as digital input
        ADPCFGbits.PCFG3 = 1;

        // SETUP TIMERS

        T1CON = 0x0000;                 //Setup Timer1 for 1:1 prescale
        TMR1 = 0;                               //Clear timer counter
        PR1 = 0xFFFF;                   //Set period
        IFS0bits.T1IF = 0;              //Clear timer interrupt flag
        IEC0bits.T1IE = 1;              //Enable timer interrupt
        IPC0bits.T1IP = 6;              //Set timer priority to 6

        T2CON = 0x0000;                 //Setup Timer2 for 1:1 prescale
        TMR2 = 0;                               //Clear timer counter
        PR2 = 0xFFFF;                   //Set period
        IFS0bits.T2IF = 0;              //Clear timer interrupt flag
        IEC0bits.T2IE = 1;              //Enable timer interrupt
```

```
        IPC1bits.T2IP = 6;              //Set timer priority to 6

        T3CON = 0x0000;                 //Setup Timer3 for 1:1 prescale
        TMR3 = 0;                           //Clear timer counter
        PR3 = 0xFFFF;                   //Set period
        IFS0bits.T3IF = 0;              //Clear timer interrupt flag
        IEC0bits.T3IE = 1;              //Enable timer interrupt
        IPC1bits.T3IP = 6;              //Set timer priority to 6

        // SETUP CN PINS TO DETECT CURRENT ZERO-CROSSINGS

        CNEN1 = 0x038;          /*Enable CN interrupt on CN3,4,5 */

        CNPU1 = 0;                          // Disable pull-ups on CN pins

        IFS0bits.CNIF = 0;      /*Reset CN interrupt flag */
        IPC3bits.CNIP = 7;              // Set CN interrupt priority to 7
        IEC0bits.CNIE = 1;              // Enable CN interrupt
}


/*-----------------------------------------------------------------------
  Function Name: CNInterrupt
  Description:   CN pin ISR - handles detection of phase current zero-crossings
  Inputs:        None
  Returns:       None
-----------------------------------------------------------------------*/
void _ISR _CNInterrupt( void ) {
        unsigned int dummy;
/*
        unsigned int temp_delay = 0x00FF;
        while ( temp_delay --);                         // crude debounce delay
*/

        IFS0bits.CNIF = 0;                              /*Reset CN interrupt flag */

        dummy = PORTB;                                          // Read PORTB to clear CN mismatch flag

        if (Ia != Ia_prev) {                            // Zero-crossing detected on phase A
                Ia_prev = Ia;

                if (Ia) {                                                       // positive zero-crossing

                        // ENTER ALPHA INTERVAL
                        PR1 = period_alpha+1;           // Set timer to alpha period
                        TMR1 = 0;                               // Reset timer value
                        T1CONbits.TON = 1;              // Activate timer
                } else {                                                        // negative zero-crossing
                        // ENTER INACTIVE INTERVAL
                        T1CONbits.TON = 0;              // Deactivate timer
                }
                        OVDEa = 0;                                              // Override output to high
                        OVDVa = 1;
        }

        if (Ib != Ib_prev) {                            // Zero-crossing detected on phase A
                Ib_prev = Ib;

                if (Ib) {                                                       // positive zero-crossing

                        // ENTER ALPHA INTERVAL
                        PR2 = period_alpha+1;           // Set timer to alpha period
                        TMR2 = 0;                               // Reset timer value
                        T2CONbits.TON = 1;              // Activate timer
                } else {                                                        // negative zero-crossing
                        // ENTER INACTIVE INTERVAL
                        T2CONbits.TON = 0;              // Deactivate timer
                }
                        OVDEb = 0;                                              // Override output to high
                        OVDVb = 1;
        }
```

```
        if (Ic != Ic_prev) {                                    // Zero-crossing detected on phase A
                Ic_prev = Ic;

                if (Ic) {                                                       // positive zero-crossing

                        // ENTER ALPHA INTERVAL
                        PR3 = period_alpha+1;                   // Set timer to alpha period
                        TMR3 = 0;                                               // Reset timer value
                        T3CONbits.TON = 1;                      // Activate timer
                } else {                                                        // negative zero-crossing
                        // ENTER INACTIVE INTERVAL
                        T3CONbits.TON = 0;                      // Deactivate timer
                }
                        OVDEc = 0;                                              // Override output to high
                        OVDVc = 1;
        }

}
```

Listing B.8: *isr_timer1.c - interrupt handler to modulate phase A current*

```
#include "h\p30f2010.h"
#include "h\common.h"

/*-----------------------------------------------------------------------
  Function Name: _T1Interrupt
  Description:   Timer1 Interrupt Handler
  Inputs:        None
  Returns:       None
-----------------------------------------------------------------------*/
void __attribute__((__interrupt__)) _T1Interrupt( void )
{
        T1CONbits.TON = 0;                              // Deactivate Timer
        IFS0bits.T1IF = 0;                              /* reset Timer 1 interrupt flag */

        if (OVDEa == 0) {                               // ENTER EPSILON INTERVAL

                OVDEa = 1;                                              // Cancel PWM override
                TMR1 = 0;                                               // Reset timer value
                PR1 = period_epsilon;           // Set timer to epsilon period
                T1CONbits.TON = 1;                      // Activate Timer

        } else {                                                        // ENTER PHI INTERVAL

                OVDEa = 0;                                              // Override output to low
                OVDVa = 0;
        }

}
```

Listing B.9: *controls.c - code to handle control knob and button*

```
#include "h\p30f2010.h"
#include "h\LCD_Display.h"
#include "h\common.h"

#define knobdir PORTCbits.RC14  // second output of opto-interrupter

void controls_Init(void);
void _ISR _INT1Interrupt( void );       // SET button handler
void _ISR _INT2Interrupt( void );       // Control knob handler

void controls_Init(void) {

        TRISCbits.TRISC14 = 1;  // Set RC14 as digital input
        CNEN1bits.CN0IE = 0;    // Disable CN interrupt on CN0/RC14

        INTCON2bits.INT1EP = 1; // INT1 interrupts on negative edge
```

```
        IFS1bits.INT1IF = 0;     /*Reset INT1 interrupt flag */
        IEC1bits.INT1IE = 1;     /*Enable INT1 Interrupt Service Routine */

        INTCON2bits.INT2EP = 0; // INT2 interrupts on positive edge
        IFS1bits.INT2IF = 0;     /*Reset INT2 interrupt flag */
        IEC1bits.INT2IE = 1;     /*Enable INT2 Interrupt Service Routine */
}


/*-----------------------------------------------------------------------
  Function Name: INT1Interrupt
  Description:   INT1 pin ISR - handles OK button
  Inputs:        None
  Returns:       None
-----------------------------------------------------------------------*/
void _ISR _INT1Interrupt( void ) {

        ms_delay(50);                           // crude debounce delay
        IFS1bits.INT1IF = 0;            // reset interrupt flag

        status_menu = !status_menu;

        if (status_item) {
                Display_CharPos(1,13);  // epsilon position
        } else {
                Display_CharPos(1,6);   // alpha position
        }

        if (status_menu) {
                Display_Byte(0x7F);             // display adjustment arrow

                // Calculate parameter limits
                if (status_item) {
                        epsilon_limit = 180 - param_alpha;
                } else {
                        alpha_limit = 180 - param_epsilon;
                }

        } else {
                Display_Byte('_');              // clear adjustment arrow
        }
}

/*-----------------------------------------------------------------------
  Function Name: INT2Interrupt
  Description:   INT2 pin ISR - handles control knob
  Inputs:        None
  Returns:       None
-----------------------------------------------------------------------*/
void _ISR _INT2Interrupt( void ) {
        unsigned int temp_delay = 0x8FFF;

        //while ( temp_delay --);   // crude debounce delay

        IFS1bits.INT2IF = 0;            // reset interrupt flag

        lcd_update = 1;

        if (status_menu == 0) {                         // SELECTING PARAM

                if (knobdir == 1) {
                        status_knob++;
                } else if (status_knob > 0) {
                        status_knob--;
                }

                if (status_knob > 5){
                        status_item = 1;
                } else {
                        status_item = 0;
                }
```

```
                if (status_knob > 11){status_knob = 11;}

        } else if (status_menu == 1) {          // ADJUSTING PARAM

                if (status_item == 0) {                 // Adjusting alpha
                        if (knobdir == 1) {
                                param_alpha++;
                                if (param_alpha > alpha_limit) {param_alpha = alpha_limit;}
                        } else if (param_alpha > 0) {
                                param_alpha--;
                        }

                } else if (status_item == 1) {  // Adjusting epsilon
                        if (knobdir == 1) {
                                param_epsilon++;
                                if (param_epsilon > epsilon_limit) {param_epsilon = epsilon_limit;}
                        } else if (param_epsilon > 0) {
                                param_epsilon--;
                        }
                }

        }

}
```